



Balkan Journal of Electrical & Computer Engineering

An International Peer Reviewed, Referred, Indexed and Open Access Journal

www.bajece.com

Vol : 6
No : 3
Year : 2018
ISSN : 2147 - 284X



It is abstracted and indexed in, Index Google Scholarship, the PSCR, Cross ref, DOAJ, Research Bible, Indian Open Access Journals (OAJ), Institutional Repositories (IR), J-Gate (Informatics India), Ulrich's, International Society of Universal Research in Sciences, DRJI, EyeSource, Cosmos Impact Factor, Cite Factor, SIS Scientific Indexing Service, IJIF, iifactor. ULAKBİM-TR Dizin.

General Publication Director & Editor-in-Chief
Musa Yılmaz, Batman University, Turkey.

Vice Editor
Hamidreza Nazarpouya, University of California Riverside, USA

Scientific Committee
Abhishek Shukla (India)
Abraham Lomi (Indonesia)
Aleksandar Georgiev (Bulgaria)
Arunas Lipnickas (Lithuania)
Audrius Senulis (Lithuania)
Belle R. Upadhyaya (USA)
Brijender Kahanwal (India)
Chandar Kumar Chanda (India)
Daniela Dzhonova-Atanasova (Bulgaria)
Deris Stiawan (Indonesia)
Emel Onal (Turkey)
Emine Ayaz (Turkey)
Enver Hatimi (Kosovo)
Ferhat Sahin (USA)
Gursel Alici (Australia)
Hakan Temeltaş (Turkey)
Ibrahim Akduman (Turkey)
Jan Izykowski (Poland)
Javier Bilbao Landatxe (Spain)
Jelena Dikun (Lithuania)
Karol Kyslan (Slovakia)
Kunihiko Nabeshima (Japan)
Lambros Ekonomou (Greece)
Lazhar Rahmani (Algerie)
Marcel Istrate (Romania)
Marija Eidukeviciute (Lithuania)
Milena Lazarova (Bulgaria)
Muhammad Hadi (Australia)
Muhamed Turkanović (Slovenia)
Mourad Houabes (Algerie)
Murari Mohan Saha (Sweden)
Nick Papanikolaou (Greece)
Okyay Kaynak (Turkey)
Osman Nuri Ucan (Turkey)
Ozgur E. Mustecaplioglu (Turkey)
Padmanaban Sanjeevikumar (India)
Ramazan Caglar (Turkey)
Rumen Popov (Bulgaria)
Tarek Bouktir (Algeria)
Sead Berberovic (Croatia)
Seta Bogosyan (USA)
Savvas G. Vassiliadis (Greece)
Suwarno (Indonesia)
Tulay Adali (USA)
Yogeshwarsing Calleecharan (Mauritius)
YangQuan Chen (USA)
Youcef Soufi (Algeria)

Aim & Scope

The journal publishes original papers in the extensive field of Electrical-Electronics and Computer engineering. It accepts contributions which are fundamental for the development of electrical engineering, computer engineering and its applications, including overlaps to physics. Manuscripts on both theoretical and experimental work are welcome. Review articles and letters to the editors are also included.

Application areas include (but are not limited to): Electrical & Electronics Engineering, Computer Engineering, Software Engineering, Biomedical Engineering, Electrical Power Engineering, Control Engineering, Signal and Image Processing, Communications & Networking, Sensors, Actuators, Remote Sensing, Consumer Electronics, Fiber-Optics, Radar and Sonar Systems, Artificial Intelligence and its applications, Expert Systems, Medical Imaging, Biomedical Analysis and its applications, Computer Vision, Pattern Recognition, Robotics, Industrial Automation.



ISSN: 2147- 284X
Vol: 6
No : 3
Year: July 2018

CONTENTS

- T.P. Fowdur, R. Abdool Khader;** An Anti-Web Phishing Application for Analysing the Security of Websites**146-152**
- L. T. Ergene, M. Imeryuz, C. Ekin;** Cross Saturation Inductance Analysis of a Permanent Magnet Synchronous Motor,**153-158**
- K. Y. Aldoğan, C. Ide;** Experimental Investigation of Refractive Index Measurement of Common Solvents and Aqueous Solutions in the Infrared Wavelengths,**159-164**
- R. Koprü,** FSRFT Based Broadband Double Matching via Passband Extremums Determination,**165-171**
- A. Gencer;** Modelling and control of permanent magnet synchronous generator based on three level NPC using fuzzy PI,**172-177**
- T. Ercan, M. Asim;** Energy Efficient Routing Protocol to Extend WSN Lifetime,**178-182**
- A. Şenpınar;** PV Array Based Smart Home Automation System,.....**183-190**
- A. Gezer;** Identification of abnormal DNS traffic with Hurst parameter,**191-197**
- H. Gözde, B. Baydar, M.C. Taplamacioglu;** Analysis of the Effect of Uncertain Renewable Sources on Static Voltage Stability by Using NR-Based DSOPF Model with Adapted IEEE-30 Bus Test System, ...**198-206**
- H. S. Noğay, T. C. Akinci;** A Convolutional Neural Network Application for Predicting the Locating of Squamous Cell Carcinoma in the Lung,**207-210**

**BALKAN
JOURNAL OF
ELECTRICAL & COMPUTER ENGINEERING**
(An International Peer Reviewed, Indexed and Open Access Journal)

Contact
Batman University
Department of Electrical-Electronics Engineering
Bati Raman Campus Batman-Turkey

Web: <https://www.bajece.com>
<http://dergipark.gov.tr/bajece>
e-mail: bajece@hotmail.com

An Anti-Web Phishing Application for Analyzing the Security of Websites

T. P. Fowdur and R. Abdool Khader

Abstract- Nowadays, one of the major internet security problems being faced is ‘Web Phishing’, whereby attackers get hold of the personal and sensitive information of the internet users. Sometimes, attackers create fake web pages just to mislead users and give them wrong information. With the increase of more and more sophisticated attacks like Whale Phishing, Spear Phishing, and Ransomware among others, internet users easily fall in attackers’ traps. Most web browsers are not able to counteract or block these attacks and hence internet users consider the spoofed webpages to be legitimate ones and end up giving their details like credit cards details, passwords and usernames among others. In this paper, an application has been developed in Java that performs several tests on a URL, on the different hyperlinks present on the web page and on the content of the web page and provides a security rating to the internet user. Together with the percentage security, the user is informed if the web page is safe, doubtful or unsafe. The security ratings of several website domains such as, .gov, .co, .edu, .info, .mu, .ac, .org, .net, .com were also analysed. Furthermore, tests using independent samples ANOVA and Tukey HSD were performed and they revealed that there was a significant difference between the security ratings of the websites.

Index Terms— Phishing, IP, URL, Web Security

I. INTRODUCTION

WITH the increase in internet usage, there has been a significant increase of phishing attacks. Usually attackers impersonate as someone else to gather information or to provide the user with misleading information. Often, it might happen that the user receives an e-mail from a phisher where he is asked to upgrade his profile through an embedded hyperlink. However, when the user enters the hyperlink and enters his personal information, the attacker gets hold of this information and misuses them. Since these e-mails are malicious copies of legitimate ones, it is hard for the human eyes to distinguish between the legitimate and the malicious e-mail. According to [1], in 2015, at least 230,280 phishing attacks were recorded which increased to 255,065 in 2016 worldwide.

T. P. FOWDUR is with the Department of Electrical and Electronic Engineering, University of Mauritius (email: p.fowdur@uom.ac.mu)

R. ABDOOL KHADER is with the Department of Electrical and Electronic Engineering, University of Mauritius (email: bibi.abdool8@umail.uom.ac.mu)

Manuscript received April 10, 2018; accepted June 1, 2018.
DOI: [10.17694/bajece.435864](https://doi.org/10.17694/bajece.435864)

Several publications have proposed schemes to counteract web phishing. An overview is given next. In [2], to secure online transactions, an Anti-Phishing Prevention Technique [APPT] was proposed where a One-Time Password [OTP] will be generated and communicated to the user via an alternate e-mail or via SMS [3]. After that, a token containing the user’s information will be created and stored in the user machine. The password and the token together will authenticate the user. When the user logs on a webpage, his personal data are checked and the token name is retrieved. In [4], a rating of webpages was provided based on users’ experiences on a webpage. If a majority of people have rated a webpage positively, it will display ‘This site is safe’, if the majority have rated negatively, it will display ‘This site is unsafe’, else it will display ‘Unknown site’. In [5], if alterations were detected on webpages, the webmasters are alerted and if a user browses a phishing webpage or is about to download a malicious file, a warning is displayed to him. Also, a transparency report is displayed to the user. Furthermore, several web extensions can be used to prevent phishing attacks. In [6], AntiPhish was used which is suitable for non-experienced web users as it keeps track of the user’s personal information. It scans a webpage and if it finds it malicious, it prevents the submission of personal information to that webpage. However, AntiPhish is limited to webpages written in HTML. In [7], Link Guard Algorithm is proposed which can detect and stop 195 out of 203 attacks. This algorithm analyses the differences between the visual link and the actual link and calculates the similarity of the URI of the hyperlink with that of the legitimate website. If they are not the same, then it is considered to be an attack. In [8], ratings and reviews are collected from experienced users and the ratings of the webpages are displayed as traffic lights next to the search engine. In [9], GeoTrust developed TrustWatch where information is displayed to users so that the identity of websites for e-commerce services can be verified. TrustWatch can also block pop-up windows and report suspicious webpages. In [10], the web extension GoldPhish is proposed where the logo of suspicious webpages is extracted and are converted to text. The text is queried as a google search and the result obtained is compared with the suspicious webpage. If the results do not match, then it is considered as a possible attack. In [11], an approach based on K-Means and Naïve-Bayes was proposed to check the behaviour of browsed webpages. With this method, approximately 18,480 unique phishing webpages have been detected. Firstly, a K-Means Classifier is used and then a Naïve-Bayes Classifier is used and based on the results, the webpage is rated as phishing, non-phishing or suspicious. In [12], it has been proposed that through the source code, phishing webpages can be detected. For example, if the logo loads from an external

link, it is a phishing characteristic. Another characteristic would be if the URL contains characters such as '@' and '_'. Phishing webpages are normally short-lived and the content has language anomalies. The presence of pop-up windows asking to update and validate accounts usually means that the webpage has been compromised.

In this paper, an application was developed in Java to give a percentage security rating to a webpage based on different features such as the Uniform Resource Locator (URL), the Hyper Text Markup Language (HTML) source code and the content of the webpage. However, compared to the previous proposed solutions, this application conducts its tests on nine sets of domains which are '.com', '.net', '.org', '.ac', '.gov', '.mu', '.info', '.edu', and '.co'. The percentage security obtained are recorded and an Analysis of Variance (ANOVA) test is performed on them with the HSD Tukey test to determine whether the difference between the means of the percentage security is significant or not.

The organisation of this paper is as follows. Section 2 gives an overview of the different Phishing attacks and some existing solutions. Section 3 describes the methodology employed to conduct the research. Section 4 describes the tests performed on the application and the results obtained and Section 5 concludes the paper.

II. BACKGROUND

This section starts with an overview of the different types of web-phishing attacks that have been recorded worldwide, followed by some existing solutions.

2.1 Overview of web-phishing attacks

Different types of web-based phishing attacks have been encountered till now, for instance:

- Deceptive Phishing [13]: in this case, the user receives an e-mail with an embedded hyperlink and he will be asked to update his account or to warn him about system failures. When the user browses the provided hyperlink, he will be asked to enter his personal information and login credentials. However, the success of this type of attacks depend on how closely the phishing webpage is similar to the legitimate one.
- Speare Phishing [14]: this is the most common type of phishing where the goal is to lure users to click on malicious hyperlinks so that the attackers get hold of personal information.
- Pharming [15]: in this case, the Domain Name System (DNS) server is the target and the Internet Protocol (IP) addresses are altered. When a user browses a webpage, he will be redirected to the webpage desired by the attacker.
- Clone Phishing [16]: legitimate e-mails are cloned and the attachments and hyperlinks are altered to redirect the users to malicious webpages where their credentials are captured by the attacker.

2.2 Security features in Web Browsers

- Connection Security: for some webpages, a lock icon is displayed in the location bar to inform the user that the connection to that particular webpage is safe. For example, this icon appears when a user browses to 'https://www.ebay.com'.

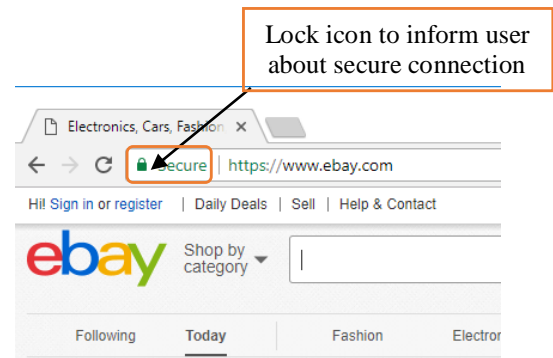


Figure 1: Lock icon for secure connection

- Protection against trackers [18]: information about user's browsed webpages can be collected by trackers. Furthermore, trackers also keep track of the device that the user is using to access the webpages. To seek protection from these trackers, Mozilla Firefox has developed a security feature to block them.

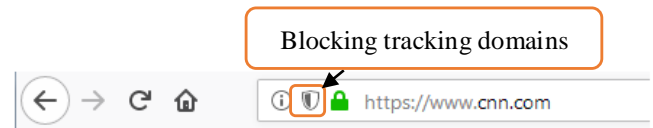


Figure 2: Protecting Mozilla Firefox from trackers

III. PROPOSED ANTI-PHISHING APPLICATION

3.1 Software Architecture

The application interface is shown in Figure 3.

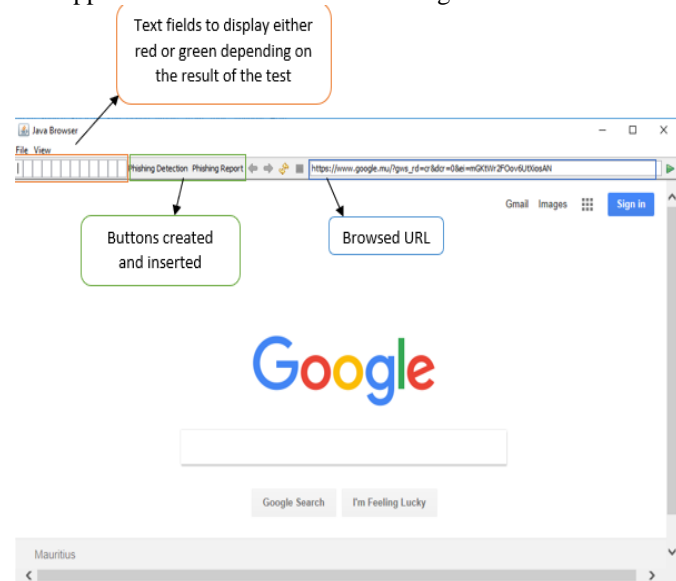


Figure 3: Application Interface

Twelve text fields are created to be set to either red or green depending on the result of the different tests conducted. Furthermore, two buttons are created namely 'Phishing Detection' and 'Phishing Report'. All these are implemented in the Java Web Browser. When 'Phishing Detection' button is clicked, tests will be carried out on the URL, HTML and content of the webpage and the text fields will be set accordingly. And when 'Phishing Report' button is clicked, a report is provided to the user based on the results of the different tests.

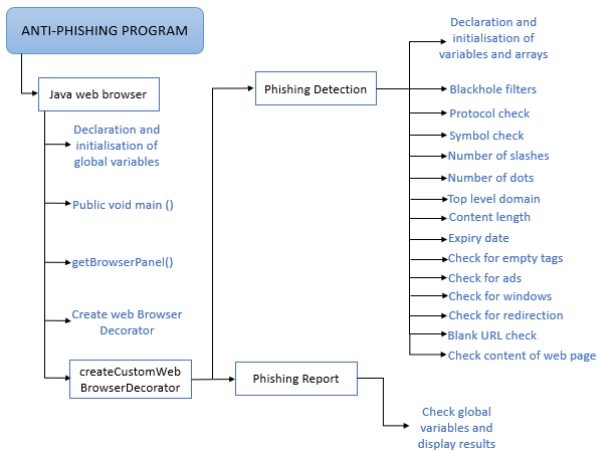


Figure 4: Software Architecture

The architecture of the anti-phishing software is shown in Figure 4. The Java web Browser declares and initialises the global variables and contains two buttons: 'Phishing Detection' and 'Phishing Report'. The pseudocode for 'Phishing Detection' is given in Section 3.2 and that of 'Phishing Report' in Section 3.3.

3.2 Pseudocode for 'Phishing Detection'

1. Declare and initialise global variables
2. txt_protocol, txt_symbol, txt_slashes, txt_dots, txt_tld, txt_content, txt_length, txt_date, txt_tag, txt_ads, txt_window, txt_redirect, txt_blankurl, txt_content: set to either red or green depending on the result of the tests
3. Create Java web browser
4. Create text fields degree1 to degree12 null, of length '1'
5. degree1 – degree12: Background set to either red or green depending on the result of the tests.
6. Declare and initialise scale to '0': scale counts the number of anomalies detected.
7. Declare and initialise arrays for malicious words and percentage spam
8. Extract browsed URL
9. Pass URL in blackhole filter and check if present
10. If yes,
11. Set text fields degree1 to degree12 to red and display 'Phishing Webpage'
12. Else,
13. Extract protocol
14. If protocol = https,

15. Set degree1 to green and set txt_protocol to green
16. Else,
17. Set degree1 to red and add 1.0 to scale
18. Check for '@' and '_'
19. If present,
20. Set degree2 to red and add 1.0 to scale
21. Else,
22. Set degree2 to green and set txt_symbol to green
23. If no. of slashes > 5
24. Set degree3 to red and add 1.0 to scale
25. Else,
26. Set degree3 to green and set txt_slashes to green
27. If no. of dots > 5
28. Set degree4 to red and add 1.0 to scale
29. Else,
30. Set degree4 to green and set txt_dots to green
31. Extract Top-Level Domain
32. If (tld > 4) && (tld < 2),
33. Set degree5 to red and add 1.0 to scale
34. Else,
35. Set degree5 to green and set txt_tld to green
36. If content length of browsed URL = -1
37. Set degree6 to red and add 1.0 to scale
38. Else,
39. Set degree6 to green and set txt_content to green
40. If (expiry date < last modified date),
41. Set degree7 to red and add 1.0 to scale
42. Else,
43. Set degree7 to green and set txt_date to green
44. If empty tags present in source code
45. Set degree8 to red and add 1.0 to scale
46. Else,
47. Set degree8 to green and set txt_tag to green
48. If ads present in source code
49. Set degree9 to red and add 1.0 to scale
50. Else,
51. Set degree9 to green and set txt_ads to green
52. If pop-up present in source code
53. Set degree10 to red and add 1.0 to scale
54. Else,
55. Set degree10 to green and set txt_popup to green
56. If URL is redirected,
57. Set degree11 to red and add 1.0 to scale
58. Else,
59. Set degree11 to green and set txt_redirect to green
60. If webpage contains blank URL,
61. Set degree12 to red and add 1.0 to scale
62. Else,
63. Set degree12 to green and set txt_blankurl to green
64. Read content of webpage
65. Compare each word of webpage against elements in array of malicious words
66. Declare percent of type double and initialise to '0.0': percent counts the percentage of all malicious words[19] that have been detected.
67. If present,
68. Add respective percentage spam to percent
69. If (percent > 50),
70. Add 3.0 to scale
71. Result = 100 - ((scale/15)*100)

72. Display result
73. If (result > 70),
74. Display 'High Safety Level' and set txt_content to green
75. If (result < 70) && (result > 50),
76. Display 'Average Safety Level' and set txt_content to red
77. Else,
78. Display 'Not Safe'

As it can be observed in the above pseudocode, different checks are performed and based on these results, the text fields are set to either red or green and a value of 1.0 or 0.0 is added to scale. Then the percentage security is calculated and if it is greater than 70, the webpage is considered as having a high safety level. If the percentage safety is between 50 and 70, then it is considered to be having an average safety level, else it is considered as being not safe.

3.3 Pseudocode for 'Phishing Report'

1. Create button 'Phishing Report'
2. Declare and initialise local variables
3. Pro: secure or not depending on content of txt_protocol
4. Sym: contains symbols or not depending on the content of txt_symbol
5. Slash: more than 5 slashes or not depending on the content of txt_slash
6. Dot: more than 5 dots or not depending on the content of txt_dot
7. Tld: valid or not depending on the content of txt_tld
8. Len: -1 or not depending on the content of txt_length
9. Date: last modified date greater than expiry date or not depending on the content of 'txt_date'
10. Tag: contains tag or not depending on the content of 'txt_tag'
11. Ads: contains ads or not depending on the content of txt_ads
12. Win: opens another window or not depending on the content of txt_window
13. Redirect: redirects webpage or not depending on the content of txt_redirect
14. Burl: contains blank url or not depending on the content of txt_blankurl
15. Con: set to 'safe', 'doubtful' or 'unsafe' depending on the content of txt_content
16. If (txt_protocol = green)
17. Set pro to 'secure'
18. Else,
19. Set pro to 'not secure'
20. If (txt_symbol = green)
21. Set sym to 'not contain '@' and '_'
22. Else,
23. Set sym to 'contain '@' and '_'
24. If (txt_slashes = green)
25. Set slash to 'not contain more than 5 slashes'
26. Else,
27. Set slash to 'contain more than 5 slashes'
28. If (txt_dots = green)
29. Set dot to 'not contain more than 5 dots'
30. Else,
31. Set dot to 'contain more than 5 dots'
32. If (txt_tld = green)
33. Set tld to 'valid tld'
34. Else,
35. Set tld to 'invalid tld'
36. If (txt_length = green)
37. Set len to 'not -1'
38. Else,
39. Set len to '-1'
40. If (txt_date = green)
41. Set date to 'expiry date not less than last modified date'
42. Else,
43. Set date to expiry date less than last modified date
44. If (txt_tag = green)
45. Set tag to 'not contain empty tags'
46. Else,
47. Set tag to 'contain empty tags'
48. If (txt_ads = green)
49. Set ads to 'not contain ads'
50. Else,
51. Set ads to 'contain ads'
52. If (txt_window = green)
53. Set win to 'not open another window'
54. Else,
55. Set win to 'open another window'
56. If (txt_symbol = green)
57. Set sym to 'not contain '@' and '_'
58. Else,
59. Set sym to 'contain '@' and '_'
60. If (txt_blankurl = green)
61. Set burl to 'not contain blank URLs'
62. Else,
63. Set burl to 'contain blank url'
64. If (txt_content = green)
65. Set con to 'safe content'
66. Else If (txt_content = green),
67. Set con to 'doubtful content'
68. Else,
69. Set con to 'content not safe'
70. Concatenate all the strings
71. Display result

It can be observed from this pseudocode that the global variables are set to green or red. Depending on these global variable, the local variables are set. At last, all the local variables are concatenated and displayed to the user.

ANOVA [20] is a statistical method that is used to test the differences between the means of two or more groups of data. This test is done on a general basis among the means. One-way ANOVA [21] is when only one qualitative variable is taken into consideration. Each set must contain same number of elements and must be normally distributed with the same variance.

In this work, for nine domains, the security percentage of 50 websites have been recorded. The mean security level of each of these domains was then computed and an independent

samples one-way ANOVA was used to determine if the difference between the means was significant.

IV. RESULTS

As mentioned earlier, nine different domains of websites were tested, each containing fifty (50) links.

4.1 Testing with '.com'

The tested URL is 'https://www.bestbuy.com'

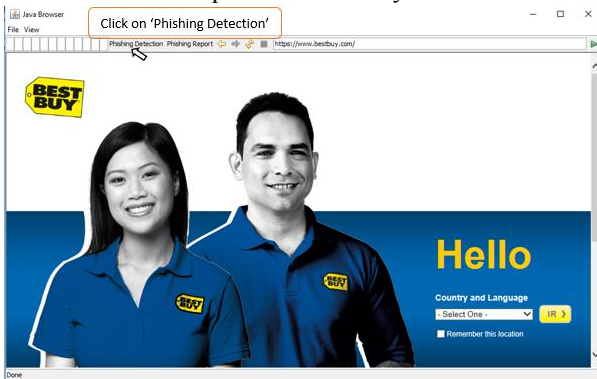


Figure 5: Navigating to the desired webpage

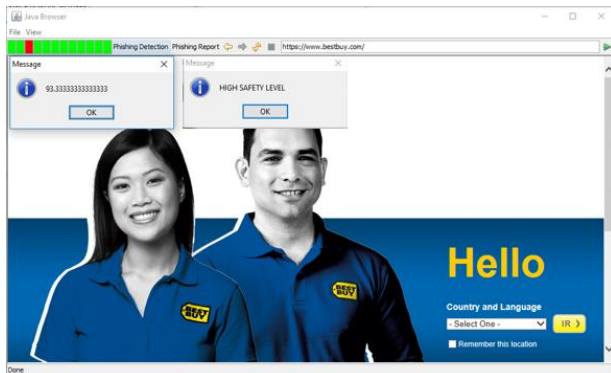


Figure 6: Result of test

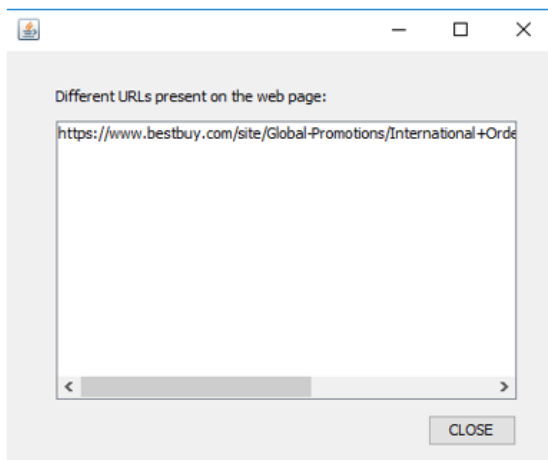


Figure 7: Hyperlinks present on webpage

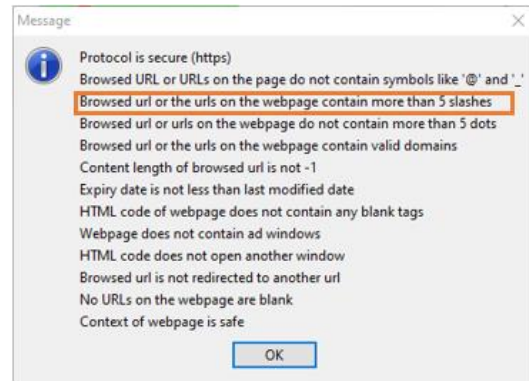


Figure 8: Phishing Report

Figure 5 shows the navigated webpage. When 'Phishing Detection' is clicked, a percentage security of 93.33 is shown along with 'High Safety Level' as shown in Figure 6. Figure 7 shows the different hyperlinks present on the webpage and Figure 8 is displayed when the user clicks on 'Phishing Report'. The selected result in Figure 8 shows the anomaly that has been detected by the application.

4.2 Testing with '.org'

The tested URL is 'www.readingrockets.org'



Figure 9: Navigating to the desired webpage

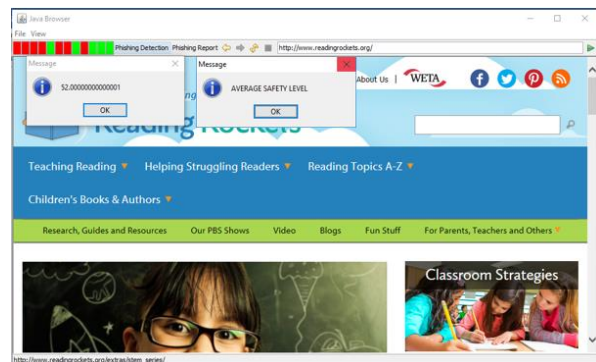


Figure 10: Result of test

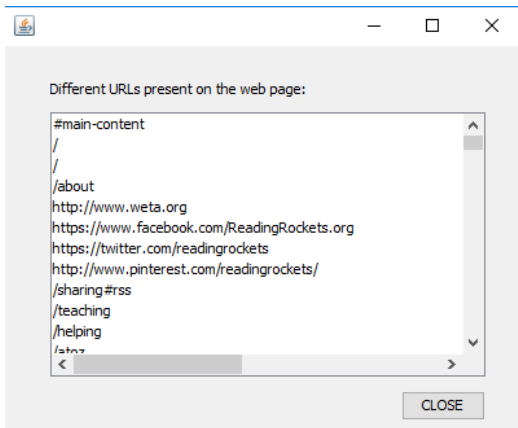


Figure 11: Hyperlinks present on webpage

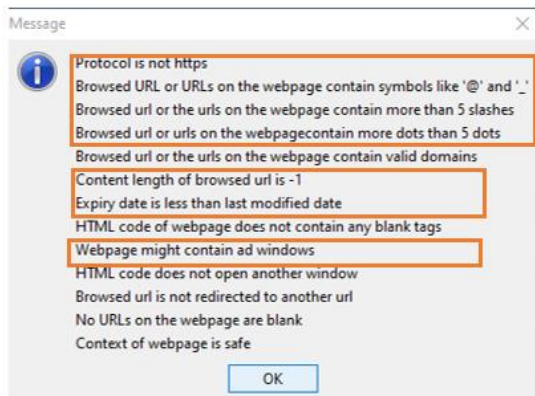


Figure 12: Phishing Report

The navigated webpage is shown in Figure 9 and after clicking on ‘Phishing Detection’, the results are displayed as shown in Figure 10. Figure 11 shows the different hyperlinks present on the webpage and Figure 12 shows the different anomalies that have been detected by the application.

The mean security percentages for each domain is shown in Figure 13.

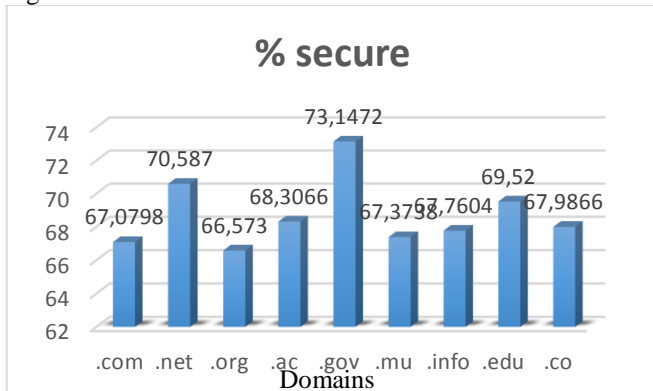


Figure 13: Bar Chart for average percentage security

An ANOVA Independent test and an HSD Tukey test were performed on the nine sets of results that were obtained. The value obtained for F_{obs} and F_{table} were 2.7618 and 1.9594 respectively. Hence, it can be concluded that the difference

between the means is significant. Furthermore, the HSD Tukey test revealed that the pairwise differences between the means of ‘.com and .gov’ and ‘.gov and .mu’ are significant.

V. CONCLUSIONS AND FUTURE WORK

Web phishing is a rising security risk which target many people and provide them with misleading information. In this paper, an application has been designed which gives a rating when the button ‘Phishing Detection’ is clicked. The rating is based on tests on different characteristics of the URL, the HTML code and the content of the webpage. Compared to [12], the application can check for anomalies in the content of the webpages and based on the results, a rating is displayed to the user.

The program also rates a webpage based on the different tests carried out. In contrast with [4] where the rating is based on the users’ experiences. Moreover, the ANOVA test performed confirmed that the difference between the security of different domains is significant. Finally, it will be interesting to investigate the possibility of integrating the schemes developed in [22] and [23] into the proposed application.

ACKNOWLEDGMENT

My gratitude to all those who have helped and supported me throughout this research work.

REFERENCES

- [1] Aaron G. and Rasmussen R., Global Phishing Survey: Trends and Domain Name Use in 2016, pp. 5, 2017.
- [2] Chelliah G. A and Aruna S., Preventing Phishing Attacks Using Anti-Phishing Prevention Technique, International Journal of Engineering Development and Research, pp. 60- 63, 2014.
- [3] Khan A. A., Preventing Phishing Attacks using One Time Password and User Machine Identification, International Journal of Computer Application, vol. 68, no. 3, pp. 7-11, 2013.
- [4] Avast Support. 2018. Avast Online Security browser extension – Getting Started | Official Avast Support. [Online] Available at: <https://support.avast.com/en-au/article/18/> [Accessed 23 November 2017]
- [5] Safe Browsing – Google Safe Browsing. 2018. [Online] Available at: <https://safebrowsing.google.com/> [Accessed 9 January 2018]
- [6] Kirda E. and Krugel C., Protecting Users Against Phishing Attacks, The Computer Journal, vol. 00, no. 0, pp. 1-8, 2005.
- [7] Naresh U., Sagar U. V. and Reddy C. V. M, Intelligent Phishing Website Detection and Prevention System by Using Link Guard Algorithm, IOSR Journal of Computer Engineering (IOSR-JCE), vol. 14, no. 3, pp. 28-36, 2013.
- [8] WOT Services Ltd.,2018. Web of Trust (WOT) – Crowdsourced web safety | WOT (Web of Trust). [Online] Available at: <https://www.mywot.com/en/aboutus> [Accessed 10 September 2017]
- [9] TrustWatch – WEB SITE VERIFICATION SERVICE. [Online] Available at: https://www.trustico.co.in/material/DS_TrustWatch.pdf [Accessed 29 October 2017]
- [10] Jain A. K. and Gupta B. B., Phishing Detection: Analysis of Visual Similarity Based Approaches, Security and Communication Networks, vol. 2017, pp. 1-20, 2017
- [11] Wanawe K., Awasure S. and Puri N. V., An Efficient Approach to Detecting Phishing A Web Using K-Means and Naive- Bayes Algorithms, International Journal of Research in Advent Technology, vol. 2, no. 3, pp. 106-111, 2014
- [12] Alkhozai M. G. and Batarfi O. A., Phishing Websites Detection based on Phishing Characteristics in the Webpage Source Code, International Journal of Information and Communication Technology Research, vol. 1, no. 6, pp. 283-291, 2011

- [13] The State of Security. 6 Common Phishing Attacks and How to Protect Against Them, 2018. [Online] Available at: <https://www.tripwire.com/state-of-security/security-awareness/6-common-phishing-attacks-and-how-to-protect-against-them/> [Accessed 8 April 2018]
- [14] Ho G., Sharma A., Javed M., Paxson V. and Wagner D., Detecting Credential Spearphishing Attacks in Enterprise Settings, usenix, pp. 469-484, 2017.
- [15] The State of Security. 6 Common Phishing Attacks and How to Protect Against Them, 2018. [Online] Available at: <https://www.tripwire.com/state-of-security/security-awareness/6-common-phishing-attacks-and-how-to-protect-against-them/> [Accessed 8 April 2018]
- [16] Chaudhry J. A., Chaudry S. A. and Rittenhouse R. G., Phishing Attacks and Defences. International Journal of Security and its Application, vol. 10, no. 1, pp. 247-256, 2016.
- [17] Tracking Protection | Firefox Help. 2018. Tracking Protection | Firefox Help. [Online] Available at: <https://support.mozilla.org/en-US/kb/tracking-protection> [Accessed 3 January 2018]
- [18] Lane D. M., Analysis of Variance. Online Statistics Education B. pp. 517-598
- [19] Sun T, Spam Filtering based on Naïve Bayes Classification, pp. 1-42, 2009
- [20] Heron E., Analysis of Variance – ANOVA, 2009. [Online] Available at: https://www.tcd.ie/medicine/neuropsychiatric-genetics/assets/pdf/2009_3_ANOVA.pdf [Accessed 9 December 2017]
- [21] Analysis of Variance (ANOVA) [Online] Available at: <https://www.calvin.edu/~scofield/courses/m143/materials/handouts/anova1And2.pdf> [Accessed 15 December 2017]
- [22] Rami M. Mohammad, Fadi Thabtah and Lee McCluskey, "Intelligent rule-based phishing websites classification", IET Information Security Volume: 8, Issue: 3, pp. 153 – 160, May 2014, DOI: 10.1049/iet-ifs.2013.0202.
- [23] Yasin Sönmez, Türker Tuncer and Hüseyin Gököl, "Phishing web sites features classification based on extreme learning machine", 6th IEEE International Symposium on Digital Forensic and Security (ISDFS), 22-25 March 2018, Antalya, Turkey, DOI: 10.1109/ISDFS.2018.8355342.

BIOGRAPHIES



Dr. T.P. Fowdur received his BEng (Hons) degree in Electronic and Communication Engineering with first class honours from the University of Mauritius in 2004. He was also the recipient of a Gold medal for having produced the best degree project at the Faculty of Engineering in 2004. In 2005 he obtained a full-time PhD scholarship from the Tertiary Education Commission of Mauritius and was awarded his PhD degree in Electrical and Electronic Engineering in 2010 by the University of Mauritius. He is presently an Associate Professor at the Department of Electrical and Electronic Engineering at the University of Mauritius. His research interests include Communications Theory, Multimedia Communications, Mobile and Wireless Communications, Networking, Security and Internet of Things.



Miss R. Abdool Khader is currently a final year student for BSc (Hons) Information and Communication Technologies at the University of Mauritius. Her research interest include Networking, Security and system development.

Cross Saturation Inductance Analysis of a Permanent Magnet Synchronous Motor

L.T. Ergene, Member IEEE, M. Imeryüz and C. Ekin

Abstract— This paper presents the cross saturation effect on a specially designed spoke type permanent magnet synchronous motor (PMSM) for the sensorless vector control. The cross saturation effect becomes very important where the sensorless control algorithm is used. Accurate flux linkage modeling is required to obtain a satisfactory position estimation and eventually minimum induced torque error. The magnetic saturation is the most impacting parameters affecting the position error. Since the L_d and L_q inductance difference is generally less than 5% in the spoke type PMSM, the accurate estimation of the cross saturation is critical for the sensorless vector control. In this paper, the designed PMSM has the L_d and L_q difference in 15% level even for the overload capacity. So it is even possible to operate the motor in the transient modes with the overload capacity by estimating right cross saturation effect with certain time limits. The mapping of the inductances and efficiency are obtained by using Finite element method and presented in the paper. Some experimental results are also given such as efficiency and power-speed variation at the constant torque.

Index Terms—Permanent magnet synchronous motor, finite element method, cross saturation effect, d-q inductances, sensorless vector control.

I. INTRODUCTION

THE rapid developments in magnetic materials used in the production of electric motors has led to the development of special electric motors such as brushless DC, permanent magnet synchronous motors with the electronic commutation. Reaching high speeds in the electronic components used in motor drive systems and the cost reduction in the manufacturing are also supporting this development. It is very critical to find the most suitable motor and drive system in terms of the design and control algorithm for the application. Permanent magnet synchronous motors (PMSM) can be used widely in the systems from low to medium power because of their high efficiency, high torque/inertia ratio, high reliability and high dynamic performance features. The efficient motor design was the main focus on the early literature [1]. However the control algorithms become more important in the recent publication. Generally, ac variable-speed drive of a permanent magnet synchronous motor needs a position sensor for the commutation and also current control.

L. T. ERGENE, is with Department of Electrical Engineering of Istanbul Technical University, Istanbul, Turkey, (e-mail: ergenel@itu.edu.tr).

M. IMERYÜZ, is with Department of Electrical Engineering of Istanbul Technical University, Istanbul, Turkey, (e-mail: imeryuz@itu.edu.tr).

C. EKIN, is with PROMOTE AS, Çorlu, Tekirdag, Turkey, (e-mail: cihad.ekin@promote.com.tr)

Manuscript received May 23, 2018; accepted June 10, 2018.

DOI: [10.17694/bajece.426284](https://doi.org/10.17694/bajece.426284)

Position sensor brings some disadvantages such as increased drive cost, reduced mechanical robustness of the overall system, etc. [2]. Sensorless control solutions have been studied since the beginning of 80s to cope with these drawbacks [3-6]. There are two methodologies in the literature: one is based on the back-EMF and the other is based on the position dependency of the winding. In low speed applications extra high frequency signal should be injected to estimate the rotor flux position. The significant saliency between L_d and L_q becomes critical. Interior PM synchronous motors are naturally suitable for the sensorless control because of their saliency. Rahideh et.al. succeeded the high performance direct torque control of PMSM by using fuzzy logic and genetic algorithms in 2007 [7]. Novak et al. used the field oriented control with the flux weakening in 2008 [8]. PMSM with sensorless control requires to take into account the cross saturation carefully. The cross saturation was studied by different researchers. Fuchs et al. pointed the constraints of the model d, q in the case of turbo alternators in 1973 [9]. The similar study was performed on the salient pole synchronous motor and the limitation of classical linear uncoupled model compared to experimental results was shown [10]. Especially the experimental validation of the saturation and cross coupling are studied in some literature [11-14]. This paper presents the analysis of a spoke type PMSM motor with its cross saturation inductances and performance calculations. It is also shown that the motor can be operated with the accurate positioning at under and overload conditions by using the sensorless control without any problem.

II. CROSS SATURATION OF PMSM

PMSM motor control systems generally have two-axis model, direct-axis (d-axis) and quadrature-axis (q-axis). Moreover these two-axis inductances, L_d and L_q directly affects the performance of the motor, such as output torque. Therefore, the analysis of these inductances is very critical for the dynamic characteristics of the motor. These d- and q-axes inductances are not constant. They are changing under different operating conditions non-linearly because of the varying current phase and magnitude and changing reluctance due to the saturation of the magnetic material [14]. This issue becomes more important especially for the dynamics model of the highly saturated PMSMs [12]-[14]. The cross saturation is taken into account in the flux models where the models are linear or non-linear. The nonlinear flux linkage equations for a saturated interior type PMSM are given as

follows

$$\lambda_d(i_d, i_q) = \lambda_{d,PM} + L_d(i_d, i_q)i_d + L_{dq}(i_d, i_q)i_q \quad [15]:$$

$$\lambda_q(i_d, i_q) = \lambda_{q,PM} + L_q(i_d, i_q)i_q + L_{qd}(i_d, i_q)i_d \quad (1)$$

where λ_d and λ_q are the total flux linkages in d and q axes respectively. $\lambda_{d,PM}$ and $\lambda_{q,PM}$ are the permanent magnet flux linkages in d and q axes. The electromagnetic torque equations in synchronous machines is defined as in Eq(2)

$$T = \frac{3}{2}p(\lambda_d i_q - \lambda_q i_d) \quad (2)$$

After substituting the non-linear flux linkage equations into Eq(1), the torque equation becomes:

$$T = \frac{3}{2}p(\lambda_{d,PM} i_q - \lambda_{q,PM} i_d + (L_d - L_q)i_d i_q + L_{dq} i_q^2 - L_{qd} i_d^2) \quad (3)$$

There are five terms in Eq.3. First and second terms represent the permanent magnet components. Third term is the reluctance torque term. Fourth and fifth terms are the cross saturation terms. The stator voltages of the PMSM can be given in dq-reference frame as follows:

$$V_d = Ri_d + \frac{d\lambda_d}{dt} - \omega\lambda_q \quad (4)$$

$$V_q = Ri_q + \frac{d\lambda_q}{dt} + \omega\lambda_d$$

Steady state voltage equations at ω speed, E back electromotive force (EMF) with the assumption of negligibly small $\lambda_{q,PM}$ are given in Eq(5)

$$\begin{aligned} V_d &= Ri_d - \omega L_q i_q - \omega L_{qd} i_d \\ V_q &= Ri_q + \omega L_d i_d + \omega L_{dq} i_q + E \end{aligned} \quad (5)$$

The cross saturation terms can be approximated by using numerical equations as follows

$$L_{dq}(i_d, i_q) = \frac{\Delta\lambda_d}{\Delta i_q} \Big|_{i_d=constant}$$

$$L_{qd}(i_d, i_q) = \frac{\Delta\lambda_q}{\Delta i_d} \Big|_{i_q=constant} \quad (6)$$

III. MODELLING OF PMSM

A. Specifications of the PMSM

The test PMSM motor is a special designed and optimized motor which has an efficiency class IE5. The motor has 1.1 kilowatts, 10 Poles, 12 stators slots, ferrite permanent magnets, 3.5 Nm, 3000 min⁻¹ rated values (500-4000 min⁻¹ without flux weakening and 6000 min⁻¹ with the flux weakening). The needle winding is used for the stator. The motor layout is given in Fig.1. in two and three dimensions.

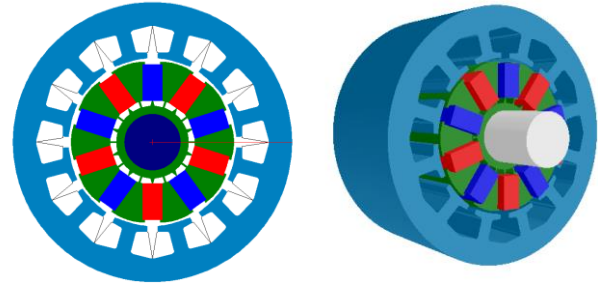


Fig.1. 1.1 kW PMSM motor view.

B. Numerical Modeling of PMSM

A commercial software (EMAG FEM) which based on Finite Element Method is used for the numerical simulations. The motor half geometry with the equi flux lines are given in Fig.2.

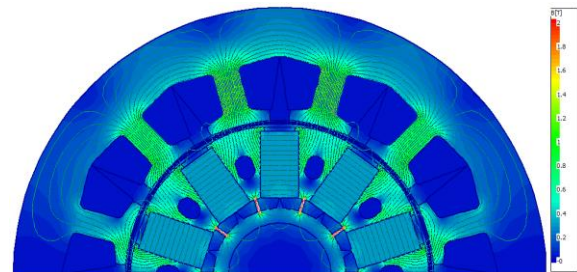


Fig.2. PMSM FEM Model (half of the motor).

The motor is simulated at very low speed to see the reluctance effect as known as the cogging torque. The cogging torque is shown for the half of the motor in Fig.3.

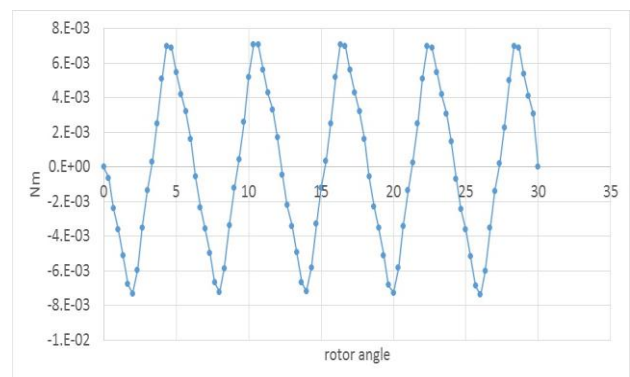


Fig.3. Cogging torque of the PMSM

The peak to peak value of the cogging torque is 14 mNm. Saliency of the motor is about 1.2 for this sensorless vector control algorithm. The motor has the cogging torque less than 1% of the rated torque. The simulated output torque profile is given in Fig. 4. Torque ripple is less than 10% of the rated torque.

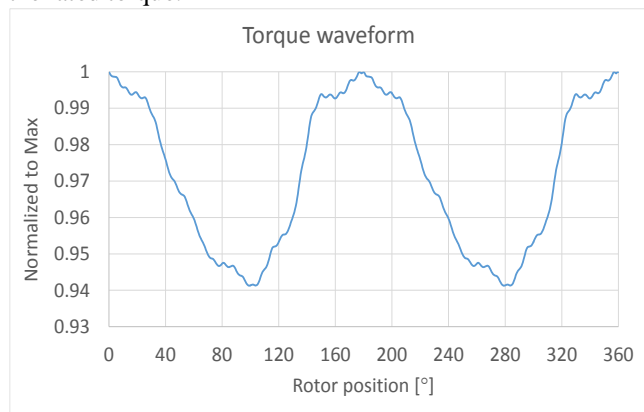


Fig.4. Output torque of the PMSM

The first model would be the no-load operation to calculation of d-axis flux linkage. Later different loading conditions will be applied to obtain d and q axes flux linkages. The flux density distributions for the different loadings are given in Fig. 5.

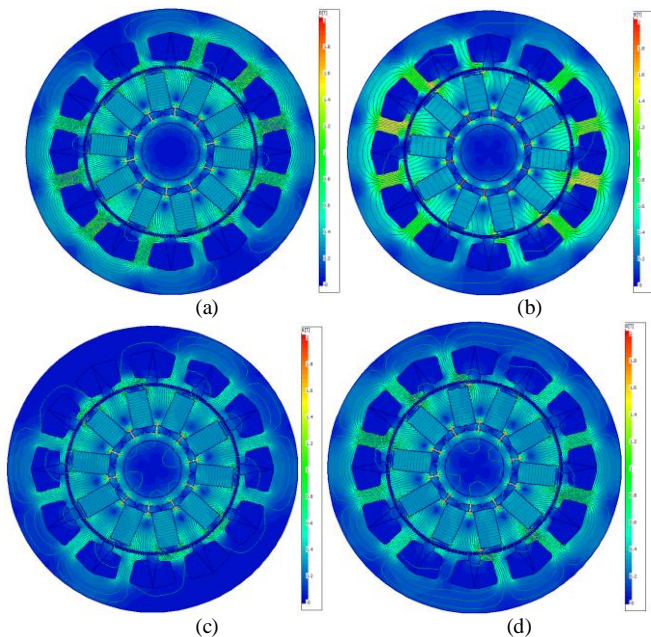
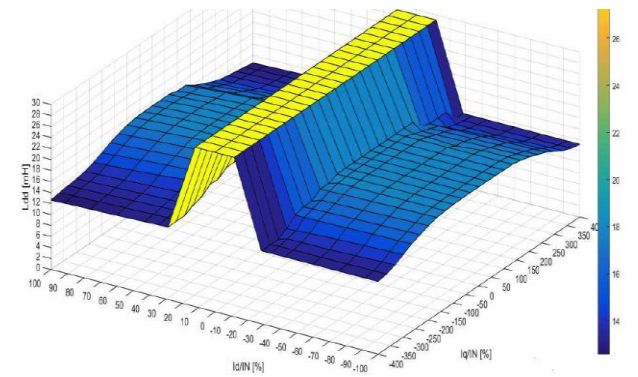


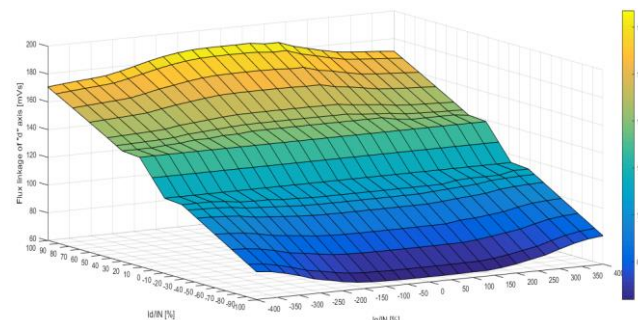
Fig.5. The flux density distribution (a) No-load at 3000 min⁻¹ (b) q-axis align, I_q = 2.5A, I_d = 0A, 3000 min⁻¹ (c) d-axis align, I_q = 0A, I_d = 2.5A, 3000 min⁻¹ (d) d-axis align, I_q = 1.8A, I_d = 1.8A, 6000 min⁻¹

Fig.6a gives the d-axis inductance (L_d) variation due to the I_d/I_N and I_q/I_N while Fig.6b shows the d-axis flux linkage variation respect to the I_d/I_N and I_q/I_N for peak $I_N = 3.5$ A. The differential inductance method is used to define the inductance values especially in the saturation region. Fig.7a and 7b present the similar variations for the q-axis inductance and flux linkage respectively for peak $I_N = 3.5$ A. Fig.8a shows L_{dq} cross saturation inductance which is calculated by using Equation 5. L_{dq} is calculated by taking the differential d axis

flux change (λ_d) respect to q axis current (I_q) while keeping the d-axis current (I_d) constant.

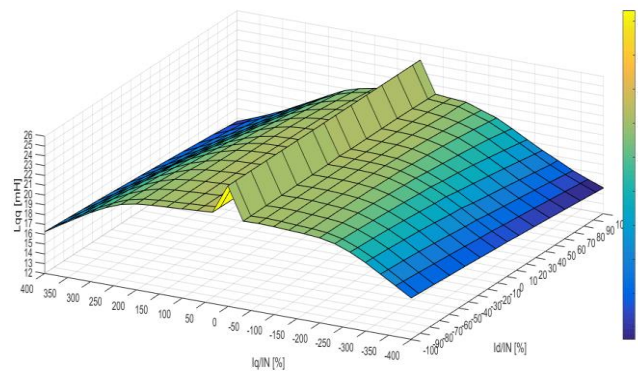


(a)

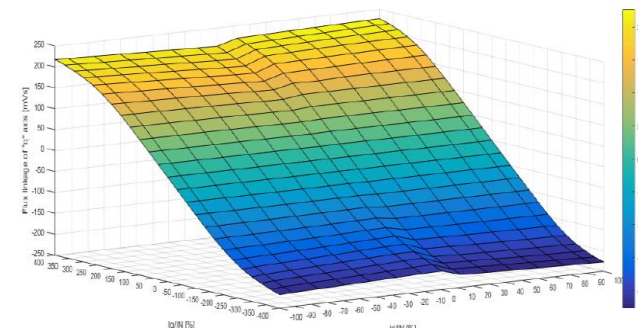


(b)

Fig.6.(a) L_d "d" axis inductance vs I_d and I_q currents (b) Flux linkage of "d" axis vs I_d and I_q currents



(a)



(b)

Fig.7.(a) L_q "q" axis inductance vs I_d and I_q currents (b) Flux linkage of "q" axis vs I_d and I_q currents

Similarly, L_{qd} cross saturation inductance is also calculated by using Eq.6 and drawn as given in Fig.8b. L_{qd} is calculated by taking the differential q axis flux change (λ_q) respect to d axis current (I_d) while keeping the q-axis current (I_q) constant.

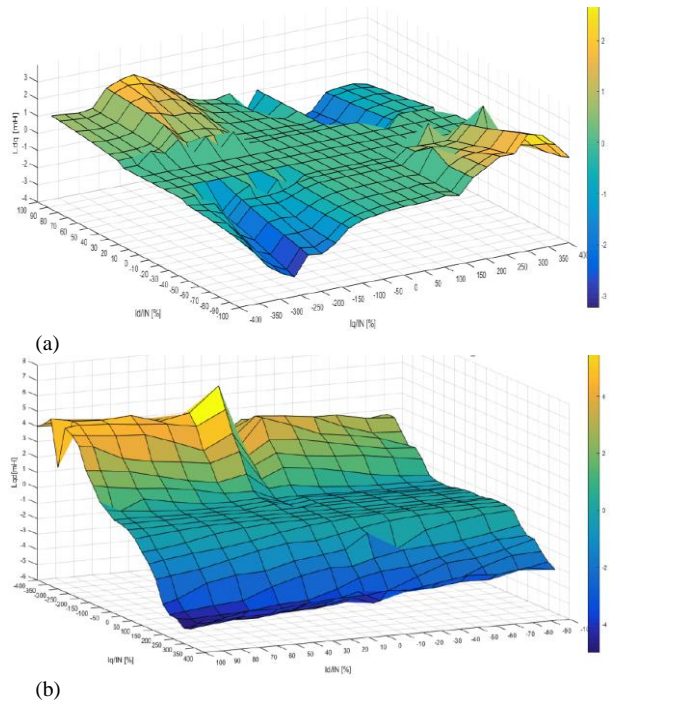


Fig.8.(a) L_{qd} cross saturation inductance (b) L_{qd} cross saturation inductance

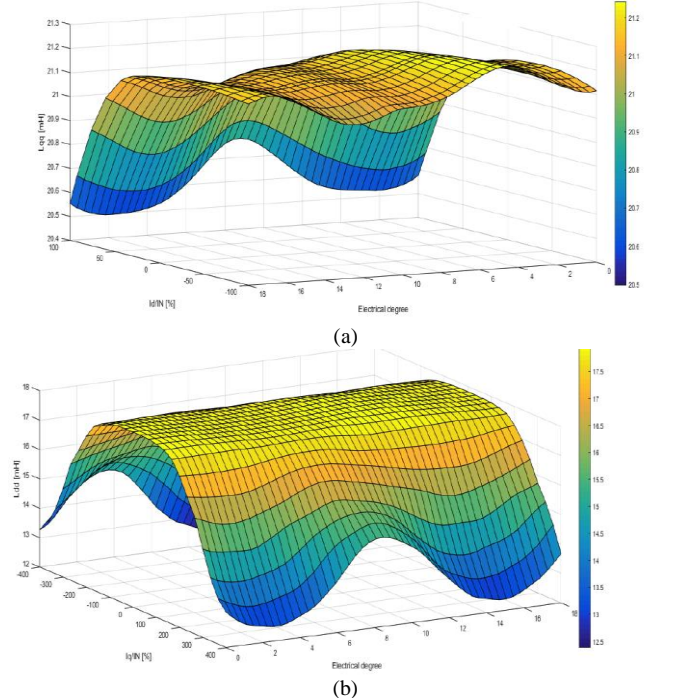


Fig.9.(a) L_q “q” axis inductance vs I_d current and rotor position ($I_q=I_N$, peak=3.5 A) (b) L_d “d” axis inductance vs I_q current and rotor position ($I_d=I_N$, peak=3.5 A)

The efficiency maps of the motor for the power vs. speed and torque vs. speed are given in Fig.10 and Fig.11. Some results can be derived from these inductance and flux linkage profiles: I_d current has low effect on “q” axis inductance. I_q current has high effect on “d” axis inductance for high current. The motor

performs over 90% efficiency in the 1500-4000 min^{-1} speed range. The back EMF results of FEM and test are given in Fig. 13 to verify the modeling consistency. The relative errors is less than 1%. Total harmonic distortion is also calculated as less than 1%. For rated performance $I_d=0$ and doesn’t affect “q” axis flux. For rated performance $I_d \neq 0$ and also doesn’t affect “q” axis flux. It doesn’t have effect on “d” axis flux, up to rated I_q . For start-up with high torque, high I_q current affects the control. Saturation effect on L_{qq} is 12 % up to the rated current. Saturation effect on L_{qd} is 33 % up to four times of the rated current. Saturated saliency is about $L_d/L_q=1.17$ up to rated current. Saturated saliency is about $L_d/L_q=1.20$ up to the four times of the rated current.

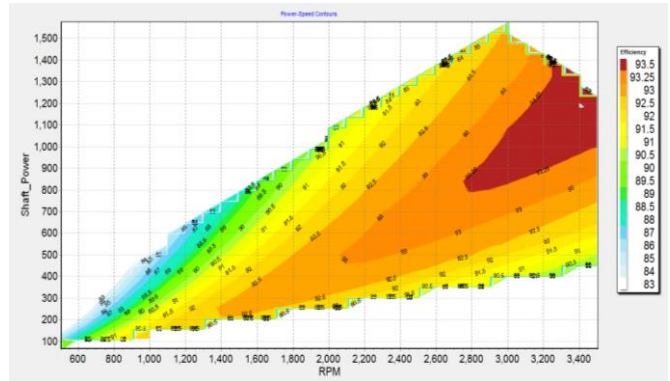


Fig. 10. Efficiency map of the PMSM (power vs. speed)

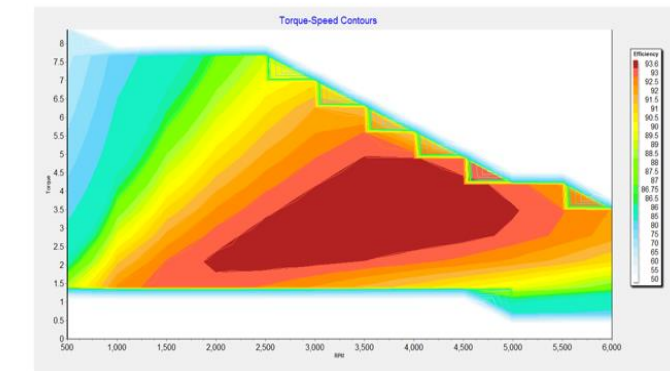


Fig. 11. Efficiency map of the PMSM (torque vs. speed)

IV. EXPERIMENTAL SETUP OF PMSM

The prototyped PMSM motor and its test setup are given in respectively Fig. 12 and Fig.13. YASKAWA brand driver are used for the vector control. The driver is a commercial type which can be used to drive any type of the motor such as inductance, synchronous reluctance, etc. MAGTROL type hysteresis brake dynamometer is used to load the motor.

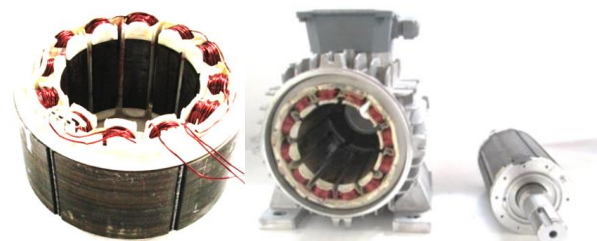


Fig.12. Manufactured PMSM



Fig.13. PMSM Experimental Setup

The Back-EMF variation of the motor for the test and simulation results is given in Fig.13.

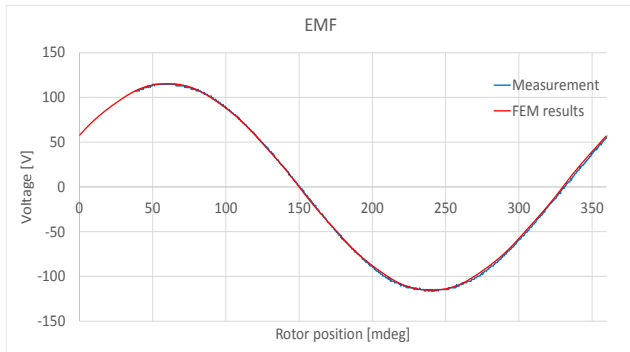


Fig.14. Back-EMF of the PMSM

The output power variation with the speed at constant torque from the test results is presented in Fig.14. The variation is linear as expected. There is no field weakening in that region. The efficiency with speed from the test results is shown in Fig.16.

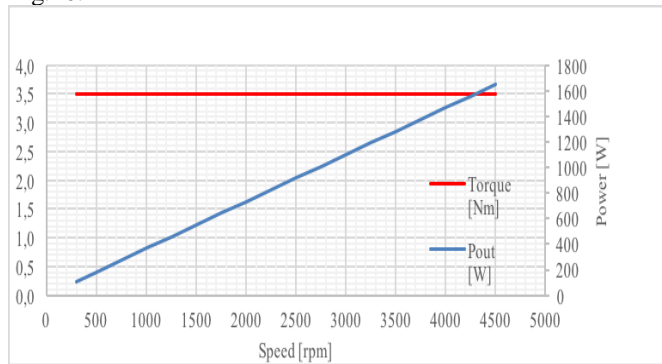


Fig.15. The output power vs. speed at the constant torque

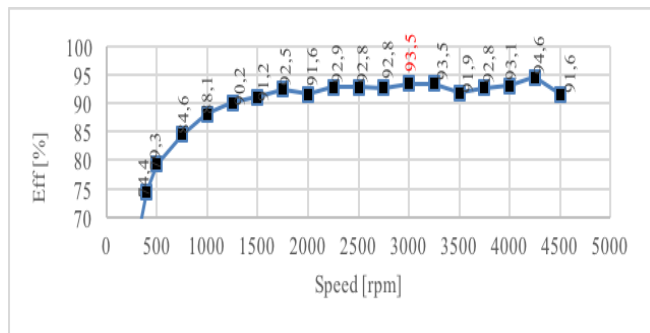


Fig.16. Efficiency vs. speed for the PMSM

Maximum current limit is chosen according to the demagnetization and winding heating. Steady state thermal analysis is used for continuous running region.

V. CONCLUSIONS

The paper presents the analysis of a special designed spoke type PMSM motor with the sensorless control for the industrial applications. Saturation of inductances is so important for the sensorless vector control, especially for low speed high torque region. The dynamic and not accurate response in positioning of the Spoke type PMSM with sensorless control because of its low saliency ratio becomes a critical drawback. The result of the motor for a full-speed range is given in Fig.17.

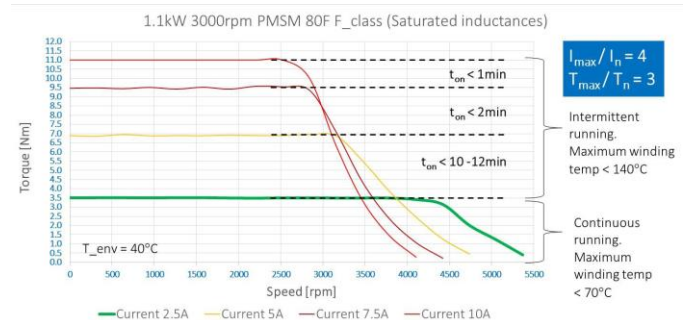


Fig.17. Torque vs. speed profile for full speed-range of the PMSM

The motor overcomes this drawback even in overloading conditions. Three times of the rated torque and four times of the rated current are achieved with control strategy including compensation of the cross-saturation effect.

REFERENCES

- [1] K. Kurihara, M.A. Rahman, "High-Efficiency Line-Start Interior Permanent-Magnet Synchronous Motors", IEEE Transactions on Industrial Applications, Vol.40, No.3, 2004, pp.789-796.
- [2] Y. Kano and N. Matsui, "Sensorless Control of Interior Permanent Magnet Synchronous Motor: An Overview and Design Study", 2017 IEEE Workshop on Electrical Machines Design, Control and Diagnosis (WEMDCD), 2017.
- [3] P. Ferraris, A. Vagati, and F. Villata, "PM brushless motor drives: A self-commutating system without rotor-position sensors," in Proc. 9th Annu. Symp. Incremental Motion Contr. Syst., Devices, June 1980, pp.305-312.
- [4] J.Davoine, R.Perrer, and H. Le-Huy, "Operation of a Self-Controlled Synchronous Motor Without a Shaft Position Sensor," IEEE Trans. Ind. Appl., vol. IA-19, pp. 217-222, Mar. 1983.
- [5] K. Iizuka, H. Uzuhashi, M. Kano, T. Endo, and K. Mohri, "Microcomputer control for sensorless brushless motor," IEEE Trans. Ind. Appl., vol. 21, no. 4, pp. 595-601, May/June 1985.
- [6] A. Athavale, H. Flieth, B.S. Gagas, T.S. Slininger, R.D. Lorenz, "Machine design for self-sensing", 2016 IEEE Symposium on Sensorless Control for Electrical Drives (SLED), 2016.
- [7] A. Rahideh, A. Rahideh, M. Karimi, A. Shakeri, M. Azadi, "High Performance Direct Torque Control of a PMSM Using Fuzzy Logic And Genetic Algorithm", IEEE International Conference on Electric Machines & Drives, Antalya, TURKEY, 2007.
- [8] J. Simanek, J. Novak, O. Cerny, R. Dolecek, "FOC and Flux Weakening for Traction Drive with Permanent Magnet Synchronous Motor", Proceedings of IEEE International Symposium on Industrial Electronics, Cambridge, UK, 2008.
- [9] E. Fuchs, E. Erdelyi "Nonlinear Theory of Turboalternators, Part II. Load Dependent Synchronous Reactances", IEEE Transactions on Power Apparatus and Systems, Vol. 92, No.2, 1973, pp.592-599.

- [10] M. Kamoun, M. Poloujadoff, "Experimental Study of The Effect of Saturation on The Steady State Operation of a Salient Pole Microalternator", *Electrical Machines and Power Systems*, Vol.10, 1985, pp.325–334.
- [11] K. Saleh, M. Sumner, "Sensorless Speed Control of Five-Phase PMSM Drives with Low Current Distortion", *Electrical Engineering*, 2017, pp.1-18.
- [12] B. Stumberger, G. Stumberger, D. Dolinar, A. Hamler, M. Trlep, "Evaluation of Saturation and Cross-Magnetization Effects in Interior Permanent-Magnet Synchronous Motor", *IEEE Transactions on Industrial Applications*, Vol.39, No.5, 2003, pp.1264–1271.
- [13] A.M. El-Serafi, A.S. Abdallah, M.K. El-Sherbiny, E. Badawy, "Experimental Study of The Saturation and the Cross-Magnetizing Phenomenon in Saturated Synchronous Machines", *IEEE Transactions on Energy Conversion*, Vol.2, No.4, 1988, pp.815–823.
- [14] E. Levi, V.A. Levi, "Impact of Dynamic Cross-Saturation on Accuracy of Saturated Synchronous Machine Models", *IEEE Transactions on Energy Conversion*, Vol.15, No.2, 2000, pp.224–230.
- [15] E. Oksuztepe, Z.Omac, H. Kurum, "Sensorless Vector Control Of PMSM With Non-Sinusoidal Flux Using Observer Based On FEM", *Electrical Engineering*, Vol.96, No.3, September 2014, pp. 227-238.

BIOGRAPHIES



Lale T. Ergene received her BS and M.Sc. degrees in Electrical Engineering at Istanbul Technical University (ITU) in 1992 and 1995 respectively and Ph.D. degree in Electrical Power Engineering at Rensselaer Polytechnic Institute (RPI), NY, USA in 2003. She worked as consultant engineer at MAGSOFT Corporation during 1999-2004. She was also an adjunct assistant professor at RPI in 2004. From 2004 to 2009, she was an assistant professor at the Informatics Institute, ITU. She joined to the faculty of Electrical Engineering, Istanbul Technical University in 2009. She is currently an associate professor at the same department. Her current research interests include design, analysis, control of electrical machines and alternative energy technologies.



Murat İmeryüz was born in Ankara in 1967. He graduated from Suadiye High School and started undergraduate education in 1984 at the Istanbul Technical University, Faculty of Electric & Electronics, Department of Electrical Engineering. He completed his undergraduate education in 1989 and M.Sc. degree in 1994 in Electrical Engineering major. He is working at the same department since 1990. His current research interests are fault diagnosis in asynchronous machines, electrical drive systems, analytical calculation of electrical machines and solar energy systems.



Cihad Ekin received his BS degree in Electrical Engineering at Istanbul Technical University (ITU) in 1997. He worked as design team leader at ARCELİK AS between 1997-2013. He is currently the Vice Director of PROMOTE AS. He has several patents on electrical motors. His research interests include design, analysis, control of PM motors.

Experimental Investigation of Refractive Index Measurement of Common Solvents and Aqueous Solutions in the Infrared Wavelengths

C. İde, K. Yüksel

Abstract—We proposed and experimentally demonstrated a fast and simple technique to measure refractive index of liquids. A commercial Optical Time-Domain Reflectometer (OTDR) was implemented for interrogating sensor tips from a remote location. The system uses Fresnel reflected light from standard single mode fiber tips as sensing points without requiring any chemical coating, delicate fiber components, and/or sophisticated architecture at the sensor head. We reported new measurements of refractive indices of common solvents and solutions at both 1550 nm and 1625 nm. The precision of the proposed measurement system was found to be in the order of 10^{-4} . The experimental results have been validated by the way of theoretical calculations.

Index Terms—Fiber optic refractometer, Fresnel reflection, OTDR, refractive index measurement.

I. INTRODUCTION

REFRACTIVE INDEX measurement is frequently used in a variety of fields, such as chemical industry, food quality and safety analysis, bio-medical applications, environmental imaging systems, petroleum and oil industry and material processing [1]. Being a very critical parameter in all of these areas, there is an increasing interest, in recent years, in determining the exact value of the refractive index of the materials. Several research groups have published different types of fiber-based refractive index sensors which include fiber Bragg gratings (FBG) structures, long period gratings (LPGs) structures, interferometers, photonic crystal fibers (PCF) and sensors using Surface Plasmon Resonance (SPR) effects [2, 3].

Among these various sensor approaches, Fresnel reflection-based refractometers have emerged as promising tool for refractive index monitoring due to their simplicity and easy accessibility. In Fresnel-reflection-based refractometers, interrogation can be done in various ways. Table I summarizes the interrogation methods, sensitivities and precisions of different Fresnel-reflection-based fiber optic refractometers reported in the literature.

C. İDE, is with Department of Electrical-Electronics Engineering University of Izmir Institute of Technology, Izmir, Turkey, (e-mail: cansuide@iyte.edu.tr)

K. YÜKSEL, is with Department of Electrical-Electronics Engineering University of Izmir Institute of Technology, Izmir, Turkey, (e-mail: kivilcimyuksele@iyte.edu.tr)

Manuscript received May 30, 2018; accepted June 16, 2018.

DOI: [10.17694/bajece.428800](https://doi.org/10.17694/bajece.428800)

In the literature, for the methods based on conventional single-wavelength OTDR scheme, the separation of different sensor points is limited by the OTDR's dead zone. Hence, the multi-point measurement capability remains as a critical issue. This problem was addressed by our previous work [4] presenting a limited number of proof-of-concept measurements. Thanks to this approach, where a multi-wavelength OTDR is used for measuring the modified optical power of the light reflected from the sensing probes, the spatial resolution of OTDR does not limit the distances between sensors point.

In the present work, we elaborated our previously proposed method taking into account all the practical parameters such as real concentration values of the solutions as well as the effective refractive indices of the sensor tips at the measurement wavelength range. We investigated the refractive indices of common solvents, glycerin-water, and alcohol-water solutions in the infrared wavelength region (used in fiber-optic telecommunications). Moreover, our proposed method was extensively supported by a considerable amount of measurements including long-term repeatability tests. Comparison of the experimental results with that of theoretical calculations presented a good agreement. This shows a great potential of the system in a wide panel of applications requiring the self-calibration and easy implementation features, particularly those in difficult environments.

II. SENSING PRINCIPLE OF FRESNEL REFLECTION-BASED REFRACTIVE INDEX SENSOR

The operation principle of the proposed sensor was based on the measurement of Fresnel-reflection coefficient at the interface between the optical fiber and the sample. In this sensor, conventional single mode fiber tips were used as sensing points and a multi-wavelength OTDR was used as interrogation unit.

At the fiber end (flat cleaved fiber end) where the index of refraction differs, a small portion of the incident light is reflected back into the fiber. Power reflection coefficient R of this Fresnel reflected light can be quantified by the following expression at the interface between fiber end and air:

$$R = \left(\frac{n_1 - n_2}{n_1 + n_2} \right)^2 \quad (1)$$

Where n_1 is the effective refractive index of the fiber, and n_2 is the refractive index of the second medium which is air in this case ($n_2 = n_{air} = 1.0002739$) [5]. Power reflection coefficient can

be measured by using an optical time domain reflectometer (OTDR) as represented in Fig. 1.

TABLE I
SUMMARY OF THE FRESNEL REFLECTION-BASED REFRACTOMETERS

Source	Interrogator	Sensitivity	Precision	Ref.
Diode laser (modulated by a pulse train)	Photodetector and computer	-	2.5×10^{-5}	[6]
Diode laser (modulated by a pulse train)	Photodetector and digital oscilloscope	-	Short-time: 2.8×10^{-6} Long time: 2.9×10^{-5}	[7]
Broadband Source (centered at 1550 nm)	Photodetector	-	Short-time: 8×10^{-6} Long-time: 5×10^{-5}	[8]
Broadband Source (centered at 1538 nm)	OSA	55.2 dB/RIU to 148.1 dB/RIU	-	[9]
Laser diode (at 635 nm)	Photodetector	-	10^{-4}	[10]
OTDR's light source	Commercial OTDR (1550 nm)	38.70 dB/RIU to 304.73 dB/RIU	Long-time: 2.9×10^{-5}	[11, 12]
OTDR's light source	Multi-wavelength OTDR and AWG (1550 nm and 1625 nm)	-	4.7×10^{-4}	This work

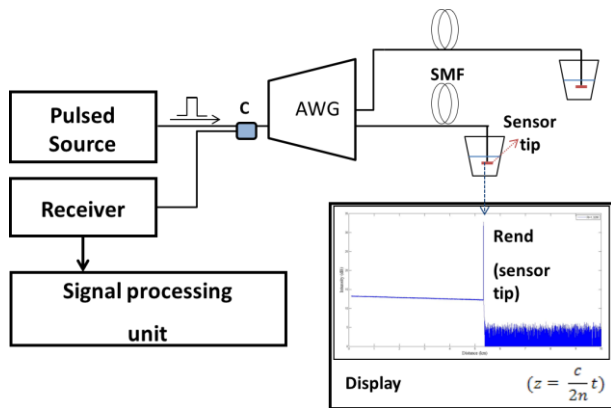


Fig. 1. Refractive index measurement using OTDR. AWG: Array Waveguide Grating

The amount of reflected light can be calculated by the differences in the refractive index of the two fibers joined, or any sample (air or chemical) at the end of the fiber. When the fiber tip is immersed into the liquid sample as shown in Fig. 1, the RI value of the liquid can be determined by measuring the end reflection peak (R_{end}):

$$n_2 = n_1 \frac{[1 - 10^{R_{end}/20}]}{[1 + 10^{R_{end}/20}]}, \quad n_1 > n_2 \quad (2)$$

$$n_2 = n_1 \frac{[1 + 10^{R_{end}/20}]}{[1 - 10^{R_{end}/20}]}, \quad n_1 < n_2 \quad (3)$$

The effective refractive index of the fundamental mode (n_1 or n_{eff}) was obtained as $n_1 = 1.4473$ at 1550 nm, and $n_1 = 1.4463$ at 1625 nm. In the case of each wavelength (1550 nm, 1625 nm) the very well-known Sellmeier equation given in (4) was implemented for the sensor fiber (4.5% GeO_2 doped silica fiber) [6, 13, 14].

$$n^2 = 1 + \sum_{i=1}^3 \frac{A_i \lambda^2}{\lambda^2 - B_i^2} \quad (4)$$

III. EXPERIMENTS

The glycerin-pure water solutions having different concentration levels were used to obtain the calibration characteristics of the Fresnel-based refractive index sensor. Reference measurements were realized with a conventional refractometer (model: RE50 digital refractometer). Fig. 2 represents the relation between the concentration values and the corresponding refractive indices of the glycerin-distilled water measured by the RE50 digital refractometer. Refractometer's light source emits at 589.3 nm.

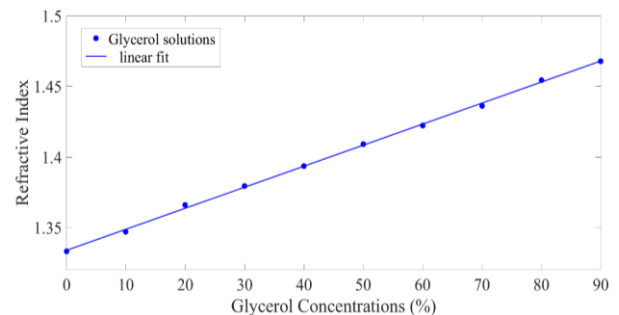


Fig. 2. Measured refractive indices of the glycerin-distilled water solutions

The fitting function of Fig. 2 is $n = 0.0014904 \times C + 1.3337$, having a fitting degree of $R^2 = 0.9999$.

In the experiments, two fiber tips were simultaneously used as sensing points. The optical pulses sent by the interrogation unit (Multi-wavelength OTDR) at two wavelengths (1550 nm and 1625 nm) were separated by a WDM coupler. The fiber tips were standard single mode fibers without the jacket (cut perpendicularly to the fiber axis by using a cleaver).

OTDR parameters set during the measurements are listed in Table II.

TABLE II
OTDR PARAMETERS

Parameter	Value
Distance range	10 km
Averaging time	15 secs
Pulse width	5 ns

The experiments were realized in two sections:

- **SET-1:** The sensor tip at 1550 nm was immersed in glycerin solutions prepared at different concentrations, while a second sensor tip at 1625 nm was kept in pure water.
- **SET-2:** The sensor tip at 1625 nm was immersed in glycerin solutions prepared at different concentrations, while a second sensor tip at 1550 nm was kept in pure water.

In both cases, the reflection coefficients from sensor tips were measured on the OTDR display. As an example, the change of end reflection peak for three different glycerol concentration values (20%, 30%, and 40%) is shown in Fig. 3.

Once the calibration characteristics had been obtained for both sensor tips, additional experiments were realized to measure the refractive indices of some chemicals such as acetone, isopropyl alcohol, methanol and ethanol.

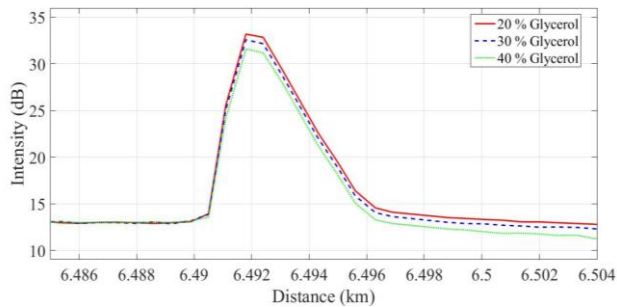


Fig.3. Enlarged view of the reflection from the sensor tip when the fiber is exposed to 20%, %30, and 40% glycerol solutions

IV. ANALYSIS OF EXPERIMENTAL RESULTS

Based on the measured reflection coefficient from the sensor tips, the refractive indices of the prepared solutions were calculated using Eq. (2) and (3). Table III and IV show R_{end} values measured at different wavelengths (at 1550 nm and 1625 nm), together with the calculated refractive indices using these R_{end} and n_1 values.

The absence of highly sensitive test equipment (e.g. electronic micropipette) prevented the preparation of the solution at the pre-determined concentration values. To overcome this limitation, the actual amount of concentration of the prepared chemicals were determined using the RI values measured by RE50 digital refractometer of distilled water, pure glycerin and related chemical (Eq. (5)). These concentration amounts were then used to determine the refractive indices of the solutions at 1550 nm. Conversion of the refractive indices of the chemicals at 589 nm to that of at 1550 nm was realized based on the refractive index values of distilled water and glycerin at 1550 nm given in the literature [15].

The real concentration values (X_{real}) of a glycerin-water solution at different wavelengths were obtained as:

$$n_x(\lambda) = \frac{(n_{pure_glycerin}(\lambda) \times X_{real}) + (n_{water}(\lambda) \times (100 - X_{real}))}{100} \quad (5)$$

A numerical example for determining the exact concentration value of 70% glycerin solution for 589.3 nm: $n_{water} = 1.33300$, $n_{pure_glycerin} = 1.47332$ and $n_x = 1.43612$ at 589.3 nm. From Eq. (5) X_{real} was found to be $X_{real} = 73.489\%$.

The refractive index value of 73.489% glycerine-water solution at 1550 nm was then calculated to be $n_x = 1.419799 \approx 1.4198$ using: $n_{water} = 1.3164$ and $n_{pure_glycerin} = 1.4571$ (at 1550 nm).

TABLE III
EXPERIMENTAL RESULTS AND REFERENCE RI VALUES FOR GLYCEROL SOLUTIONS (SET-1)

Concentrations		Reference RIs		R_{end} (dB)	Calculated RIs at $\lambda = 1550$ nm, $n_1 = 1.4473$
Originally aimed %	Real %	$n(\lambda)$ $\lambda = 589.3$ nm	$n(\lambda)$ $\lambda = 1550$ nm		
Air	-	1.00027	-	- 16.35	$1.0649 \pm 3.85 \times 10^{-3}$
Water	-	1.33300	1.3164	- 27.70	$1.3327 \pm 1.25 \times 10^{-3}$
10	9.999	1.34703	1.3305	- 28.80	$1.3459 \pm 1.10 \times 10^{-3}$
20	23.425	1.36587	1.3494	- 30.80	$1.3662 \pm 0.95 \times 10^{-3}$
30	33.089	1.37943	1.3630	- 32.00	$1.3764 \pm 0.80 \times 10^{-3}$
40	43.052	1.39341	1.3770	- 34.00	$1.3907 \pm 0.65 \times 10^{-3}$
50	48.439	1.40097	1.3846	-	-
60	63.626	1.42228	1.4059	- 38.40	$1.4129 \pm 0.40 \times 10^{-3}$
70	73.489	1.43612	1.4198	- 41.60	$1.4234 \pm 0.30 \times 10^{-3}$
75	78.328	1.44291	1.4266	- 43.80	$1.4287 \pm 0.20 \times 10^{-3}$
84	85.640	1.45317	1.4369	- 48.70	$1.4367 \pm 0.10 \times 10^{-3}$
86	86.959	1.45502	1.4388	- 49.40	$1.4375 \pm 0.10 \times 10^{-3}$
87	88.783	1.45758	1.4413	- 50.50	$1.4387 \pm 0.10 \times 10^{-3}$
88	90.287	1.45969	1.4434	- 52.00	$1.4400 \pm 0.05 \times 10^{-3}$
90	96.045	1.46777	1.4515	- 58.97	$1.4506 \pm 0.05 \times 10^{-3}$
100	-	1.47332	1.4571	- 52.23	$1.4544 \pm 0.05 \times 10^{-3}$

TABLE IV
EXPERIMENTAL RESULTS AND REFERENCE RI VALUES FOR GLYCEROL SOLUTIONS (SET-2)

Concentrations		n(λ) λ = 589.3 nm	R _{end} (dB)	Calculated RIs at λ = 1625 nm, n ₁ = 1.4463
Originally aimed %	Real %			
Air	-	1.00027	- 16.40	1.0660 ± 3.80 x 10 ⁻³
Water	-	1.33300	- 28.10	1.3368 ± 1.20 x 10 ⁻³
10	9.999	1.34703	- 28.50	1.3415 ± 1.15 x 10 ⁻³
20	23.425	1.36587	- 29.70	1.3546 ± 1.00 x 10 ⁻³
30	33.089	1.37943	- 31.00	1.3670 ± 0.90 x 10 ⁻³
40	43.052	1.39341	- 32.70	1.3808 ± 0.75 x 10 ⁻³
50	48.439	1.40097	- 34.30	1.3916 ± 0.60 x 10 ⁻³
60	63.626	1.42228	- 38.40	1.4119 ± 0.40 x 10 ⁻³
70	73.489	1.43612	-	-
75	78.328	1.44291	- 43.90	1.4280 ± 0.25 x 10 ⁻³
84	85.640	1.45317	- 51.45	1.4386 ± 0.10 x 10 ⁻³
86	86.959	1.45502	-	-
87	88.783	1.45758	- 54.10	1.4406 ± 0.10 x 10 ⁻³
88	90.287	1.45969	- 57.75	1.4426 ± 0.05 x 10 ⁻³
90	96.045	1.46777	- 59.85	1.4492 ± 0.05 x 10 ⁻³
100	-	1.47332	- 54.84	1.4515 ± 0.05 x 10 ⁻³

In the Table III and IV calculated RIs were given by adding the OTDR’s precision (± 0.1 dB). A systematic difference between the measured and the theoretical R_{end} values was observed. This difference can be attributed to the OTDR’s optical return loss (ORL) measurement accuracy, which is ± 1 dB.

The RI values obtained by using the proposed method versus reference refractive index values calculated for 1550 nm (for experimental Set-1 at 1550 nm) are represented in Fig. 4. The slope of the linear fit is: 0.83901. The fitting function is $n = 0.83901 \times \text{REF} + 0.23157$, with a fitting degree of $R^2 = 0.9973$, norm of residuals = 0.0074. The corrected version based on the OTDR’s ORL accuracy was plotted on a new graph (Fig. 5) and the slope closer to 1 was obtained. The slope of the linear fit is: 0.93735. The fitting function on this new graph was obtained as $n = 0.93735 \times \text{REF} + 0.089037$, having a fitting degree of $R^2 = 0.9975$, and norm of residuals = 0.0081.

It was observed that the refractive index differences occurred between the reference and the calculated values decreased as the refractive index of the external medium becomes closer to the effective refractive index value of the core (cf. Table III and IV).

The refractive index of the materials depends on the wavelength of the light source used for the measurement, as well as on the temperature.

For most of the liquids, the temperature dependence of the refractive index ($\partial n / (\partial T)$) is $10^{-4} \text{ } ^\circ\text{C}^{-1}$ [16]. The temperature variation of the laboratory was maximum 1 – 2°C during the whole experiments, therefore the influence of temperature could be ignored for measurements.

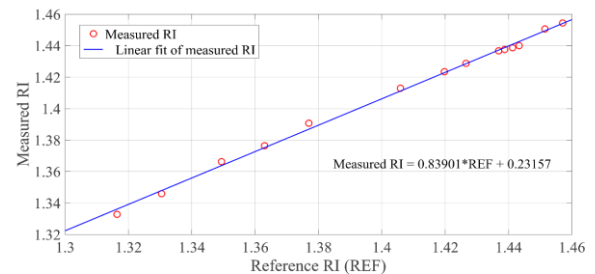


Fig.4. The reference refractive index values (at 1550 nm) vs the refractive index values (at 1550 nm) calculated using the proposed method

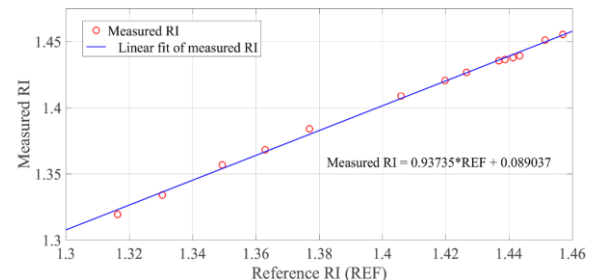


Fig.5. The reference refractive index values (at 1550 nm) vs the refractive index values (at 1550 nm) calculated using the corrected R_{end} values

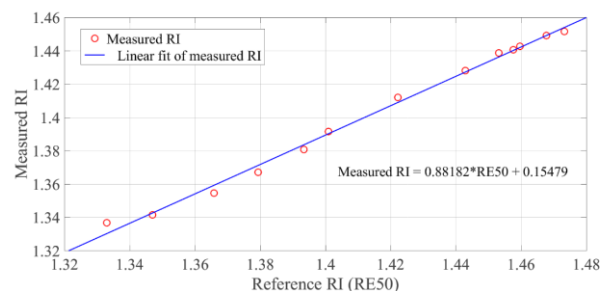


Fig.6. The reference refractive index values (at 589 nm) vs the refractive index values (at 1625 nm) calculated using the proposed method

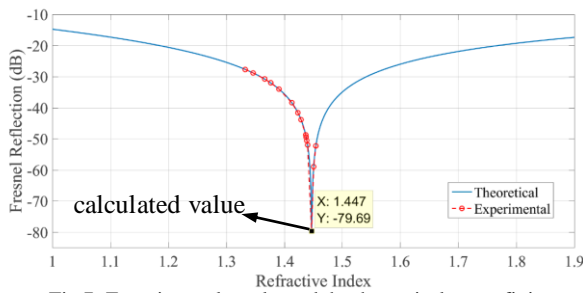


Fig.7. Experimental results and the theoretical curve fitting

Fig. 7 shows the experimental results (at $\lambda=1550$ nm) and the theoretical curve fitting these experimental points in the same graph.

The experimental results obtained for various chemicals such as ethanol, methanol, acetone and iso-propanol are presented in Table V. The differences between the values were in the second digit after the decimal point. The measurements were repeated three times to determine the measurement precision. The repeated measurements for acetone is listed in Table VI, where the standard deviation (precision) was obtained as 4.7×10^{-4} .

TABLE V
EXPERIMENTAL RESULTS AND REFERENCE RI VALUES FOR VARIOUS CHEMICALS

Chemical	Reference RIs ($n(\lambda)$)		Experimental RIs At 1550 nm	Δn
	At 589 nm	At 1550 nm		
2-propanol	1.3772	1.3661	$1.3756 \pm 0.80 \times 10^{-3}$	0.95×10^{-2}
Ethanol	1.3614	1.3522	$1.3624 \pm 0.95 \times 10^{-3}$	1.02×10^{-2}
Acetone	1.3586	1.3483	$1.3605 \pm 0.95 \times 10^{-3}$	1.22×10^{-2}
Methanol	1.3284	1.3174	$1.3556 \pm 1.05 \times 10^{-3}$	3.82×10^{-2}

TABLE VI
DETERMINATION OF SENSOR PRECISION

Number of measurement	R_{end} (dB)	$n_1 = 1.4463$	Deviation of each point
1	- 29.9	1.3566	0.0003
2	- 29.9	1.3566	0.0003
3	- 29.8	1.3556	0.0007

V. DISCUSSION & CONCLUSION

Requirements for quality standards in different areas, and increased public awareness have created a need for more reliable, faster, automated, remote and/or portable refractive index sensors and monitoring systems with multi-measurement capability. Fiber-based RI sensors provides attractive solutions in this area.

The measurement of refractive indices of common solvents in the range of telecommunication wavelengths is becoming critical due to the growing interest in fiber optic sensing at telecommunication wavelength range [17].

The aim of this work is to meet the calibration requirements of RI sensors that operate in the infrared wavelength range.

We provided a straightforward solution to this requirement using a conventional tool (OTDR) as the sensor interrogation unit.

Indeed, the wavelength range implemented in most of the fiber-based sensors and applications is within the classical telecommunication wavelength region as the commercial opto-electronic devices are readily available with reasonable prices. OTDR is one of them. On the current marketplace, one can easily find out a hand-held OTDR emitting at two wavelengths at reasonable prices. This opportunity is largely due to the emerging deployment (and related testing requirements) of optical fibre, particularly in the broadband access networks (e.g. NG-PONs). Hence, the proposed method based on OTDR provides cheap and easy RI measurement capability eliminating all expensive devices (lock-in amplifier, fast pulse modulation of laser source, fast detectors, GHz oscilloscopes...) and custom fibers (photonic crystal, microfiber, plastic optical fibers, SPR) reported in the previous literature.

The refractive index sensor investigated in this study is based on Fresnel reflection which uses SMF fiber tip as sensing point interrogated by an OTDR (operating at two different telecom wavelengths) from a distant location. Experimental work realized on different concentrations of glucose-water and glycerol-water solutions successfully demonstrated the capability of the proposed sensor in measuring RI of liquid chemicals with a precision of 4.7×10^{-4} . We provided substantial amount of measurements of refractive indices of common solvents and solutions at both 1550 nm and 1625 nm using a systematical and comparative approach.

Compatibility of the proposed sensor with the classical telecommunication wavelength range test equipment is the key advantage. Processing method used in the experiments (in calculating real concentration values of the solutions and determination of effective refractive index of the sensor tip) would serve as a reference for future investigations in this domain.

A wide panel of applications can be envisaged for the proposed sensor system, particularly those in difficult environments, requiring the self-calibration, easy implementation, multi-point, and remote measurement features.

ACKNOWLEDGMENT

The paper was supported by the Izmir Institute of Technology (IZTECH) under the Scientific Research Project (BAP-2016-IYTE-50). The authors would like to thank Dr. Burcu Okuklu (IYTE Food Engineering Department) for reference RI measurements using conventional refractometer.

REFERENCES

[1] J. Oelhafen, T. Mayr, F. Dörner, K. Moutzouris, J. Roths, K. Drechsler, "Fiber Optic Measurement System for Fresnel Reflection Sensing: Calibration, Uncertainty, and Exemplary Application in Temperature-Modulated Isothermal Polymer Curing", Journal of Lightwave Technology, Vol.36, No.4, February 2018, pp.939 - 945.
 [2] G. An, X. Hao, S. Li, X. Yan, X. Zhang, "D-shaped photonic crystal fiber refractive index sensor based on surface plasmon resonance", Applied Optics, Vol.56, No.24, 2017, pp.6988-6992.

- [3] I.D. Villar, J.L. Cruz, A.B. Socorro, S. Diaz, J.M. Corres, F.J. Arregui, I.R. Matias, "Monitoring the Etching Process in LPFGs towards Development of Highly Sensitive Sensors", *Proceedings*, Vol.1, No.4, 2017, pp.331-334.
- [4] K. Yüksel, "Optical fiber sensor system for remote and multi-point refractive index measurement", *Sensors and Actuators A: Physical*, Vol.250, 2016, pp.29-34.
- [5] R. C. Weast, S. M. Selby (ed), *Handbook of Chemistry and Physics*, (48th edition), CRC Handbook of Chemistry and Physics Press, 1968.
- [6] C.-B. Kim, C.-B. Su, "Measurement of the refractive index of liquids at 1.3 and 1.5 micron using a fibre optic Fresnel ratio meter", *Measurement Science and Technology*, Vol.15, No.9, 2004, pp.1683-1686.
- [7] A. Basgumus, F.E. Durak, A. Altuncu, G. Yilmaz, "A universal and stable all-fiber refractive index sensor system", *IEEE Photonics Technology Letters*, Vol.28, No.2, 2015, pp.171-174.
- [8] W. Xu, X.G. Huang, J.S. Pan, "Simple fiber-optic refractive index sensor based on Fresnel reflection and optical switch", *IEEE Sensors Journal*, Vol.13, No.5, 2013, pp.1571-1574.
- [9] C.-L. Zhao, J. Li, S. Zhang, Z. Zhang, S. Jin, "Simple Fresnel reflection-based optical fiber sensor for multipoint refractive index measurement using an AWG", *Photonics Technology Letters*, Vol.25, No.6, 2013, pp.606-608.
- [10] R. Selvas-Aguilar, A. Castillo-Guzman, L. Cortez-Gonzalez, et al., "Noncontact Optical Fiber Sensor for Measuring the Refractive Index of Liquids" *Journal of Sensors*, Vol.2016, Article ID 3475782, 2016, 6 pages.
- [11] C.-H. Yeh, C.-W. Chow, J.-Y. Sung, P.-C. Wu, W.-T. Whang, F.-G. Tseng, "Measurement of organic chemical refractive indexes using an optical time-domain reflectometer", *Sensors*, Vol.12, No.1, 2012, pp.481-488.
- [12] J.-Y. Yuan, C.-L. Zhao, M. Ye, J. Kang, Z. Zhang, S.-Z. Jin, "A Fresnel reflection-based optical fiber sensor system for remote refractive index measurement using OTDR", *Photonic Sensors*, Vol.4, No.1, March 2014, pp. 48-52.
- [13] O.V. Butov, K.M. Golant, A.L. Tomashuk, M.J.N. van Stralen, A.H.E. Breuls, "Refractive index dispersion of doped silica for fiber optics", *Optics Communications*, Vol.213, 2002, pp.301-308.
- [14] Y. Kang, *Calculations and Measurements of Raman Gain Coefficients of Different Fiber Types*, MSc Thesis, Virginia Polytechnic Institute and State University, 2002.
- [15] J.E. Saunders, C. Sanders, H. Chen, H.-P. Look, "Refractive indices of common solvents and solutions at 1550 nm", *Applied Optics*, Vol.55, No.4, 2016, pp.947-953.
- [16] J.-H. Chen, X.-G. Huang, W.-X. He, J. Tao, "A parallel-multipoint fiber-optic temperature sensor based on Fresnel reflection", *Optics & Laser Technology*, Vol.43, No.8, 2011, pp.1424-1427.
- [17] H. Apriyanto, G. Ravet, O.D. Bernal, M. Cattoen, H.C. Seat, V. Chavagnac, F. Surre, J.H. Sharp, "Comprehensive Modeling of Multimode Fiber Sensors for Refractive Index Measurement and Experimental Validation", *Scientific Reports*, Vol.8, Article number: 5912, 2018.



KIVILCIM YÜKSEL ALDOĞAN received the M.S. degrees in electronics engineering from the Ege University, in 2000 and the Ph.D. degree in applied sciences from Mons Engineering Faculty, Mons, Belgium, in 2011. Between 2002 and 2005, she worked at Multitel asbl (Belgium),

Applied Photonics Department, as an optical research engineer.

Afterwards, she worked as a research assistant at University of Mons (UMONS, Belgium) until 2012.

From 2012 up to date, she has been an Assistant Professor at the İzmir Institute of Technology. Her research interests include Rayleigh-based reflectometry techniques and their applications to fiber optic sensors, fiber Bragg grating sensors, monitoring of optical access networks, and development of innovative traffic monitoring solutions.

BIOGRAPHIES



CANSU İDE. She received the B.S. degree in physics engineering from Hacettepe University, in 2011 and M.S. degree in electrical - electronics engineering from Izmir Institute of Technology University, in 2017.

From 2014 up to date, she has been a research and development engineer at Ermaksan Optoelectronics R&D Center. Her research interests include fiber optic sensors, optical fiber gratings, structural health monitoring, high power fiber lasers and laser diodes.

FSRFT Based Broadband Double Matching via Passband Extremums Determination

R. Koprü, Member IEEE

Abstract— Fast simplified real frequency technique (FSRFT) is a numerical solver used to solve microwave broadband double-matching (DM) circuit design problems in a much faster and effective manner. Recently, it has been reported that an FSRFT based Matlab code can complete the design of a $n = 6th$ order lowpass lumped element double matching network to match a given generator and load impedance within an optimization time of only 0.6 seconds, a 47 fold less time than that of the same design done using the classical simplified real frequency technique (SRFT). FSRFT owes this superior speed performance to the fact that it tracks only $n + 1$ (system unknowns n plus 1) number of passband extremum points selected from among the nd number of gain data ($nd \gg n$). This work introduces a simple numerical technique called PED (passband extremums determination technique) to be used in determination of these passband extremum points (PEs). An exemplary $n = 6th$ order microwave bandpass DM circuit design using FSRFT based Matlab (of Mathworks Inc.) code and the simulation of this design via MWO (of AWR Corp.) has yielded the same circuit performance with an exact agreement. Thus, FSRFT, equipped with the PED, newly proposed hereby, might be used as a powerful solver in designing broadband circuits in many fields such as RF/microwave, radar, and communications.

Index Terms— Broadband matching, FSRFT-fast simplified real frequency technique-, lumped elements, scattering parameters.

I. INTRODUCTION

FSRFT, fast simplified real frequency technique, is a powerful RF/microwave design tool because of both its superior design completion speed and accuracy. Since its first introduction in [1], many RF/microwave filters and broadband matching network designs have been done by its author and the circuit performances yielded by FSRFT based Matlab [2] code have shown that these performances exactly agree with the results obtained from the simulations of the same circuits done via industry standard microwave packages such as MWO (Microwave Office) [3]. Design completion times are very small, even under sub-second times have been reported [1].

The major motivation in introducing of FSRFT in [1] was

R. KOPRÜ, is with Department of Electrical and Electronics Engineering, Isik University, Istanbul, Turkey, (e-mail: ramazan.koprü@isikun.edu.tr).

Manuscript received May 5, 2018; accepted July 23, 2018.
DOI: [10.17694/bajece.421266](https://doi.org/10.17694/bajece.421266)

several difficulties faced in the optimization based design of broadband matching circuits, such as *i) slow design times, ii) yielding different circuits depending on the different optimization initials*. All these difficulties have been overcome with ease by using FSRFT. FSRFT is fast, gives almost always the same circuit with any randomly chosen optimization initials.

FSRFT is essentially a faster variant of the classical SRFT (simplified real frequency technique). Some important works of the classical and recent literature on broadband double matching can be counted as given in [4-9]. Since its first introduction in 1982 [10], SRFT has always found an indispensable place to itself as a very powerful solver in many broadband matching design applications such as RF/microwave filters, matching networks, low and high power amplifiers, LNAs (low noise amplifiers) [1, 11-20].

Previously, an example design, given in the section V of [1], has been done using both SRFT and FSRFT for comparison purpose. It involves the design of a $n = 6th$ order lowpass equalizer, with $\epsilon = 0.333$, cut-off frequency $F_c = 1 \text{ GHz}$, generator impedance $Z_G = (R_G + L_G) || C_G$, load impedance $Z_L = (R_L + L_L) || C_L$, with $R_G = 12 \Omega$

$L_G = 3 \text{ nH}$, $C_G = 6 \text{ pF}$, $R_L = 34 \Omega$, $L_L = 4 \text{ nH}$, $C_L = 8 \text{ pF}$.

According to Table I of [1], FSRFT completes a typical double matching design problem in far less time, 0.6 seconds (vs ~29seconds) --47 fold less time compared to those of other solvers-, since the FSRFT uses only the amplitude extremums of the gain data. Thus, FSRFT can be thought as a far superior solver in terms of speed compared to the classical SRFT. An Intel 2.20 GHz i7 CPU with 8 GB RAM has been used as the computer running the experimental Matlab code [1].

Manual determination of PEs (passband extremums) and their entrance into the FSRFT based broadband double matching design code is a cumbersome process, thus, an algorithm for automatic determination of PEs is needed. Therefore, this work is devoted to present the PED (numerical passband extremums determination technique).

Organization of this paper is as follows: Section II gives a short review of broadband DM technique based on FSRFT as described in [1]. Section III introduces the newly proposed simple PED to be equipped into the FSRFT. Section IV presents a bandpass broadband DM design example solved via the FSRFT equipped with PED feature. Since a vast review of both SRFT and FSRFT has already been given in section II

and section III of [1], those who are not familiar with SRFT and FSRFT, are recommended to consult to [1] for a much more detailed knowledge. Thus, only some summarized parts of FSRFT taken from [1] are given in the following section.

II. REVIEW OF FAST SIMPLIFIED REAL FREQ. TECH. - FSRFT-

In classical literature, the problem of broadband double matching is described by “designing a 2-port matching network or equalizer in an arbitrary or predefined topology constructed with lossless elements such as lumped and/or distributed inductors, capacitors, transformers and transmission lines” [1,7]. An algorithm for double matching designs in accordance with the FSRFT is given in the following algorithmic steps. Notice that the following algorithm is a version that includes the BP (bandpass) DM designs whereas the one given in [1] was only for LP (lowpass) DM designs.

FSRFT Algorithm with PED for Broadband Double Matching

1) Enter the specs of the bandpass DM problem:

- passband ripple factor, equalizer order: ϵ, n
- begin and end freqs. of the optim. range (GHz): F_B, F_E
- lower and upper cut-off freqs. of the BP gain (GHz): F_L, F_H
- center freq. is computed as (GHz): $F_0 = \sqrt{F_L F_H}$

2) Enter the impedance data to be matched:

- impedance data: $Z_G(\omega_k), Z_L(\omega_k), \omega_k = 2\pi F_k$.
- frequency data: F_k (GHz), $k = 1, 2, \dots, nd$.

3) Generate normalized frequency and impedance data:

- freq. normalization factor: $\Omega = 2\pi F_0$, (Grad/s)
- norm. freq: $f_b = F_B/\Omega, f_l = F_L/\Omega, f_h = F_H/\Omega, f_e = F_E/\Omega$
- normalized center freq.: $\omega_0 = 2\pi(F_0/\Omega) = 1$ (rad/s)
- impedance norm. factor: $R_0 = 50 \Omega$
- norm. imp.: $z_G(\omega_k) = Z_G(\omega_k)/R_0, z_L(\omega_k) = Z_L(\omega_k)/R_0$.
- norm. freq.: $f_{k+1} = f_k + \Delta f, \Delta f = (f_2 - f_1)/(nd - 1)$.
- norm. complex fr.: $p_k = j\omega_k, \omega_k = 2\pi f_k, k = 1, 2, \dots, nd$

4) Generate target gain func. T_t to be tracked by the optimization:

$$T_t(\omega_k) = \frac{1}{1 + \epsilon^2 T_n(p_k)^2} \quad (1)$$

where $T_n(p_k)$ is an n th order Chebyshev function.

5) Construct “initial target data, ITD”:

$$ITD(k) = \{\omega_k, T_t(\omega_k), z_G(\omega_k), z_L(\omega_k)\}, k = 1, 2, \dots, nd$$

6) Form a “selected target data STD”:

STD is constructed from passband extremums (PEs) of ITD (initial target data) using the PED (passband extremums determination technique) proposed in this work (PED is explained in detail in section III)

$$STD(i) = \{\omega_i, T_t(\omega_i), z_G(\omega_i), z_L(\omega_i)\}, i = 1, 2, \dots, n + 1$$

Or, in terms of PEs, $STD(i) = \{PE(i), z_G(\omega_k), z_L(\omega_k)\}$.

7) Run the “constraint optimization” code

With the initial ‘unknowns’ vector $x_0 \leftarrow h$, call the optimization function $Opt_FSRFT(x)$,

$[x, f_{val}] = cons_optim('Opt_FSRFT', x_0, lb, ub)$ where lb and ub are lower and upper boundaries of the constraint optimization that can be set to sufficiently small values so as to make the optimization as fastly converging as possible.

8) Optimization function: $Opt_FSRFT(x)$:

- $h_i \leftarrow x_i, (i = 1, 2, \dots, n + 1)$.
- Set the polynomial $f = [0 \ 0 \dots \ 1 \dots \ 0 \ 0]$, i.e. midterm is 1.

$$f(p) = f_1 p^n + f_2 p^{n-1} + \dots + f_{ndc} p^{ndc} + \dots + f_{n+1} \quad (2)$$

where all $f_i = 0$, except $f_{ndc} = 1$. Note that ndc is the number of DC transmission zeros and generally chosen as $ndc = n/2$ to obtain a symmetrical bandpass gain shape.

- Calculate the even polynomials H, F, G by

$$H = hh^\dagger \quad (3)$$

$$F = ff^\dagger \quad (4)$$

$$G = H + F \quad (5)$$

$$G = gg^\dagger \quad (6)$$

where \dagger sign denotes “paraconjugate” of any polynomial $x(p)$, i.e. $x^\dagger = x(-p)$. The polynomial g must be a strictly Hurwitz polynomial for obtaining realizable networks and can be obtained from even polynomial G by

$$g = \sqrt{G(1)} poly(LHProots(G))$$

where $G(1)$ is the 1st coefficient of the polynomial G and $poly(LHProots(G))$ Matlab command represents a polynomial constructed of left half plane roots selected among the roots of the polynomial G . g is written in a form of [1, 7],

$$g(p) = g_1 p^n + g_2 p^{n-1} + \dots + g_n p + g_{n+1} \quad (7)$$

- Compute scattering matrix S in Belevitch form by

$$S = \begin{bmatrix} S_{11} & S_{12} \\ S_{21} & S_{22} \end{bmatrix} = \frac{1}{g} \begin{bmatrix} h & \mu f^\dagger \\ f & -\mu h^\dagger \end{bmatrix} \quad (8)$$

where μ is unimodular constant ($\mu = f^\dagger/f = \mp 1$) [1, 7]. In SRFT formalism, the ultimate aim of designing an equalizer is to be able to optimize the coefficients of the numerator polynomial $h(p)$ of the input reflection function

$$S_{11}(p) = h(p)/g(p) \quad (9)$$

- Compute the gain $T(\omega_i)$ via (10) or (11) as follows [1, 7],

$$T_G = (1 - |S_G|^2) \frac{|S_{21}|^2 (1 - |S_L|^2)}{|1 - S_{11} S_G|^2 |1 - S_2 S_L|^2} \quad (10)$$

$$T_L = (1 - |S_L|^2) \frac{|S_{12}|^2 (1 - |S_G|^2)}{|1 - S_{22} S_L|^2 |1 - S_1 S_G|^2} \quad (11)$$

obviously,

$$T = T_G = T_L \tag{12}$$

where

$$S_1 = S_{11} + \frac{S_{12}S_{21}S_L}{1 - S_{22}S_L}, \quad S_2 = S_{22} + \frac{S_{12}S_{21}S_G}{1 - S_{11}S_G} \tag{13}$$

and

$$S_G = \frac{Z_G - 1}{Z_G + 1}, \quad S_L = \frac{Z_L - 1}{Z_L + 1} \tag{14}$$

where S_{km} , ($k = 1,2; m = 1,2$) are the elements of the *unit-normalized scattering matrix* $[S]$ of the equalizer E. S_G and S_L are generator and load reflectances expressed in terms of generator and load impedances Z_G and Z_L [1, 7]. S_1 and S_2 are input and output reflectance functions, respectively, seen at the related port of the matching network when the other port is terminated with Z_L and Z_G , respectively [1, 21]. A much simpler and handy impedance based gain formulae which are equivalent to the reflectance based gain formulae given in (10) and (11) can also be used to calculate the gain such that [21]

$$T_G = \frac{4R_1R_G}{|Z_1 + Z_G|^2} = \frac{4R_1R_G}{(R_1 + R_G)^2 + (X_1 + X_G)^2} \tag{15}$$

$$T_L = \frac{4R_2R_L}{|Z_2 + Z_L|^2} = \frac{4R_2R_L}{(R_2 + R_L)^2 + (X_2 + X_L)^2} \tag{16}$$

- Compute error func.: $d_i = T(\omega_i) - T_t(\omega_i)$.
- optimization ends with success, $iff \{sse = \sum_{i=1}^{max} d_i^2\} \rightarrow \delta \sim 0$, yielding optimized polynomial h such that $h \leftarrow x_{opt}$. sse is known as 'sum of squared errors' [1].

9) Network Synthesis and Gain Plotting:

- Make the final design calculations repeating (2) to (16) using the optimized polynomial $h \leftarrow x_{opt}$.
- Compute the driving point input impedance $Z_{11}(p)$ of the equalizer by [1, 7]

$$Z_{11}(p) = \frac{a(p)}{b(p)} = \frac{g(p) + h(p)}{g(p) - h(p)} \tag{17}$$

where polynomials a and b are given in the form [1, 7]

$$a(p) = a_1p^m + a_2p^{m-1} + \dots + a_m p + a_{m+1} \tag{18}$$

$$b(p) = a_1p^n + a_2p^{n-1} + \dots + a_n p + a_{n+1} \tag{19}$$

- Polynomials $a(p)$ and $b(p)$ are entered into a Matlab based high precision synthesis package [22-24] which then extracts the schematic with element values of the designed equalizer.
- Plot $T(\omega)$ vs $T_t(\omega)$ to check if the gain performance

T of the designed equalizer agree well with the desired target gain T_t performance.

The equalizer designed in the Matlab environment [2] can be simulated in a commercial microwave package such as MWO [3].

III. PED - PASSBAND EXTREMUMS DETERMINATION TECH.

This section introduces the proposed PED (numerical passband extremums determination technique) which is embedded into the FSRFT. PED is a simple technique to find the passband extremums (PEs) of a given target gain function $T_t(\omega)$ for the DM system seen in Fig.1. In FSRFT, these $n + 1$ number of predetermined PEs are then tracked by the optimization algorithm to optimize the $n + 1$ number of coefficients h_i ($i = 1,2,\dots,n + 1$) of the polynomial $h(p)$ given in (2).

Fig.2 shows an example target gain function $T_t(\omega)$ with nd number of data ($nd \gg n$) generated by an n th order Chebyshev approximation using (1). Use of this target gain function in broadband equalizer design would elapse great time due to the fact that the optimization algorithm must track an nd number of data, $nd \gg n$, which is much greater than the order n of the equalizer to be designed. However, with FSRFT, the optimization algorithm has to track only $n + 1$ number of data which are predetermined at the exact positions or vicinity of the PEs of the target gain function. Tracking PEs

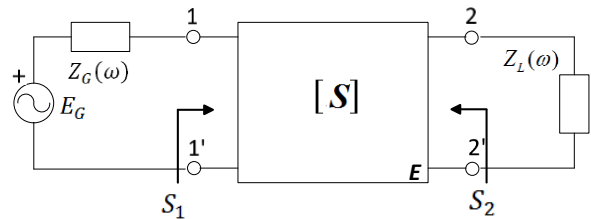


Fig.1. Broadband double matching problem.

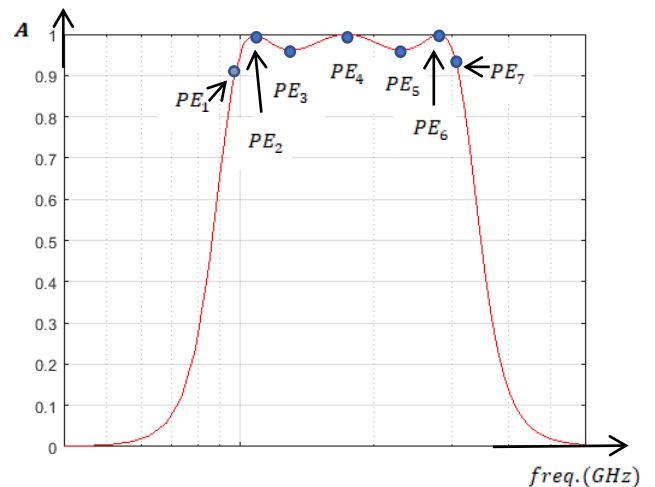


Fig.2. PED-passband extremums determination technique-: Chebyshev approximated n th order target gain function $T_t(\omega)$ is plotted (solid red line) with nd number of gain amplitudes A vs. $freq.$ ($nd \gg n$). $n + 1$ number of passband extremums PEs (blue dots) are determined at passband extremum points over the target gain function $T_t(\omega)$.

in the optimization process is very advantageous to reduce the optimization time because the PEs are already at the exact points where the solution of the system resides. “Therefore, selection of $n + 1$ number of frequency locations ω_i ($i = 1, 2, \dots, n + 1$) where the passband extremums $T_t(\omega_i)$ occur is naturally the wisest selection having a potential to hit the solution $h_{opt} \leftarrow x_{opt}$ as quick as possible” [1].

Passband extremums determination algorithm given below is a numerical method that uses a given target gain function $T_t(\omega)$ so that a pair of frequency and gain amplitude at each passband extremum of T_t function is calculated such that $PE_i = (\omega_i, T_t(\omega_i))$, $i = 1, 2, \dots, n + 1$. In the literature, available equations [7] can be used to find the passband extremums analytically for an n th order Chebyshev function, however the method presented here is a numerical one that might be used for a gain function with any arbitrary shape.

PED -Passband Extremums Determination- Algorithm

STEP 1. Enter the given target gain function T_t as a pair of frequency and gain amplitude at each k , i.e. $T_t(k) = T_t(\omega_k, A_k)$, $k = 1, 2, \dots, nd$. If the number of gain data nd is not sufficiently large (data number is close to the order n of the equalizer to be designed, i.e. $nd \cong n$, or less), apply an interpolation to obtain a gain function $T_t(k)$ with sufficiently large number of data such that $nd \gg n$, for instance $nd \geq 15(n + 1)$.

STEP 2. The first passband extremum $PE(1)$ is determined by the designer by examining the T_t gain plot (Fig.2) and it is chosen estimate at a frequency ω_k around where the passband begins as seen in Fig.2. Thus, $PE(1)$ is entered to the code as $PE(i) = T_t(k)$ for $i = 1$, or equivalently, $PE(\omega_i, A_i) = T_t(\omega_k, A_k)$ again for $i = 1$.

The frequency index k is increased by 1, i.e. $k \leftarrow k + 1$.

STEP 3. A 1st local slope is calculated as $m_1 = A_k - A_{k-1}$

The frequency index k is increased by 1, i.e. $k \leftarrow k + 1$.

A 2nd local slope is calculated as $m_2 = A_k - A_{k-1}$

The frequency index k is increased by 1, i.e. $k \leftarrow k + 1$.

STEP 4. If the product of two slopes satisfies $m_{12} = m_1 m_2 > 0$, this means that two successive slopes have the same direction indicating that this frequency point ω_k can not be a new extremum (PE). Then, goto STEP 3.

Otherwise, if $m_{12} = m_1 m_2 < 0$, this means that two successive slopes have opposite direction indicating that a new extremum (PE) is located at this frequency point ω_k . Then, increase i and assign $PE(i) = T_t(k)$.

If $i < n + 1$ Goto STEP 3, Otherwise goto STEP 5.

STEP 5. All passband extremums $PE(i)$, $i = 1, 2, \dots, n + 1$ have now been determined via the PED algorithm given in the above steps. Thus, continue the design from the Step 6 of the FSRFT Algorithm given in section III.

MATLAB CODE: A Matlab function developed using the PED algorithm given above is listed as follows:

```
global nd ki wnorm Tm
PE_i=zeros(1,n+1);% array that holds PE order
PE_f=zeros(1,n+1);% holds PE freq. (GHz)
PE_Tk=zeros(1,n+1);% holds PE amplitude

Fb=0.90;% GHz
Fe=3.2;% GHz
nd=300;
% designer must enter the 1st PE data as:
ki=53;%initial k
PE_i(1)=1;
PE_f(1)=f(ki)*wnorm;%
PE_Tk(1)=Tm(ki);%

[PE_i,PE_f,PE_Tk]= PED_func(PE_i,PE_f,PE_Tk);

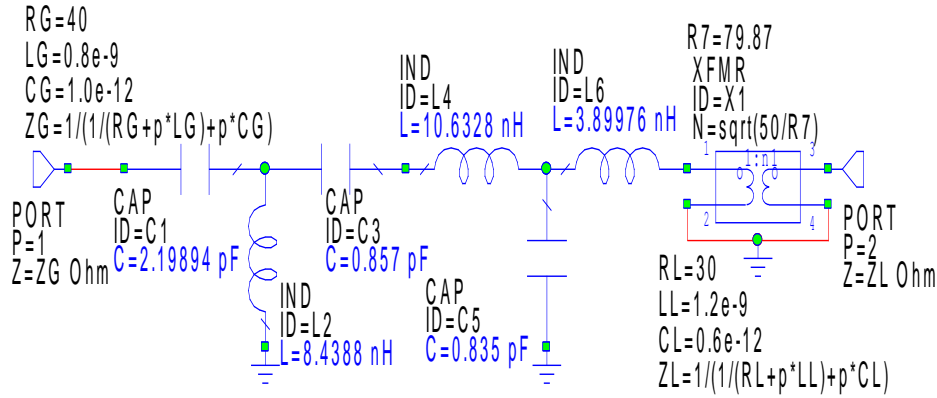
function
[PE_i,PE_f,PE_Tk]=PED_func(PE_i,PE_f,PE_Tk)
global nd ki wnorm Tm

i=1;
for k=ki:nd
k=k+1;
m1=Tm(k)-Tm(k-1);
k=k+1;
m2=Tm(k)-Tm(k-1);
m12=m1*m2;
if m12<0
i=i+1;
PE_i(i)=i;
PE_f(i)=f(k)*wnorm;
PE_Tk(i)=Tm(k);
end
end
end
```

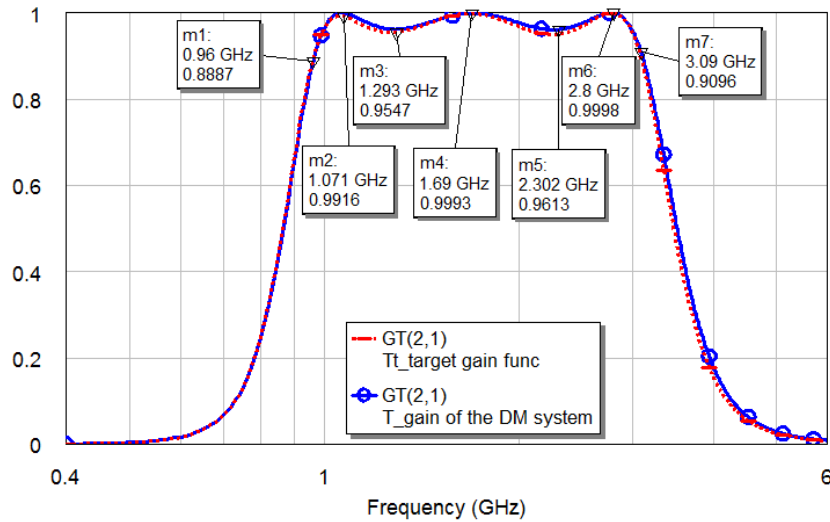
IV. DESIGN EXAMPLE

A bandpass double matching (DM) problem is given in this section and solved via FSRFT based on the proposed PED technique. A broadband design is to be done involving an $n = 6$ th order bandpass Chebyshev approximated lumped element equalizer, with passband ripple factor $\varepsilon = 0.20$, lower and upper cut-off frequencies of $F_L = 1$ GHz, $F_H = 3$ GHz, generator impedance $Z_G = (R_G + L_G) || C_G$, and load impedance $Z_L = (R_L + L_L) || C_L$, built of $R_G = 40\Omega$, $L_G = 0.8$ nH, $C_G = 1$ pF, $R_L = 30\Omega$, $L_L = 1.2$ nH, $C_L = 0.6$ pF
Solution via FSRFT with PED:

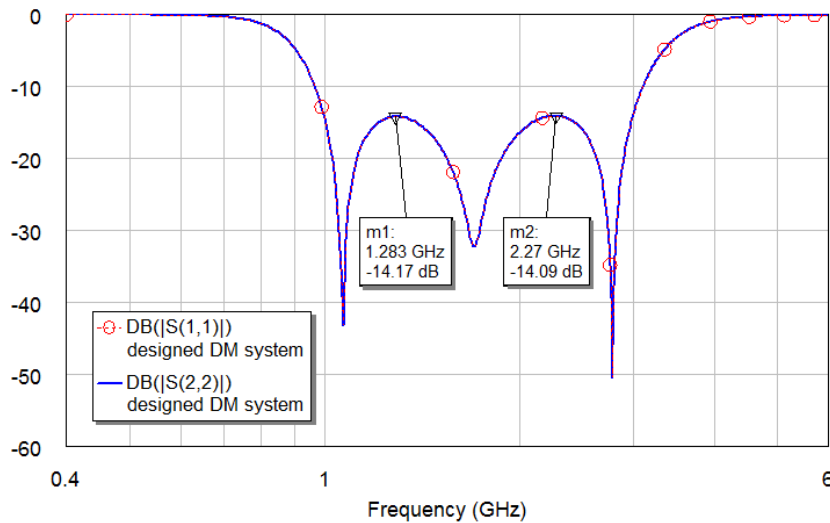
First, the optimization frequency range can be chosen for instance varying from $F_B = 0.9$ GHz upto $F_E = 3.2$ GHz. Using FSRFT algorithm given in section III, initial target data



a)



b)



c)

Fig.3. MWO [3] Simulation results of the example DM system design done via the Matlab code: a) overall circuit schematic of the DM system designed via the Matlab code is redrawn in MWO. b) gain performance of the DM system. c) input/output reflectance performance of the DM system.

set ITD is generated for the whole range of optimization frequencies $[F_B, F_E]=[0.9, 3.2]$ GHz, for example, $nd = 300$ freq. points, i.e. $ITD(k) = \{\omega_k, T_i(\omega_k), z_G(\omega_k), z_L(\omega_k)\}$, $k = 1, 2, \dots, k_{max} = nd = 300$. Therefore, the *PED Algorithm* given in section III, determines the indices of the passband extremums occurring at the indices of $k_{ext} = \{9, 23, 53, 109, 183, 249, 286\}$ whose element number is the equalizer order n plus 1, i.e. $n + 1 = 7$. Then the passband extremums are determined by the Matlab code *PED_func* as $PE(i) = T_i(k)$, $PE = \{PE_1, PE_2, PE_3, PE_4, PE_5, PE_6, PE_7\} = \{T_i(9), T_i(23), T_i(53), T_i(109), T_i(183), T_i(249), T_i(286)\}$, where $PE(i) = PE(f_i, A_i) = \{(0.960, 0.882), (1.07, 1.00), (1.296, 0.962), (1.688, 0.999), (2.304, 0.962), (2.808, 1.000), (3.088, 0.911)\}$, where all f_i frequencies are given in GHz. It is better to choose nd as large as possible, for instance $nd = 300$ to obtain accurate PE locations. Table I shows the determined PE list for $nd = 300$. The optimization range in determining the PEs of Table I has been chosen as $[F_B, F_E] = [0.90, 3.20]$ GHz. The selected target data set $STD(i)$ is then constructed by one to one mapping from $ITD(k)$ to $STD(i)$ yielding $STD(i) = \{PE(i), z_G(\omega_k), z_L(\omega_k)\}$.

TABLE I
PEs DETERMINED BY MATLAB FUNCTION *PED_FUNC()*

PE_i	f_i (GHz)	amplitude (A)
PE_1	0.960	0.884
PE_2	1.071	0.999
PE_3	1.303	0.962
PE_4	1.732	0.999
PE_5	2.303	0.962
PE_6	2.803	1.000
PE_7	3.088	0.911

Upon a successful optimization, the code yields the optimized polynomial as $h(p) = 0.352p^6 + 0.322p^5 + 1.216p^4 + 0.540p^3 + 1.216p^2 + 0.109p + 0.386$ with the polynomial $g(p) = 0.352p^6 + 1.009p^5 + 2.513p^4 + 3.044p^3 + 2.574p^2 + 1.029p + 0.386$ and $f(p) = p^3$. The designer having the optimized polynomial $h(p)$ given above, can reconstruct the equalizer circuit using only this polynomial $h(p)$ without reexecuting the optimization code at all but following only the remaining steps of the *FSRFT Algorithm* given in section II. Overall circuit schematic of the DM system (with the designed equalizer between the ports) is seen in Fig.3.a. In Fig.3.b and c, gain and input/output reflectance performance of the designed DM system are shown. Fig.3.b shows clearly that the gain performance of the designed DM system is in almost excellent agreement with that of the desired target gain function T_t . Notice that the measurement points marked by m_1, m_2, \dots, m_7 are the PEs of the system. Fig.3.c shows also that the input/output reflectance performance of the designed DM system is very well, around -14.1 dB pretty below -10 dB along the operating band.

FSRFT completes the solution of this broadband bandpass DM design problem within as low as only 0.58 seconds using only $n + 1 = 7$ number of PEs. The same computer, an Intel 2.20 GHz i7 CPU with 8 GB RAM, that has been used in the

previous work of [1] has been used as the computer running the experimental Matlab code here.

V. CONCLUSION

The proposed PED is a simple but very effective technique in determining the PEs which eases the design process of broadband DM system tremendously. The work presented here gives also the design method of broadband bandpass matching networks which are much more needed in wideband microwave amplifiers compared to their lowpass counterparts. Thus, need for bandpass designs using FSRFT has also been met with this work. With the addition of proposed PED feature here, FSRFT might be a good candidate to be a fast and effective design tool utilizable in broadband RF/microwave area.

REFERENCES

- [1] R. Kopru, "FSRFT—fast simplified real frequency technique via selective target data approach for broadband double matching", IEEE Transactions on circuits and systems-II: Express briefs, Vol. 64, No. 2, february 2017, pp.141-145.
- [2] Matlab, <https://www.mathworks.com> Mathworks Inc., MA., USA, retrieved on april 8, 2018.
- [3] MWO www.awrcorp.com, AWR Corp, retrieved on april 8, 2018.
- [4] H. J. Carlin, "A new approach to gain-bandwidth problems," *IEEE Trans. Circuits Syst.*, vol. 24, no. 4, pp. 170-175, Apr. 1977.
- [5] B. S. Yarman, "Broadband matching a complex generator to a complex load," Ph.D. dissertation, ECE Dept. Cornell Univ., NY, USA, 1982.
- [6] B. S. Yarman, Design of Ultra Wideband Antenna Matching Networks Via Simplified Real Frequency Techniques, Netherlands: Springer, 2008, pp. 183-225.
- [7] B. S. Yarman, *Design of Ultra Wideband Power Transfer Networks*, 1st ed., Chichester, UK.: John Wiley & Sons Ltd., 2010.
- [8] W. K. Chen, *Broadband Matching: Theory and Implementations*, 3rd ed., World Scientific, ISBN: 978-9971-5-0219-5, Nov. 1998.
- [9] Y. S. Zhu, W. K. Chen, *Computer-Aided Design of Communication Networks*, World Scientific, ISBN: 978-981-02-2351-9, April 2000.
- [10] B. S. Yarman and H. J. Carlin, "A simplified real frequency technique applied to broad-band multistage microwave amplifiers," *IEEE Trans. Microw. Theory Techn.*, vol. 30, no. 12, pp. 2216-2222, Dec. 1982.
- [11] L. Zhu, B. Wu, and C. Sheng, "Real frequency technique applied to synthesis of broad-band matching networks with arbitrary nonuniform losses for MMICs," *IEEE Trans. Microw. Theory Techn.*, vol. 36, no. 12, pp. 1614-1620, Dec. 1988.
- [12] P. Jarry and A. Perennec, "Optimization of gain and VSWR in multistage microwave amplifier using real frequency method," in *Proc. ECCTD*, Paris, FR., 1987, pp. 203-208.
- [13] R. Kopru, H. Kuntman, and B. S. Yarman, "On numerical design technique of wideband microwave amplifiers based on GaN small-signal model," *Analog Integr. Circ. Sig. Procc.*, vol. 81, no. 1, pp. 71-87, Jul. 2014.
- [14] G. Sun and R. H. Jansen, "Broadband doherthy power amplifier via real frequency technique," *IEEE Trans. Microw. Theory Techn.*, vol. 60, no. 1, pp. 99-111, Jan. 2012.
- [15] N. Tuffy, L. Guan, A. Zhu, and T. J. Brazil, "A simplified broadband design methodology for linearized high-efficiency continuous class-F power amplifiers," *IEEE Trans. Microw. Theory Techn.*, vol. 60, no.6, pp. 1952-1963, Jun. 2012.
- [16] Y. Sun and X. Zhu, "Broadband continuous class-F⁻¹ amplifier with modified harmonic-controlled network for advanced long term evolution application," *IEEE Microw. Compon. Lett.*, vol. 25, no.4, pp. 250-252, Jun. 2015.
- [17] L. Ma, J. Zhou, and W. Huang, "A broadband highly efficient harmonic-tuned power amplifier exploiting compact matching network," *IEEE Microw. Compon. Lett.*, vol. 25, no.11, pp. 250-252, Nov. 2015.
- [18] R. Kopru, H. Kuntman and B. S. Yarman, "Novel approach to design ultra wideband microwave amplifiers: normalized gain function method". Vol. 22, No. 3, pp. 672-686, September 2013, *Radioengineering*.

- [19] R. Koprü, S. Kılınç, C. Aydın, D. C. Atilla, C. Karakuş, B. S. Yarman, "Ultra wideband matching network design for a V-shaped square planar monopole antenna", *International Journal of Microwave and Wireless Technologies*, Cambridge Univ. Press, 2014, volume 6, issue 06, pp. 555-564.
- [20] R. Koprü, S. Kılınç, A. Aksen, and B. S. Yarman, "Design and implementation of wideband microwave amplifiers based on normalized gain function", *BenMAS2014, 2014 IEEE Benjamin Franklin Symposium on Microwave and Antenna Sub-Systems, Radar, Telecommunications, and Biomedical Applications*, September 27, 2014, Philadelphia, Pennsylvania, USA.
- [21] M. Sengul, "Design of practical broadband matching networks with lumped elements." *IEEE Trans. Circuits Syst. II, Exp. Briefs*, vol. 60, no. 9, pp. 552-556, Sep. 2013.
- [22] A. Kılınç and B. S. Yarman, "High precision LC ladder synthesis part I: Lowpass ladder synthesis via parametric approach," *IEEE Trans. Circuits Syst. I, Reg. Papers*, vol. 60, no. 8, pp. 2074-2083, Aug. 2013.
- [23] B. S. Yarman, and A. Kılınç, "High precision LC ladder synthesis part II: Immitance synthesis with transmission zeros at DC and infinity," *IEEE Trans. Circuits Syst. I, Reg. Papers*, vol. 60, no. 10, pp. 2719-2729, Oct. 2013.
- [24] B. S. Yarman, A. Aksen, R. Koprü, N. Kumar, C. Aydın, D. C. Atilla, P. Chacko, "Computer aided Darlington synthesis of an all purpose immittance function", *IU-JEEE Istanbul University Journal of Electrical and Electronics Engineering*, Vol. 16, No. 1, pp. 2027-2037, 2016.

power electronics, embedded systems, supercapacitors.

BIOGRAPHIES



RAMAZAN KOPRU received B.Sc. degree from Yildiz Technical University in 1991, M.Sc. and Ph.D. degrees from Istanbul Technical University, Turkey, in 1994 and 2013, respectively, all from electronics and communications engineering. In the past, he has worked as a research and development engineer in the fields of embedded systems, wireless systems, power electronics and

defense electronics. Since 2014, he has been an Assistant Professor with the Electrical and Electronics Engineering Department, Işık University, Istanbul, Turkey. He is the author/co-author of 41 articles published in international/national peer-reviewed journals and conferences. He is also the referee of many papers for the international peer-reviewed journals and conferences. His main research areas are military spec low noise wideband analog design for laser signal detection and post processing, wideband microwave low power and power amplifier design using real frequency techniques, network synthesis with lumped and distributed elements, fast circuit design methods for RF/microwave broadband matching using FSRFT, high voltage techniques, optimization, power system analysis,

Modelling and control of permanent magnet synchronous generator based on three level NPC using fuzzy PI

A. Gencer

Abstract— Recently, the permanent magnet synchronous generator (PMSG) has been gained attention by wind turbine (WT) manufactures due to advance of control system and power electronics. The permanent magnet synchronous generator based on three level neutral point control (NPC) system using fuzzy logic control proportional integral (FLC PI) is proposed in this study. The NPC systems of DC link are implemented more easily than two level systems. The NPC systems provide better harmonic reduction than conventional two level voltage source converters. The control strategies of the NPC systems reduce semiconductor losses. The proposed system can be implemented to the multi-level converters above three-level. The proposed system is developed using the steady state technique. The performance of the PMSG system under variation operation condition is investigated in this study and the performances of the PMSG based on three level NPC using FLC PI are analyzed. The validity of the proposed system is implemented and verified in the MATLAB/Simulink using three-level insulated gate bipolar transistor (IGBT) converter.

Index Terms— Permanent magnet synchronous generator (PMSG), wind turbine (WT), neutral point control (NPC) systems.

I. INTRODUCTION

RECENTLY, PMSG has been gained attention by wind turbine (WT) manufactures owing to improvement of control system and power electronics [1]. The variable speed WT provides more effective power available than constant speed. Therefore, the WT enhances to operate at variable speed value [2,3]. A control system is improved to available maximum power from the WT [4,5]. In addition, the control system supplies to required fixed frequency and voltage for the grid. Therefore, the PMSG is used for high efficiency and controllability in the variable speed WT systems [6]. The PMSG can be connected to the electrical grid by GSC systems [7]. However, these power electronic converters cause harmonic distortion for electrical grids.

A. GENCER is with Department of Electrical Engineering University of Nevsehir H.B.V., Nevsehir, Turkey, (e-mail: altangencer@nevsehir.edu.tr).

Manuscript received May 14, 2018; accepted June 10, 2018.
DOI: [10.17694/bajece.423464](https://doi.org/10.17694/bajece.423464)

In this study, a grid side converter for variable speed PMSG based on three level NPC is proposed. Three level NPC system has implemented to high power wind energy conversion system (WECS). One of the most important characteristics of the three level NPC system is providing better harmonic reduction than conventional two level voltage source converter. The control strategies of the NPC system reduce semiconductor losses. The aim of this paper is the controlling and dynamic modelling of WECS based on the PMSG. Moreover, both MSC and GSC system based on three-level NPC using FLC PI control are designed for the load systems. The validity of the proposed system is implemented and verified by MATLAB/Simulink using three-level NPC system.

The rest of the paper is organized as follows; Section 2 introduces of each element of the wind power system. The mathematical model for PMSG is introduced in Section 3. Block diagram of proposed PMSG based on WECS is given in Section 4. The simulation results of proposed protection system are presented in Section 5. Finally, conclusions are given in Section 6.

II. DYNAMIC MODEL OF WIND TURBINE

This section introduces mathematical model for each element of the wind power system, composed of WT, drive train, PMSG, electric grid, as given in Fig. 1. The PMSG is utilized as wind turbine generator type in this study. The PMSG without gearbox link to wind turbine and connected to electrical grid.

A. Wind turbine

Wind turbine converts wind power into mechanical rotate power. The wind turbine consists a classic three-bladed horizontal-axis. Used model in this paper has aerodynamic behaviors of wind turbine. Mechanical power obtained from wind turbine can be described as in Eq. (1) [1].

$$P_m = \frac{1}{2} \rho A C_p (\lambda, \beta) v^3 \quad (1)$$

where ρ depicts the air density, A shows the area swept by a classic three-bladed horizontal-axis, v is wind speed, λ and C_p denote the wind turbine blade tip speed ratio and power coefficient, respectively. λ expressed the aerodynamic

behaviors of the WT. The power coefficient C_p depicts a nonlinear function of the blade pitch angle β and the tip-speed ratio λ [1].

A wind turbine operates a wide range of wind speed value. Due to being very complex of the aerodynamic system in this operation conditions, results are difficult obtained as analytical.

B. Drive train for PMSG

The drive train of variable speed WECS is composed of the hub with blades, a rotor shaft, a blade-pitching mechanism with a spinner, and generator. The electromechanical torque is obtained from PMSG and the aerodynamic torque is acquired from rotor in the WT. Torque equations are given in Eq. (2) and Eq. (3) [1].

$$T_m = \frac{P_m}{\omega_r} \quad (2)$$

$$T_e = \frac{P_e}{\omega_e} = \frac{2}{P} \frac{P_e}{\omega_r} \quad (3)$$

In general, the mechanical equation of a PMSG is given in Eq.(4).

$$J \frac{d\omega_r}{dt} = T_m - B\omega_r - T_e \quad (4)$$

where ω_e represents electrical angular frequency of PMSG, P shows pole number of PMSG, J denotes inertia moment of PMSG and B is friction coefficient of the PMSG.

III. MATHEMATICAL MODEL OF PMSG

The mathematical model of PMSG can be used to simulate entire system. This model is required to control methods of the PMSG. This model aims to solve control problems as theoretical and analytical [1,4].

Two phase coordinate reference dq frame is quite simple according to real three phase abc frame. The dq frame has dc quantities under steady-state operation, while the abc frame appears as sinusoidal quantities. Therefore, two phase coordinate reference dq frame is widely used to control and simulation purposes rather than real three phase abc frame at reference rotate speed. Linear equations are obtained using the mathematical facilitation. Additionally, these equations simplify the decoupled control of active power and reactive power in three-phase systems [8].

The hysteresis losses, skin effect, magnetic saturation, and stator core losses are neglected in the most widely accepted PMSG model. PMSG voltage equations are expressed by[9]:

$$v_{sd} = R_s i_{sd} + L_d \frac{di_{sd}}{dt} - \omega_e \psi_{sq} \quad (5)$$

$$v_{sq} = R_s i_{sq} + L_q \frac{di_{sq}}{dt} + \omega_e \psi_{sd} \quad (6)$$

If the dq axes rotate at the synchronous speed and the d -axis is aligned with the rotor flux, the stator flux components are given by [9]:

$$\psi_{sd} = L_d i_{sd} + \psi_f \quad (7)$$

$$\psi_{sq} = L_q i_{sq} \quad (8)$$

As a result, the voltage equations in the dq synchronous reference frame are given as follows [9]:

$$v_{sd} = R_s i_{sd} + L_d \frac{di_{sd}}{dt} - \omega_e L_q i_{sq} \quad (9)$$

$$v_{sq} = R_s i_{sq} + L_q \frac{di_{sq}}{dt} + \omega_e L_d i_{sd} + \omega_e \psi_f \quad (10)$$

IV. PROPOSED SYSTEM FOR PMSG

Block diagram of proposed PMSG based on WECS is given in Fig. 1. A WECS based on PMSG consists of a WT connection to a drive train, a MSC connected with stator of PMSG and a GSC connected with the load. Three level NPC is utilized for MSC and GSC. The diode clamped topology is exploited for three level NPC in this study. The inputs of the PMSG are connected to drive train, blade and other mechanical systems in wind turbine. The outputs of the generator are connected to a MSC, DC link, a GSC, and load in the WECS, respectively.

A. Machine side converter and controller

The MSC and GSC scheme based on three levels NPC for PMSG is illustrated in Fig. 1. Three level NPC system has implemented to high power WECS. One of the most important characteristics of the three level NPC system is providing better harmonic reduction than conventional two level voltage source converter. The control strategies of the NPC system can reduce semiconductor losses. In order to achieve three steps in output AC voltages, two capacitors are employed in the three level NPC system [10].

Control block diagram of the MSC is given in Fig. 1. The controller structure of the MSC consists of two loops such as d and q loops controller. The operation of the MSC requires d and q loops of the reference frame that are determined by sustaining output of the stator and the output active power. For the reactive power compensated, stator current is controlled by d and q loops of the reference frame in the unity power factor control system. For generated maximum power torque of the generator, stator current in the maximum torque is controlled by only q loop [11,12]. However, rated power of the generator is surpassed due to the reactive power is not adjusted. The voltage waveforms of the MSC are acquired by equating the d and q loops of both reference and actual current values. The voltage waveforms are supplied voltage source PWM to maintain a constant switching frequency [12].

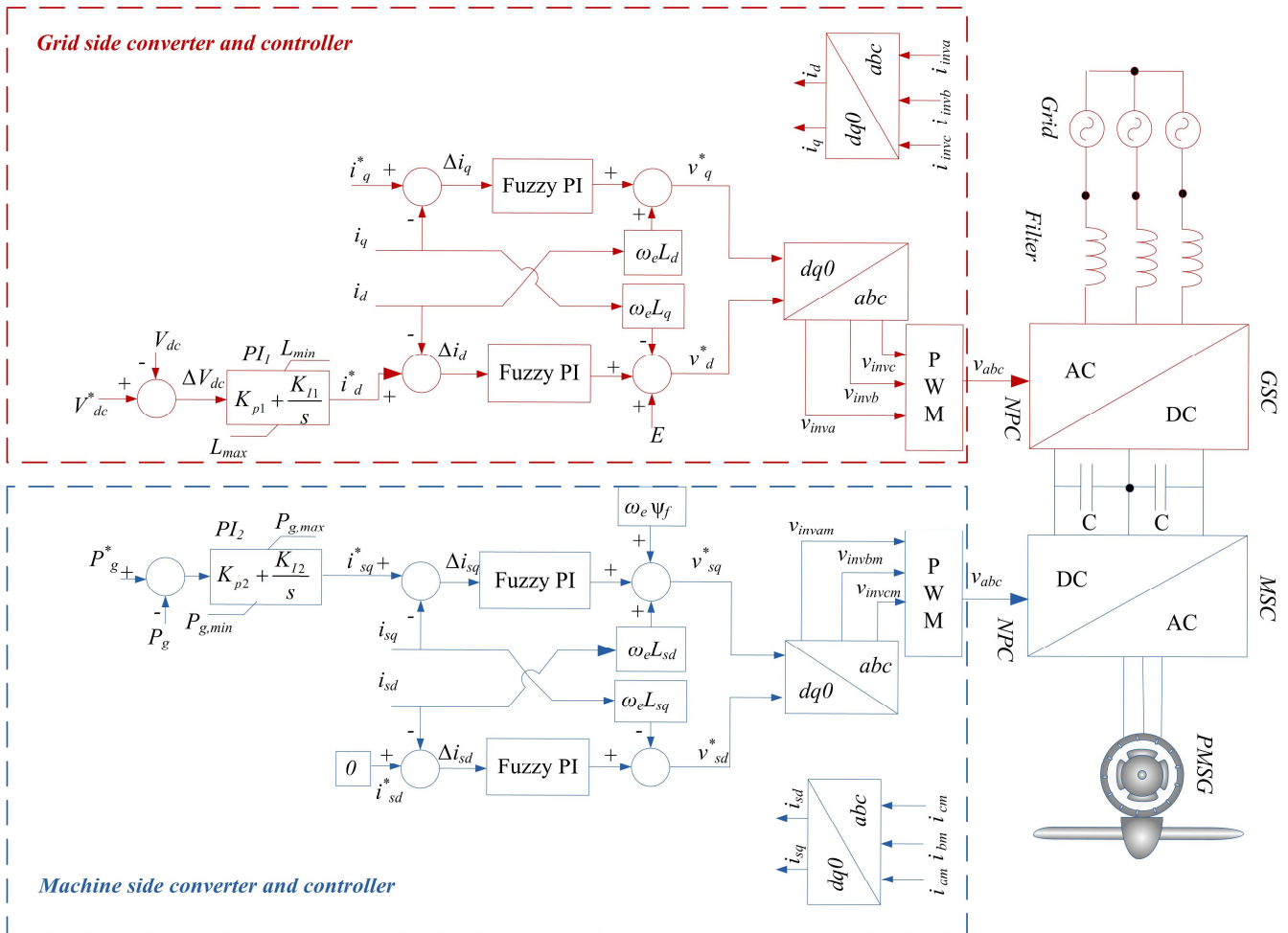


Fig.1. Permanent magnet synchronous generator system based on WECS

B. Grid Side Converter and Controller

The GSC consists three level NPC system, with three legs. For one per phase of the NPC system is used two series connected IGBT and anti-parallel diodes. Three level half bridge power module using IGBT are implemented to proposed system. This power module has two topologies: a switched topology and a control topology. A switched topology uses the semiconductors using three level NPC system. A control topology uses controlled current sources using PI control system.

In the control topology, a GSC control system implemented as a PI regulator provides a current set point to an inner dq current controller as shown in Fig. 1. The current controller measures the DC voltage and calculates the error compared to the V_{dc} reference value. The current controller has separate PI regulators for direct and quadrature currents that produce a dq reference [10,11]. The AC phase voltages and currents are measured and fed to the current controller. A phase-locked loop generates the reference phase angle for the abc to dq transformations. A low pass filter is inserted into the feedback path from the $I_{a,b,c}$ measurement to represent the limited bandwidth of the current sensor. Modulation indices

are generated for each of the three separate modulators for the three phase legs.

C. Fuzzy logic-PI controlle

Conventional PI control method is widely implemented in wind turbine systems owing to its simple structure. The PI control method forces the system to achieve the optimum values by using the two gain parameters. Therefore, PI equations are expressed by Eq. (11):

$$u(k) = K_p e(k) + \frac{K_p T_s}{T_i} \sum_{i=0}^{k-1} e(k) \quad (11)$$

where, K_p and K_i are proportional gain, integral gain, respectively. The $e(k)$, T_s , and T_i is the error, the sampling period, the integral time constant, respectively. In addition to these, maximum overshoot of the system, steady-state error, and the time response features of rise time is fixed by conventional controller.

In general, conventional controller method has non-linear for parameter variations under load variation. When parameter variations come about in different operational conditions, the conventional control system can not resolve the error of the wind turbine system. Therefore, Fuzzy PI control is presented to improve system robustness in this study. Fuzzy PI control

is implemented both GSC and MSC for wind turbine based on PMSG. The general block diagram of fuzzy PI control method is given in Fig 2.

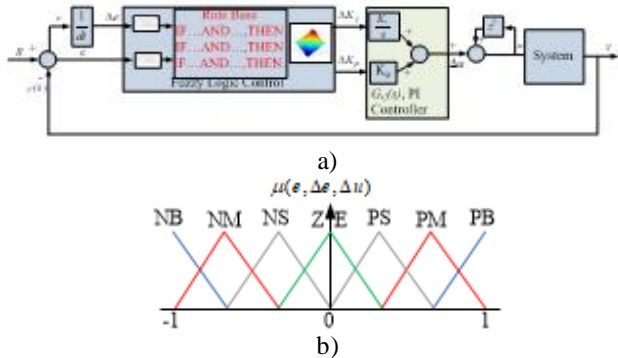


Fig.2. a) The general block diagram of fuzzy PI control method. b) MFs of e , Δe , and Δu

The fuzzy sets of FLCs are divided into seven sections for the input and output variables that consist of seven variables in the proposed study. These seven variables are named as Negative Big (NB), Negative Medium (NM), Negative Small (NS), Zero (Z), Positive Small (PS), Positive Medium (PM), and Positive Big (PB) [13].

The centroid defuzzification technique is given in Eq.(12).

$$y = \frac{\sum_{i=1}^m y_i + \mu_i(y_i)}{\sum_{i=1}^m \mu_i} \quad (12)$$

Where, y , m , y_i are the defuzzified output, the output quantificational index, and the output variable. $\mu_i(y_i)$ is the membership function.

Therefore, the rules of the FLC are obtained according to these principles, as given in Table 1. [13].

Table 1. Rule bases for e , Δe , Δu

$\Delta e / e$	NB	NM	NS	Z	PS	PM	PB
NB	PB	PB	PB	PS	Z	Z	Z
NM	PB	PB	PB	PS	Z	Z	NS
NS	PB	PB	PB	Z	Z	NS	NS
Z	PS	PS	PS	Z	NS	NS	NM
PS	Z	PS	Z	NS	NM	NM	NB
PM	Z	Z	NS	NM	NB	NB	NB
PB	Z	NS	NM	NB	NB	NB	NB

V. SIMULATION RESULTS

The simulation results of PMSG using three level NPC are presented in this section. The proposed model is designed to deliver power to a load. The presented simulations are realized for an 850-kW PMSG using three level NPC. The proposed model system is modelled and analysed in the Matlab/Simulink. The proposed model is proven to verify under different load conditions.

The proposed system is implemented varying load conditions. From time $t=0s$ to $t=2s$, from time $t=4s$ to $t=6s$, and from time $t=8s$ to $t=10s$, the load value is 0.5 pu operation. The time $t=2s$ to $t=4s$, the load value increases to 0.1 pu operation. From time $t=6s$ to $t=8s$, the load value increases to 0.75 pu operation conditions.

The rotor speed is given in Fig. 3. When load value changes between 1 pu, 0.75 p.u and 0.5 pu, rotor speed remains a constant 1 p.u value. The DC link voltage (V_{dc}) is illustrated in Fig. 4. When load value changes between 1 pu, 0.75 p.u and 0.5 pu, the DC link voltage remains a constant 500V.

The active power of PMSG and load are given in Fig. 6 and 7, respectively. When load value changes between 0.5 pu and 0.1 pu, the active power value of PMSG and load change between 0.5 p.u and 1 p.u, respectively. The active power value of PMSG changes same with varying load.

The stator current of PMSG (rms) is given in Fig. 8. When load value changes between 0.5 pu and 0.1 pu, the stator current of PMSG changes between 0.5 p.u and 1 p.u, respectively. The stator current value of PMSG changes same with varying load.

The stator voltage of PMSG (rms) and load voltage are given in Fig. 9 and 10, respectively. When load value changes between 1 pu, 0.75 p.u and 0.5 pu, the stator voltage of PMSG and load voltage remains a constant 1 p.u.

The load current is given in Fig. 11. When load value changes between 0.5 pu and 0.1 pu, the current of load changes between 0.5 p.u and 1 p.u, respectively.

The total harmonic distortion (THD) of the proposed system is given in Fig. 12. The THD is calculated using fast Fourier transform (FFT) analysis technique. The electrical grid voltage THD is approximately 1.49% for the NPC topology.

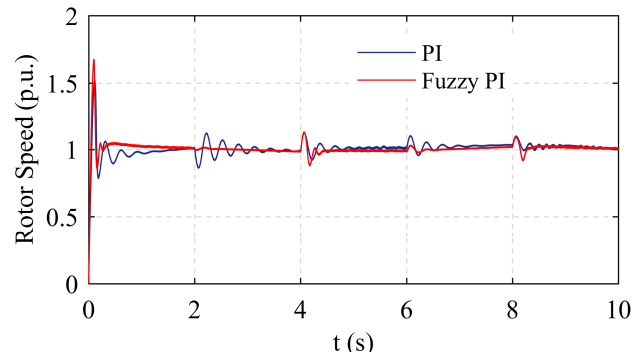


Fig.3. Rotor speed of PMSG (pu).

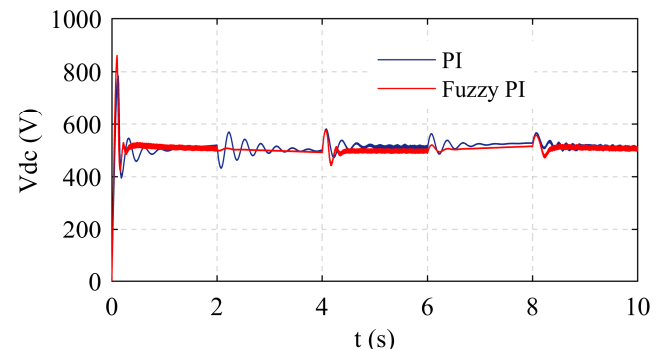


Fig.4. DC link voltage (pu)

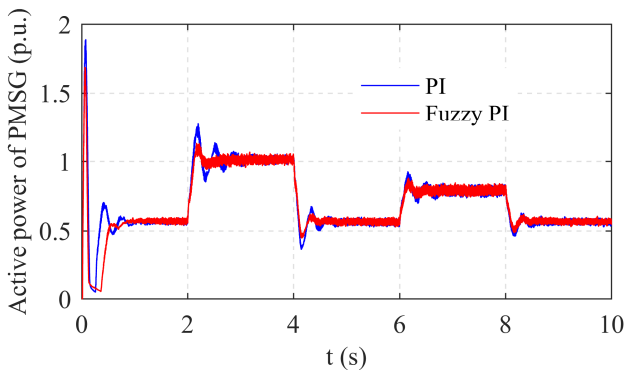


Fig.6. Active power of PMSG (pu)

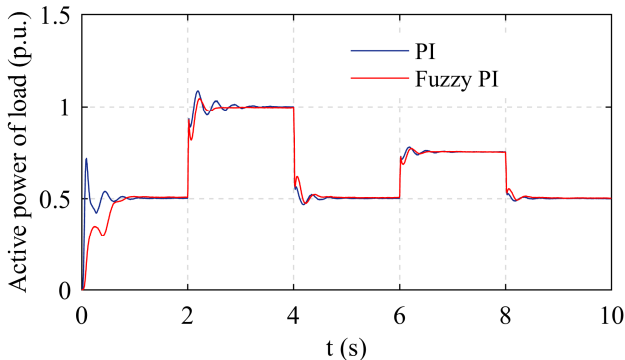


Fig.7. Active power of load (rms) (pu)

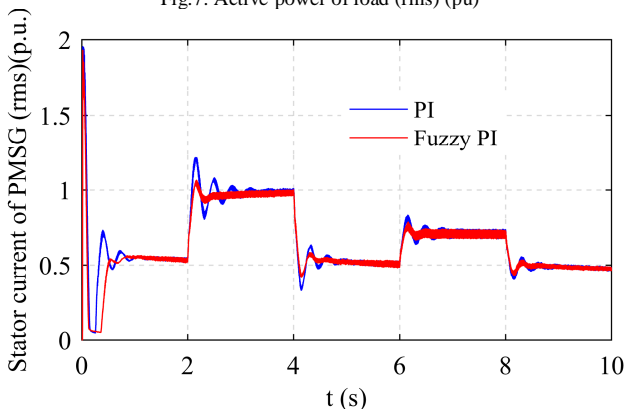


Fig.8. Stator current of PMSG (rms) (pu)

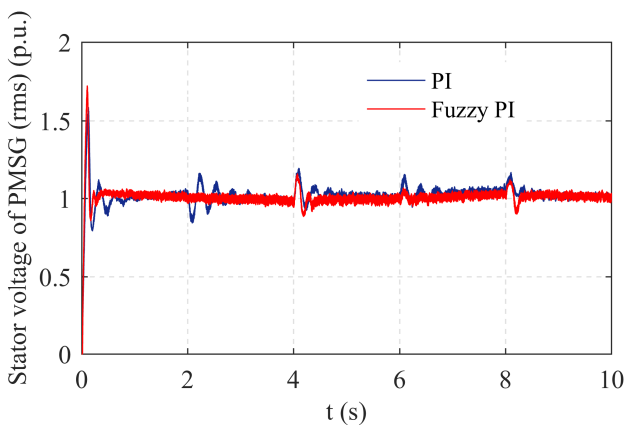


Fig.9. Stator voltage of PMSG (rms) (pu)

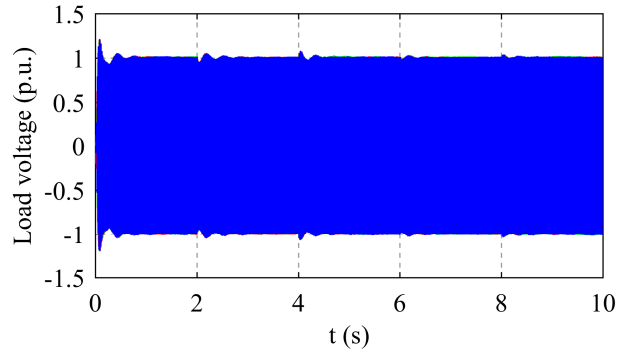


Fig.10. Load voltage (V)

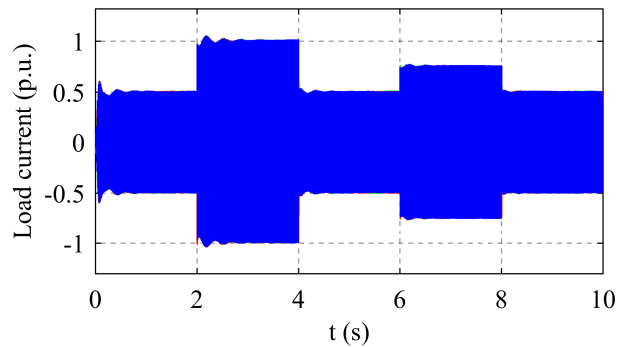


Fig.11. Load current (pu)

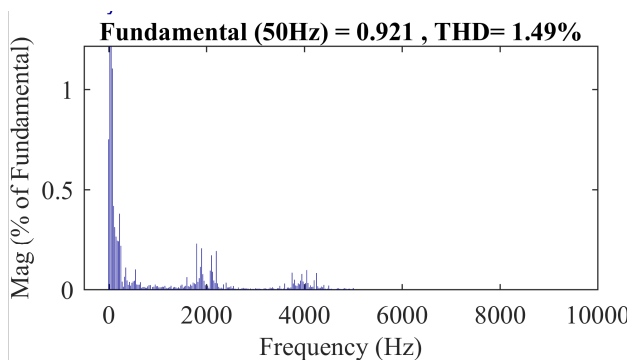


Fig.12. THD of injected voltage to grid.

VI. CONCLUSION

The permanent magnet synchronous generator has been gained attention by wind turbine manufactures due to advance of control system and power electronics. A grid side converter and machine side converter for PMSG based on three level NPC using fuzzy PI is proposed in the study. Neutral point control system of the DC link can be implemented more easily than two level systems. From the Matlab/Simulink results, it is observed that the voltage balance of the DC link is controlled fairly well under the variation speed of the PMSG. The performance of the PMSG system under the effects of varying load condition is detailed investigated in this study. The performances of the PMSG using GSC and MSC based on three level NPC using fuzzy PI are analysed. The electrical grid voltage THD is approximately calculated 1.45% for the NPC topology. It is verified by performed analysis that the proposed model can be operated stably under varying load conditions.

REFERENCES

- [1] C.-M. Hong, C.-H. Chen, C.S. Tu, "Maximum power point tracking-based control algorithm for PMSG wind generation system without mechanical sensors", *Energy Conversion and Management*, vol. 69, p.p.58–67, 2013.
- [2] E. Kabalci, "Design and analysis of a hybrid renewable energy plant with solar and wind power", *Energy Conversion and Management*, Volume 72, August 2013, Pages 51-59,
- [3] M. Alizadeh, S. S. Kojori "Augmenting effectiveness of control loops of a PMSG (permanent magnet synchronous generator) based wind energy conversion system by a virtually adaptive PI (proportional integral) controller", *Energy*, vol. 91, p.p. 610-629, 2015
- [4] A. M. Eltamaly, H. M. Farh "Maximum power extraction from wind energy system based on fuzzy logic control", *Electric Power Systems Research*, vol. 97, p.p. 144–150, 2013.
- [5] F. I. Bakhsh, D. K. Khatod "Application of variable frequency transformer (VFT) for grid interconnection of PMSG based wind energy generation system", *Sustainable Energy Technologies and Assessments*, vol. 8 p.p. 172–180, 2014.
- [6] A. Dahbi, M. Hachemi, N. N. Said, M.-S. N.-Said "Realization and control of a wind turbine connected to the grid by using PMSG", *Energy Conversion and Management*, vol. 84 p.p. 346–353, 2014.
- [7] A. Urtasun, P. Sanchis, I. S. Martín, J. Lopez, L. Marroyo "Modeling of small wind turbines based on PMSG with diode bridge for sensorless maximum power tracking", *Renewable Energy*, vol. 55, p.p. 138-149, 2013.
- [8] P. Liua, W. T. Yangb, C.E. Yanga, C. L. Hsu "Sensorless wind energy conversion system maximum power point tracking using Takagi–Sugeno fuzzy cerebellar model articulation control", *Applied Soft Computing*, vol. 29, p.p. 450–460, 2015.
- [9] A. Gencer, "Modelling and analysis of operation PMSG based WECS under different load conditions", 2016 8th International Conference on Electronics, Computers and Artificial Intelligence (ECAD), 2016.
- [10] A.G. Sanchez, M.G. Molina, A.M. Rizzato Ledo, "Dynamic model of wind energy conversion systems with PMSG-based variable-speed wind turbines for power system studies", *International Journal of Hydrogen Energy*, Volume 37, Issue 13, July 2012.
- [11] L. Wang, D.N. Truong, "Stability enhancement of a power system with a PMSG-based and a DFIG-based offshore wind farm using a SVC with an adaptive-network-based fuzzy inference system", *IEEE Transactions on Industrial Electronics*, vol. 60, p.p. 2799-2807, 2013.
- [12] E. Tremblay, A. Chandra, P.J. Lagacé, "Grid-Side Converter Control of DFIG Wind Turbines to Enhance Power Quality of Distribution Network" *Power Engineering Society General Meeting, IEEE*, Montreal, Que, 2006.
- [13] A. Gencer, "Modelling of operation PMSG based on fuzzy logic control under different load conditions," 2017 10th International Symposium on Advanced Topics in Electrical Engineering (ATEE), Bucharest, 2017, pp. 736-739.

BIOGRAPHIES



ALTAN GENCER was born in 1978. He received his BS. degree in Electrical Education at Technical Education Faculty of Firat University in 1999. He received the M.Sc. degree in Electrical Education from Firat University in 2002. He received Ph. D. degree in Electrical Education from Gazi University in 2011. From 2014, he is an assistant professor in Department of Electrical and Electronics Engineering, Faculty of Engineering and Architecture in the Nevsehir H.B.V. University in Turkey. His research interests include wind farm dynamic modeling, fuzzy logic control system.

Energy Efficient Routing Protocol to Extend Wireless Sensor Network Lifetime

T. Ercan, M. Asim

Abstract—In Wireless Sensor Networks (WSNs), the sensor nodes have limited energy resources with their mostly irreplaceable batteries. This makes to encourage design protocols that are energy efficient to provide a longer network lifetime. This paper proposes a method to divide the sensor network into equal-size grids namely regular geometric shaped clusters, selecting Cluster Head (CH) and Vice Cluster Head (VCH) for each grid by using Fuzzy Logic System (FLS). Since the CH being the central node and performing additional tasks in the cluster often results in early energy drain, the VCHs are introduced here as additional internal resources to replace CHs in the network. Unlike other typical hierarchical routing protocols, the CHs are not changed per each round; rather they are replaced on-demand in order to reduce energy consumption. We analyze and compare our proposal in the MATLAB with the well-known cluster-based protocol, LEACH and its modified version MODLEACH. The results show a significant improvement in network throughput, energy consumption and network lifetime.

Index Terms—Cluster head, fuzzy logic system, grid, vice cluster head, wireless sensor network.

I. INTRODUCTION

IN WSNs, most of the energy is consumed during communication processes. The sensor nodes sense and gather information from the environment and transmit them separately to the sink. The energy resources for sensor nodes are of finite capacities. Many energy efficient routing protocols have been presented to address this problem. Mainly they are divided into two categories; flat routing protocols and hierarchical routing protocols [1].

In flat routing protocols, all the nodes perform same tasks in the network and have similar functions. Data is usually flooded in the network and is transmitted in a multi-hop fashion to the sink. Flat routing protocols perform well in small-scale networks but they are not effective for large-scale networks because all sensor nodes generate high data processing and use more bandwidth [1]. Some famous examples of flat routing protocols are SPIN (Sensor Protocols for Information via Negotiation) [2], Directed Diffusion [3], Rumor Routing [4] and Gossiping [5].

T. ERCAN, is with Department of Computer Engineering, Yasar University, Izmir, Turkey, (e-mail: tuncay.ercan@yasar.edu.tr).

M. ASIM, is with Department of Computer Engineering, Yasar University, Izmir, Turkey, (e-mail: m_asimismail@yahoo.com).

Manuscript received May 06, 2018; accepted June 19, 2018.
DOI: [10.17694/bajece.421416](https://doi.org/10.17694/bajece.421416)

On the contrary, in hierarchical routing protocols, different nodes perform distinct tasks. They are arranged in groups or clusters and each cluster has a CH, whose task is to collect data from their member nodes and send them to the Base Station (BS). Generally, the node with highest energy level in a cluster is selected as the CH. Hierarchical protocols work in rounds, where a round usually includes; making of clusters, selecting CHs and delivering the collected data to the sink. This type of routing protocols are proved more energy efficient than flat based routing protocols [1] [6].

The functions of CHs in a hierarchical routing protocol are greater than a normal node. It includes; overhearing, receiving, data aggregation and transmission of packets to the sink. The tasks of CHs in cluster-based networks are not just limited to the respective clusters, they are also involved in routing of the data from their neighbor CHs. Particularly, the CHs located near the sink are most prone to energy exhaustion because of their role as an intermediate node for the other part of network that can't reach the sink directly. These tasks are energy consuming and they make the lifetime of a CH shorter as compared to the normal nodes [7] [8].

In this study, we propose an alternative VCH for CHs, when they suffer from energy dissipation. The current CH selects the next VCH. After this selection, VCH does not take part in any process until its energy level dissipates to a threshold level. Later, the VCH is notified from CH and replaces the CH's functions. It will select a new VCH for itself. Fuzzy Logic System is used to calculate the ranks of the nodes and according to ranks, CHs and VCHs are selected. Its decision making process is based on two parameters; residual energy and centrality. The highest-ranking node is selected as the CH and the second highest as VCH.

The remaining part of the article is organized as follows. Section II discusses the VCH and its usage with a literature review. The proposed mechanism with details is explained in section III. The simulation results are analyzed and discussed in section IV. Finally, section V concludes the paper.

II. VICE CLUSTER HEAD

The concept of VCH in the literature is presented to extend the network lifetime and handle the nodes in a cluster after the inability of the current CHs to perform. Mostly, the node having second highest residual energy in a cluster is selected as the VCH and it replaces CH's functions in case of its energy drain. The protocols that utilizes VCHs are proved more energy efficient with a better throughput.

LEACH [6] as a famous example of hierarchical routing protocol, has inspired many reformations in this area. It works in rounds, where a round includes; setup phase and steady state phase. In setup phase, some nodes are selected to become CHs based on the predefined conditions, then, the nearby nodes join them to form clusters. In steady state phase, the CHs collect and aggregate the data from their cluster members and send them to the BS. The CH selection process takes place in each round. However, [9] avoids this often CH selection per round in order to reduce energy consumption, by introducing a VCH in each cluster. The VCH takes over CH's place when it begins to consume too much energy. In this way the duration of steady state phase is increased and the extra energy that is consumed in setup phase is avoided, which results in networks lifetime extension.

Similarly, [10] presents VCHs in its clusters. The VCHs are selected by the CHs based on their energy levels. The VCH does not participate in any process until the energy level of CH decreases to a certain threshold value (such as, 10%). On getting the call, VCH starts working as the new CH and announces itself in the cluster.

Reference [11] uses VCH in LEACH-C [12] protocol to improve its performance. VCH is selected by the CH and replaces the CH when its energy level decreases to a minimum value. Likewise, [13] improves the performance of LEACH by introducing a VCH in the network and it takes over CH's function when the CH dies. Some other protocols like [14] and [15] follow the same method as well and utilize the VCHs after the death of CHs.

In the proposed method, VCH is the node having highest rank after CH in a cluster. The ranks are calculated by FLS based on two parameters; energy level and centrality. The VCH sleeps after its selection in order to avoid energy dissipation until it gets a wakeup call from the CH. The CH sends this call when it consumes $1/10^{\text{th}}$ of its initial energy. The VCH then starts functioning as the new CH.

III. PROPOSED MECHANISM

Our proposed mechanism runs two phases; setup phase and transmission phase. The setup phase includes; division of nodes into grids, selection of CHs and VCHs for each grid by using FLS. In the transmission phase, CHs collect sensed data from their cluster members, aggregate and transmit them to the BS. They are further explained in details as follows.

A. Making of Grids

The grids are established to divide the network into equal sized areas with a group of nodes. This method gives a fair distribution of the load across the network. The size of grids are defined according to the signal range of sensor nodes, as calculated in [16] and [17]. The CH of a grid should be able to reach all its member nodes and as well as to the neighbor CHs. The CHs in cluster-based routing protocols are used as intermediate nodes to re/route the packets from distant CHs that cannot reach the BS directly. Therefore, the CHs should be accessible from each other. Fig. 1 shows a network with

randomly deployed nodes, grouped into grids and each grid have a CH and a VCH. MATLAB is used to run and display the values in the figure according to the input values taken from Table1.

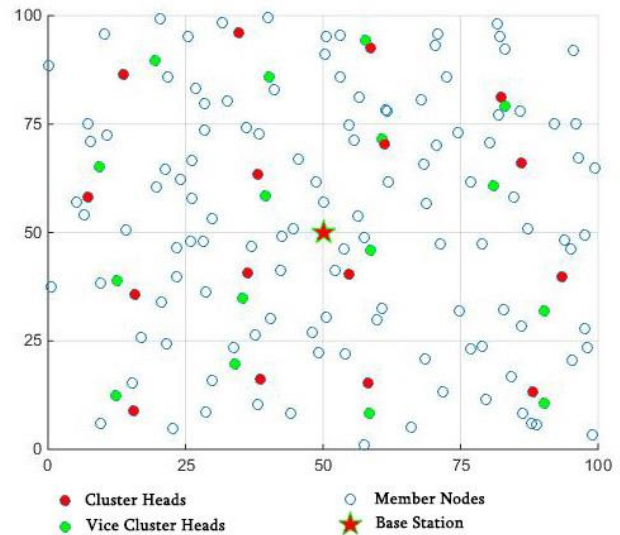


Fig.1. Grid formation

B. CH Selection

The selection of CH only takes place in the setup phase; later this process is avoided in order to reduce the energy consumption that is caused during the selection process. FLS is used to select the CHs, and its decisions are based on two parameters; residual energy and centrality.

1) Residual Energy

The existing energy level of a node to become CH is important to evaluate, because a CH has more energy consuming tasks to perform than a normal node. Ref [9] and [10] consider only energy level as the primary parameter for CH selection. However, we consider the centrality as well as the energy level to get results that are more appropriate. As stated in [18] and [8], the residual energy (RE) of a node can be calculated when the consumed energy (CE) is subtracted from the initial energy (IE) (see equation (1)).

$$RE = IE - CE \quad (1)$$

2) Centrality

Centrality is the sum of square distances of a node with respect to the other cluster members as stated in [19] [20]. The distances between the nodes are calculated by using the distance formula, from equation (2). The most central node in a cluster has minimum distance from other cluster members and it will cause them to consume less energy. Therefore, centrality is considered an important parameter for CH selection, so that the member nodes can communicate with CH conveniently.

$$D = \sqrt{(N_x - M_x)^2 + (N_y - M_y)^2} \quad (2)$$

3) Fuzzy Logic System

In our study, FLS is used to arrange the sensor nodes into ranks because of its spontaneity and energy efficiency [18] [8]. FLS works with linguistic variables and divides the input values into different levels according to their ranges such as, in this study, the both inputs i.e. residual energy and centrality are divided into three levels; *Low, Medium and High*, ranging from 0 to 0.5 J (Fig. 2) and the centrality is divided into three levels; *Close, Medium and Far*, ranges between 0 and 400 m (Fig. 3) respectively. From these input variables, the nodes are categorized into five different levels, as the fuzzy output such as; *Low, Low Medium, Medium, High Medium and High*, ranging between 0 and 1 (Fig.4).

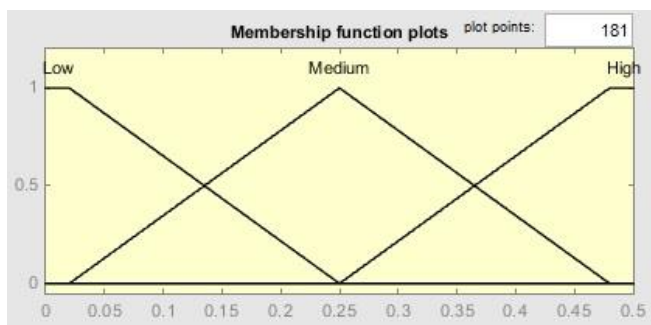


Fig.2. Membership functions for residual energy

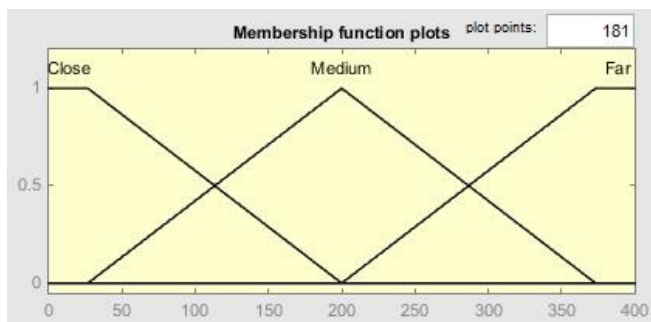


Fig.3. Membership functions for centrality

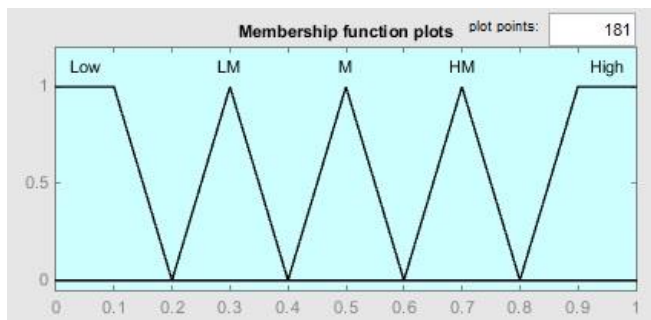


Fig.4. Membership functions for rank

C. VCH Selection

The node with the highest rank in a cluster is selected as the CH. After selection, the CH announces itself in the cluster by broadcasting a message. The member nodes send ACK messages along with their ranks. The CH chooses the node with the highest rank as the VCH and declares it. VCH after its selection does not participate in any task; it simply waits for a notification call from the CH if its energy level decreases to a threshold level (the threshold energy is taken as the 1/10th of initial energy). When getting the call, the VCH replaces CH's functions and announces itself in the cluster as the new CH. The member nodes send the ACK message with their ranks again, as they did before. The new CH selects the highest-ranking node as the new VCH in the same way it was selected.

By employing the method the setup phase is not run repeatedly, rather the CHs are changed on-demand. This gives a great energy boost to the network, as demonstrated from the simulation results. The entire working mechanism of the proposed method is explained in Fig. 5.

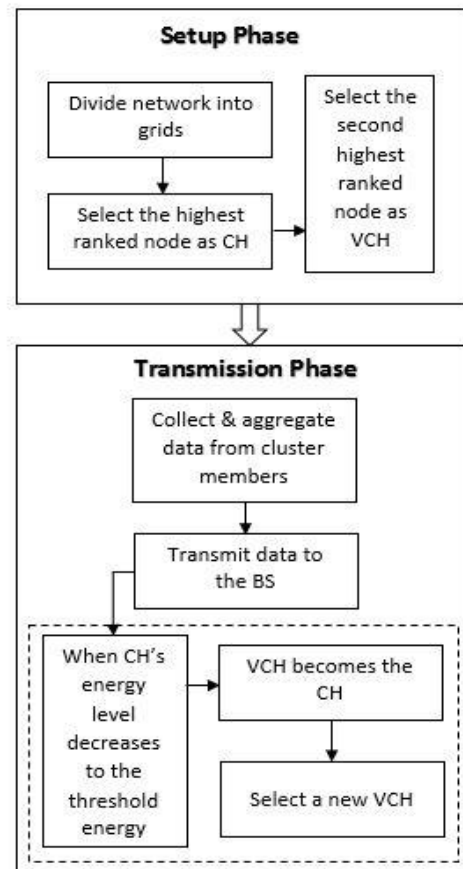


Fig.5. Model of the proposed method

IV. SIMULATION RESULTS AND DISCUSSION

The simulations are performed in MATLAB and the results are compared with LEACH and MODLEACH [21] as far as we could find the related performance values in the literature. MODLEACH is a modified version of LEACH. Unlike LEACH, it does not change the CHs in each round unless their

energy level decreases below a certain threshold value. It gives a better performance compare to the LEACH. The authors in [22] proposed using a VCH enabled in the cluster with two purposes; guard the CH against failure for energy drain and reduce the clustering frequency. Its function is different from our method, however, the authors compared with their results with LEACH again. Reference [23] also proposed to use a second cluster head. However, the authors named the cluster heads as master and vice cluster heads and claimed they could work together on data collection, fusion and transition. They also proved a longer network lifetime for large-scale sensor networks. We believe that our method outperforms both LEACH and MODLEACH, by consuming less energy, delivering higher data rate and extending network lifetime in a VCH proposed scenario.

The experiments are performed in an area of 100 by 100 m, where the BS is placed at the center of the network along with 100 sensor nodes. The simulation parameters are listed in the Table I.

TABLE I
SIMULATION PARAMETERS

Parameter	Value
Field size	100m x 100m
Number of sensor nodes	100
BS location	50m x 50m
Initial energy (E ₀)	0.5 J
Transmission Energy (E _{TX})	50 nJ/bit
Receiving energy (E _{RX})	50 nJ/bit
Packet Length	4000 bits
Free space amplifier (E _{fs})	10 pJ/bit/m ²
Multipath amplifier (E _{mp})	0.0013 pJ/bit/m ²
Data aggregation (EDA)	5 nJ/bit

The longer a node takes to die, the higher will be its lifetime. From the Fig. 6 it can be seen that the first node dies at 1563 rounds and the last node dies after 4340 rounds, which is about 64.4% and 51.8% higher than MODLEACH and LEACH respectively.

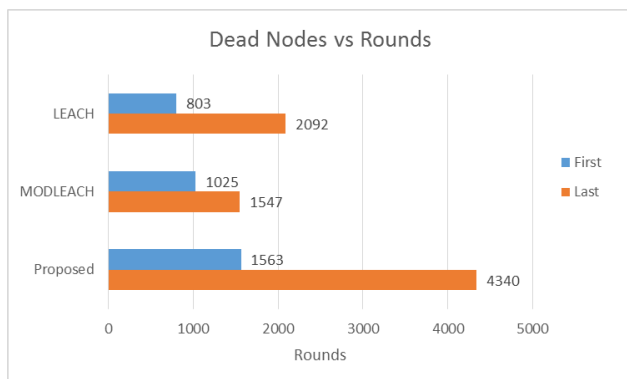


Fig.6. Network lifetime

The proposed approach is able to perform for a longer time because of its lower energy consumption per round. It consumes about 12.8%, 24.4%, 38.5% and 51.3% energy at rounds 325, 650, 975 and 1300 respectively (from Fig. 7). However, MODLEACH consumes 26.5%, 53%, 79.6% and 98.8% while for LEACH it is 27.3%, 54.7%, 81.2% and 99.2% respectively. From the listed numbers, it can be observed that the other two protocols likely consume twice as much energy as ours.

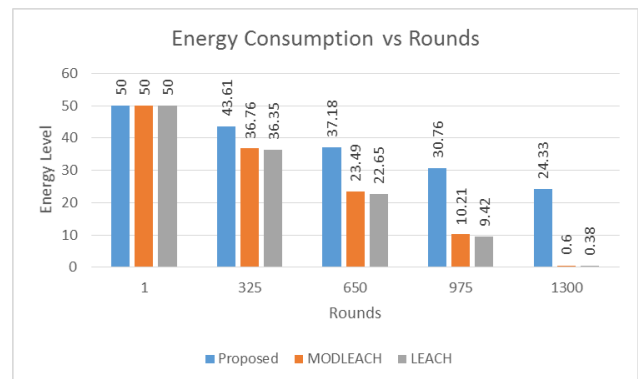


Fig.7. Energy consumption

The throughput of a network depends on number of packet delivered to the destination. Fig. 8 shows packet delivery ratio to the sink according to the rounds. MODLEACH and LEACH have higher delivery in the first 1000 rounds, but this number decreases with the increase of number of rounds. Their number of packet does not change after 3000 rounds, that shows there is no more alive nodes left in the network. However, in our protocol it raises at rate of 29.5%, 59%, 87.8%, 99.9% and finally 100% with respect to the total number of delivered packets until 5000 rounds with a difference of 1000 rounds.

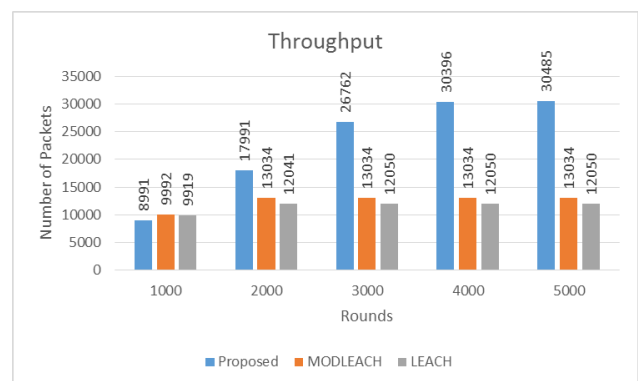


Fig.8. Throughput

V. CONCLUSION

In this study, we proposed a method to improve the performance of wireless sensor networks by using the network resources. The nodes are divided into grids and a CH and a VCH is selected for each grid by using the fuzzy logic system.

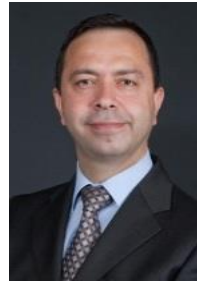
The VCH does not participate in any process after its selection until the energy level of the CH decreases to a threshold level. The VCH then becomes the CH and selects a new VCH for itself as its backup. By continuing this order, there will always be a CH in the cluster to manage its member nodes.

The process of selecting CHs can be improved in the future by adding more parameters to FLS, such as, number of neighbor nodes, density of network and speed of the nodes in case of a mobile network. It will result in selecting the optimal nodes as the CHs, and ultimately causing less energy to consume for communications tasks.

REFERENCES

- [1] X. Liu, "A Survey on Clustering Routing Protocols in Wireless Sensor Networks", *Sensors*, Vol.12, 2012, pp.11113-11153.
- [2] J. Kulik, W. Heinzelman, H. Balakrishnan, "Negotiation-Based Protocols for Disseminating Information in Wireless Sensor Networks", *Wireless Networks*, Vol.8, 2002, pp.169-185.
- [3] C. Intanagonwiwat, R. Govindan, D. Estrin, J. Heidemann, F. Silva, "Directed Diffusion for Wireless Sensor Networking", *IEEE/ACM Transactions on Networking*, Vol.11, No.1, 2003.
- [4] D. Braginsky, D. Estrin, "Rumor Routing Algorithm For Sensor Networks", *Proceedings of the 1st ACM international workshop on Wireless sensor networks and applications*, 2002, pp.22-31.
- [5] Z. Haas, J. Halpern, L. Li, "Gossip-Based Ad Hoc Routing", *IEEE/ACM Transactions on Networking*, Vol.14, N0.3, 2006.
- [6] W. Heinzelman, A. Chandrakasan, H. Balakrishnan, "Energy-Efficient Communication Protocol for Wireless Microsensor Networks", *Proceedings of the Hawaii International Conference on System Sciences*, 2000, pp.1-10.
- [7] I. Gupta, D. Riordan, S. Sampalli, "Cluster-head Election using Fuzzy Logic for Wireless Sensor Networks", *3rd Annual Communication Networks and Services Research Conference (CNSR'05)*, 2005, pp. 255-260.
- [8] T. Preethiya, G. Santhi, "Enhancement of Lifetime Using Fuzzy- Based Clustering Approach in WSN", *2014 International Conference on Electronics and Communication Systems (ICECS)*, 2014, pp. 1-5.
- [9] F. Zhao, Y. Xu, R. Li, "Improved LEACH Routing Communication Protocol for a Wireless Sensor Network", *International Journal of Distributed Sensor Networks*, Vol.2012, 2012.
- [10] A. Mehmood, J. Lloret, M. Noman, H. Song, "Improvement of the Wireless Sensor Network Lifetime using LEACH with Vice-Cluster Head", *Ad-Hoc and Sensor Wireless Networks*, Vol.28, No.1-2, 2015, pp.1-17.
- [11] T. Hassan, G. Selim, S. Sadek, "A Novel Energy Efficient Vice Cluster Head Routing Protocol in Wireless Sensor Networks", *2015 IEEE 7th International Conference on Intelligent Computing and Information Systems, ICICIS*, 2015, pp.313-320.
- [12] W. Heinzelman, A. Chandrakasan, H. Balakrishnan, "An Application-Specific Protocol Architecture for Wireless Microsensor Networks", *IEEE Transactions on Wireless Communications*, Vol.1, No.4, 2002.
- [13] A. Ahlawat, V. Malik, "An Extend Vice-Cluster Selection Approach To Improve VLEACH Protocol in WSN", *International Conference on Advanced Computing and Communication Technologies, ACCT*, 2013, pp.236-240.
- [14] M. Yassein, A. Al-zou'bi, Y. Khamayseh, W. Mardini, "Improvement on LEACH Protocol of Wireless Sensor Network (VLEACH)", *International Journal of Digital Content: Technology and its Applications*, Vol.3, No.2, 2009.
- [15] A. Singh, S. Rathkanthiwar, S. Kakde, "Energy Efficient Routing of WSN using Particle Swarm Optimization and V-Leach Protocol", *International Conference on Communication and Signal Processing, ICCSP*, 2016.
- [16] Q. Gao, K. Blow, D. Holding, I. Marshall, X. Peng, "Routing Analysis and Energy Efficiency in Wireless Sensor Networks", *IEEE 6th CAS Symp. on Emerging Technologies: Mobile and Wireless Comm.*, 2004.
- [17] R. Akl, U. Sawant, "Grid-based Coordinated Routing in Wireless Sensor Networks", 2007.
- [18] W. Din, S. Yahya, M. Taib, A. Yassin, "Energy Efficient of WSN using Two Parameters Selection", *2013 IEEE Conference on Systems, Process and Control, ICSPC*, 2013, pp. 181-185.
- [19] N. Nokhanji, Z. Hanapi, S. Subramaniam, M. Mohamed, "An Energy Aware Distributed Clustering Algorithm Using Fuzzy Logic for Wireless Sensor Networks with Non-uniform Node Distribution", *Wireless Personal Communications*, Vol.84, No. 1, 2015, pp. 395-419.
- [20] M. Jahanshahi, S. Rahmani, S. Ghaderi, "An Efficient Cluster Head Selection Algorithm for Wireless Sensor Networks Using Fuzzy Inference Systems", *International Journal of Smart Electrical Engineering*, Vol.2, No.2, 2013, pp.121-125.
- [21] D. Mahmood, N. Javaid, S. Mahmood, S. Qureshi, A. Memon, T. Zaman, "MODLEACH: A Variant of LEACH for WSNs", *2013 8th International Conference on Broadband, Wireless Computing, Communication and Applications, BWCCA*, 2013, pp.158-163.
- [22] R. Pachlor, D. Shrimankar, "VCH-ECCR: A Centralized Routing Protocol for Wireless Sensor Networks", *Hindawi Journal of Sensors*, Volume 2017, Article ID 8946576, pp.1-10.
- [23] Ma et al. "Hybrid energy-efficient APTEEN protocol based on ant colony algorithm in wireless sensor network", *EURASIP Journal on Wireless Communications and Networking*, (2018) 2018:102, pp.1-13.

BIOGRAPHIES



TUNCAY ERCAN graduated from Military Academy, Department of Electric-Electronics in 1986. He received his M.S. degree from Ege University, and Ph.D from Dokuz Eylul University in Computer Engineering in 2000 and 2005 respectively.

Currently he is an Assistant Professor at Yasar University, Department of Computer Engineering. His research interests include: Advanced Network Technologies, Wireless Ad-hoc and Sensor Networks, Network Security and Forensics, Network modelling.



MUHAMMAD ASIM graduated from Balochistan University of Information Technology, Engineering and Management Sciences, Quetta, Pakistan, department of Electronic Engineering in 2013. Currently he is doing his Master's from Yasar University, Izmir, Turkey, Department of Computer Engineering. His research interests include: Wireless Sensor Networks, Optimization of congestion control algorithms and energy efficient routing protocols for sensor networks.

PV Array Based Smart Home Automation System

A. Şenpınar

Abstract--The utilization of renewable energy sources have been increasing day by day. Solar, wind, biomass, wave, etc. are some of the renewable energy sources. Solar, wind and hydro are more commonly used than others. Solar energy has many advantages such as abundance, renewability, continuation, and pollution free etc. Advancing technology increases people's life standards. Over time, high life standards have stopped being a luxury and entered people's homes with smart home automation systems. With the advances in Internet technologies, people now expect to be able to control their homes and workplaces over the Internet too. This study controls six different Computer/Internet-based systems of smart home automation in a house which is included solar arrays. These systems were illumination of three different rooms, temperature control of a room, garden irrigation system control, and home security system control. With the software written, all these systems were monitored online on a website. These controls were successfully experimented on the model house with the smart home automation system designed.

Index term-- Internet access, pv arrays, renewable energy, smart home automation.

I. INTRODUCTION

HUMAN needs are changing increasingly by the day along with the advancing technology. Millions of engineers and scientists around the world are working towards achieving these advances. Recent human needs entail the facilitation of home and work life. Many previously manual operations can now be performed automatically with the automation systems developed with the help of advancing technology. Such efforts are known by the name "Smart Home Automation Systems". The main goal of this concept is to enable a safer, easier, more comfortable and economic life. The energy consumption has been also increasing since these systems are increasing. So, it is utilized from renewable energy sources to meet the energy.

Commonly used methods in smart home automation systems include phone control, internet based control, Plc control and computer control.

Even though smart buildings were defined for the first time at the beginning of the 1980s in the USA, it only reached Turkey in 1984. At first, applications in the country were based on observation. Many applications around this time and thereafter targeted the comfort of healthy and ordinary people. Yumurtaci et al. studied smart home systems and the technologies usually used in these systems [1].

A. SENPINAR, is Department of Electronics Technology, College of Technical Sciences, Firat University, Elazig, Turkey, (e-mail: asenpinar@gmail.com).

Manuscript received May 03, 2018; accepted June 30, 2018.

DOI: [10.17694/bajece.420722](https://doi.org/10.17694/bajece.420722)

Yet another study designed a smart home automation system over GSM technology. This technology works over a phone line by processing digitized tones, and has the advantage of being used independently of time and place.

Isik et al. used a different method to design another mobile phone based smart home automation system [2]. Bekcibasi and Tenruh studied control over telephone and concluded that it may be preferred owing to its ease and reasonable maintenance costs [3]. There are many other studies on GSM technology [4-8]. For Internet control, the design is made with a server card embedded into the web interface and accessing the system over the Internet [9-12]. Other researchers studied computer controlled smart home automation systems. In this method, control is achieved via the interface program on a desktop or laptop computer by accessing micro-controlled circuits over ports [13-14]. Smart home systems designed for Plc control operate by accessing the Plc over a written Scada [15]. There are also other studies on smart home automation systems, most of which used micro controller design [16-17]. Other researchers have investigated the general structure of smart home automation systems [18-30]. Hazer et al. studied the control parameters and benefits of smart home automation [31]. Some researchers have investigated the renewable energy and energy systems of smart home automation systems [32, 33].

Smart home automation systems may be used to control electronic tools and systems such as security [34, 35], temperature [36, 37], RF command [38, 39], illumination [40], TV, sound systems, irrigation systems, curtain control, and garden/garage gate control. These systems may particularly benefit disabled and old people's lives.

When people are away from their homes, they wish to control what is happening over smart home automation systems. For instance, having left for their summer vacation, a family may want to check their home security system or irrigation for the garden from afar. Similarly, a family may want to check the temperature at home on the internet and adjust it before they arrive home after an evening out. This study aims to enable the control of different home electronic systems by means of renewable energy sources away from home. The energy which is required for this purpose is provided by pv array. These systems controlled via a computer were the illumination of three rooms, temperature control of a room, home security system control, and the control of garden irrigation system.

II. SYSTEM DESIGN

The designed smart home automation system was accessed over the internet. The system basically works over a computer program. System information is entered on a database through a website. This database is kept on a rental server.

The computer program reads and transmits data regularly from the database to the control circuit. There are six active outputs from the computer in the system. These outputs are used to illuminate three rooms, start and stop air conditioning for temperature in a room, start and stop the garden irrigation system, activate and stop the home security system. Optionally, the number of outputs can be increased; any device on a power line, for instance an iron, tv, or electric oven may be controlled. The designed system has 8 outputs and six of them are ready for active use. Further, the system may also be used to control the temperature of three rooms. Another feature on the system is that it allows the eight input unit to be checked over a website. The system is not affected by power outages because it is supported by pv arrays. Fig.1 shows the block diagram of the designed system. Fig.2 shows the model house where the designed smart home automation system could be established. The designed system has five main components: pv array, internet access, computer software program, control circuit and driver circuit.

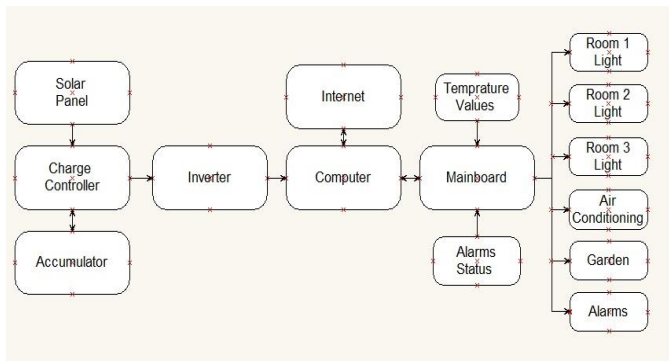


Fig.1. Block diagram of the designed system



Fig.2. Model house

A. Pv Array

A PV cell is a specialized semiconductor material with a p-n junction. It converts sunlight into electricity through a basic process called photovoltaic effect. The energy generated by the cell is in direct proportion with the visible light it has been exposed to. Additionally, conversion efficiency also depends on extending the plane. The amount of the current and the voltage changes depending on the amount of sunlight shining on the cell. Then, the I-V equation is:

$$I = I_1 - I_0 (e^{(qV)/(kT)} - 1) \quad (1)$$

where I_1 is the component of the pv cell current due to photons, electrical load ($q = 1,6 \cdot 10^{-19} \text{C}$), $k = 1,38 \cdot 10^{-23} \text{ J/K}$ (Boltzman constant) and T is the cell temperature in Kelvin.

B. Internet Access

Internet access enables remote access to the system. It allows people to control their smart home automation system by using a predefined website. As the website supports mobile devices, the system may also be accessed over smart phones. Website design has two components. The first one entails the inclusion or exclusion of the electronic devices or systems to be controlled. The buttons here are used to switch on/switch off. The first component shows the current temperature in a pre-specified room on the screen. Based on this temperature, the user can control the air conditioning system for heating in winter or cooling in sun. Buttons in the second line in Fig.3 are used to switch on/switch off for garden (irrigation), air conditioning (rooms) and home security. The second component includes the activation/deactivation of the home security system. When an alarm goes off while the security system is in use, this component notifies us and provides see on the screen from website. Buttons in the last line in Fig.3 show the alarm statuses. For example; when the alarm conditions are active, it turns red from green. Fig.3 shows the web page.

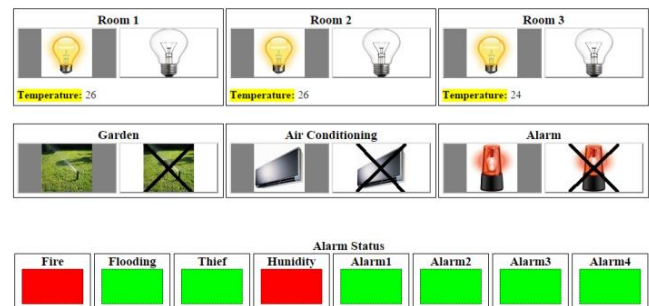


Fig.3. Web page

C. Computer Software Program

The computer software program is a desktop application using the RS-232 series communication that controls the designed system. Fig.4 shows the flow chart of it. This application provides the connection between the internet site and the control circuit. Owing to this program, the devices on the smart home automation system may be controlled over the home computer when there is no internet. Below is a screenshot from when the application runs for the first time (Fig.5).

This application has two sections. The first one includes the settings for the connection between the application and the control circuit. The COM port to connect to and the speed for the connection are selected here. When the COM port is clicked, currently usable ports are displayed. If the port that our device has been connected to is not shown among the ports, the connection between the port and the electronic circuit needs to be checked. The second section is where the devices on the system can be checked. It has been designed to check 6 devices and includes 12 buttons for the switch on/switch off operations. The left side of the dual buttons is used for energizing, and the right side for de-energizing. All buttons have active and passive positions.

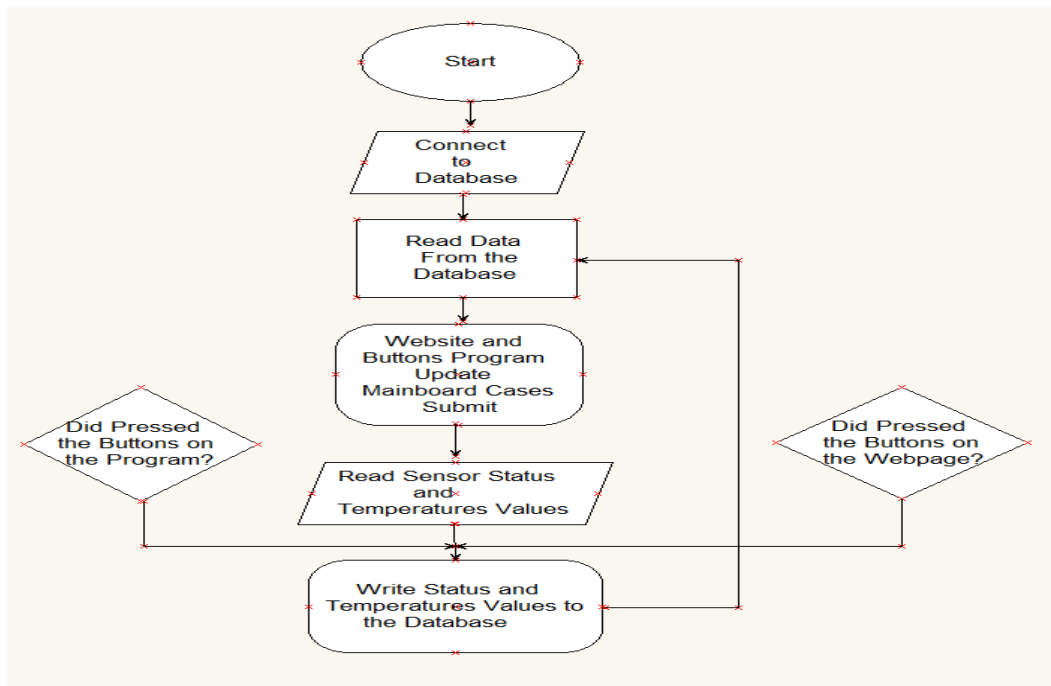


Fig.4. The flow chart of desktop application

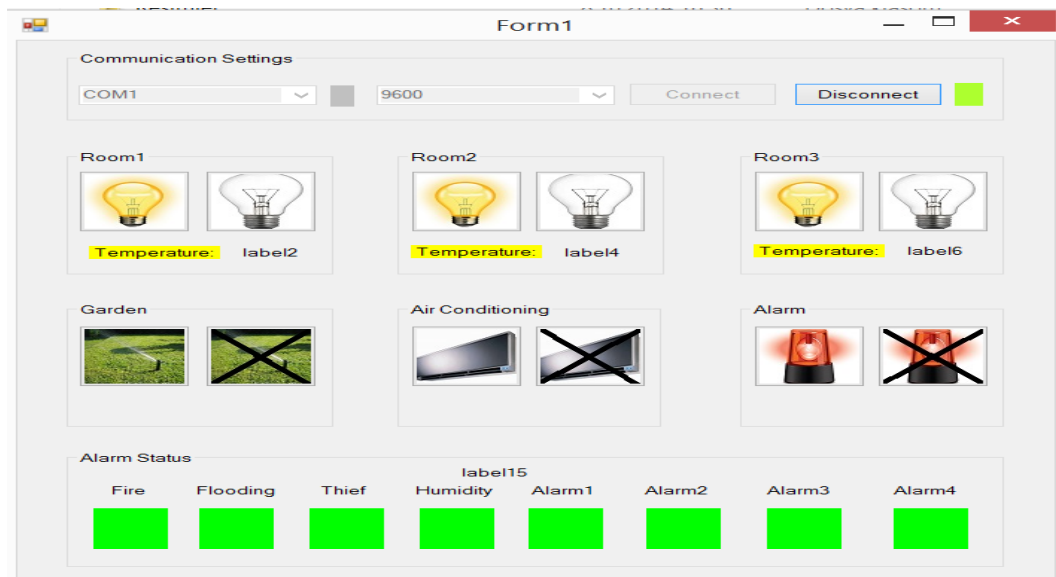


Fig.5. Screenshot of the desktop application

These positions provide information about whether that device is working online or not. This enables us to view the device that we wish to control and change its position accordingly. In addition, the temperature values of the rooms can also see in this section if want.

D. Control Circuit

The control circuit is the unit that enables communication between the computer and the devices to be controlled. This circuit is connected to the computer output and controls the driver circuit according to the commands received. At the same time, it sends the information from the security system and the value from the temperature sensor to the computer.

The microprocessor used was Microchip's 16F877A from the PIC family. This microprocessor has enough input/output ports for the controls. It also enables the RS-232 series communication protocol that the system requires to communicate with the computer.

The system has 6 active outputs and has been designed to control up to 8 outputs with the same design. All controls made over the computer application can be viewed simultaneously on the website designed. In other words, the designed pv array based smart home automation system may be controlled both from a distance over the website and from home computer. The control circuit diagram and card are shown in Fig.6.

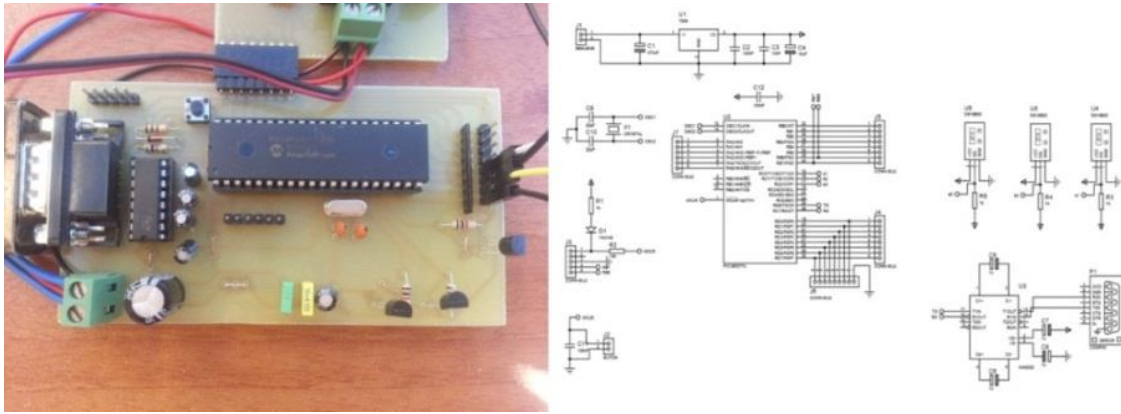


Fig.6. Control circuit diagram and card

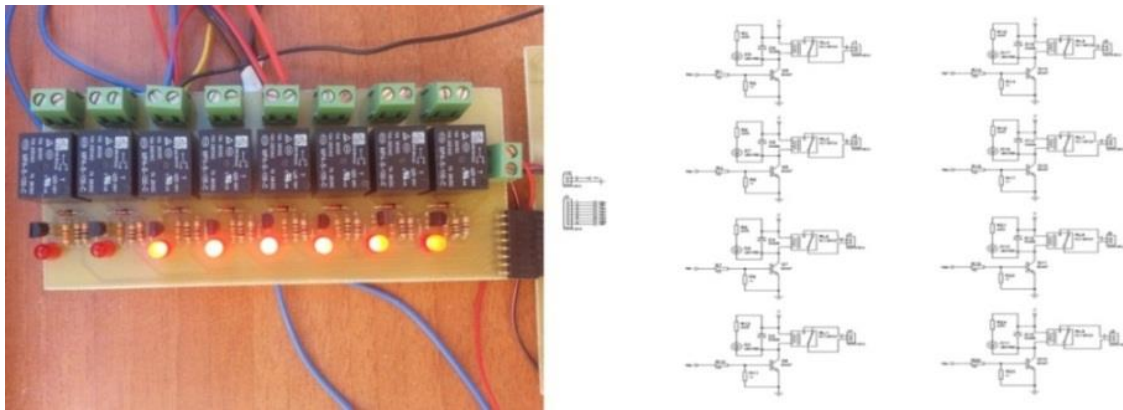


Fig.7. Driver circuit diagram and card

E. Electronics Driver Circuit

The electronics driver circuit is used to switch on and off the loaded devices depending on logic-1 (+5V) and logic-0 (GND) from the control circuit. It has a relay and a transistor. The transistor provides the energy needed for the relay by elevating according to the logic information received. With the led connected to the circuit, it may be understood whether the driver is active or passive. This circuit was designed as a model to control only one output. The system has 6 active outputs and so six leds in Fig.7 are active. It can be increased to control up to 8 outputs with the same design if needs.

For every other output, the circuits can be multiplied. Below is a diagram and complete state of a driver circuit for controlling a device (Fig.7).

F. The Input Units of System

The input units of the system are those that transmit any alarm incidents to the control card when the alarm output is active. The designed circuit supports eight alarm incidents. During the experiments, 4 active alarm inputs were used. These were as follows:

2.1. Humidity Sensor

The sensor used in the system measures humidity and yields an appropriate analog output. The output signal is between 0-5V. This sensor is used with a comparator circuit. With the help of a potentiometer on the circuit, the desired humidity level is set. If the humidity level increases this pre-specified

level, the circuit yields logic-1 information. Afterwards read with a microprocessor, this information is shown in the computer software and the Internet site.

2.2. Fire Sensor

The fire sensor in the system is one that yields analog output by perceiving ultraviolet (UV) light. It is used with a comparator circuit. With the help of a potentiometer on the circuit, the desired fire level is set. If the fire level in the environment increases this at any given time, we are informed over the computer and the website via the microprocessor.

2.3. Motion (PIR) Sensor

Known as the PIR sensor, this motion sensor yields 3V digital output based on the motion level. For as long as motion exists and depending on the time set, this 3V output continues. When there is no motion, the output is 0V. As the microprocessor does not perceive 3V as logic, an additional logic inverter has been used in the circuit between output and the microprocessor.

2.4. Flooding Sensor

The sensor functions on dry contact logic. It has two ends. One is connected to the feeding voltage. The other is connected to the microprocessor. If the water level rises, the sensor closes its contacts and thus logic-1 is fed into the microprocessor.

III. EXPERIMENTAL APPLICATION

The designed smart home automation system may be controlled over a website or the computer depending on the user's preference. A laptop was used to put this system into use. First, pv array and charge regulator are connected to

system. Then, the energy needed for the system is met by them. To begin with, the desktop application was downloaded on the laptop. Following this, connection was established between the control and driver circuits and the computer. Finally, the loads we planned to control were connected to the driver circuit and the system was ready to be used. The overview of the experimental system can be seen in Fig.8.



Fig.8. Overview of the experimental system

In order to run the smart home automation system, the desktop application was operated to observe the temperature data and alarm status from the control circuit. Then, a personal website was reached from the computer to observe the change in the alarm status connected to the security

system in the circuit. The alarm indicator that is normally is green turns red if the alarm is activated. The changes in room temperature at different times can be observed from the internet page (Fig.9).

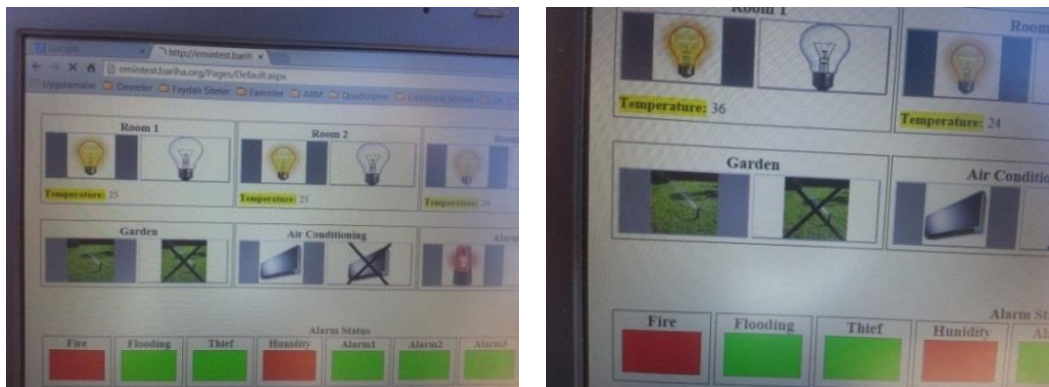


Fig. 9 Changes in temperature

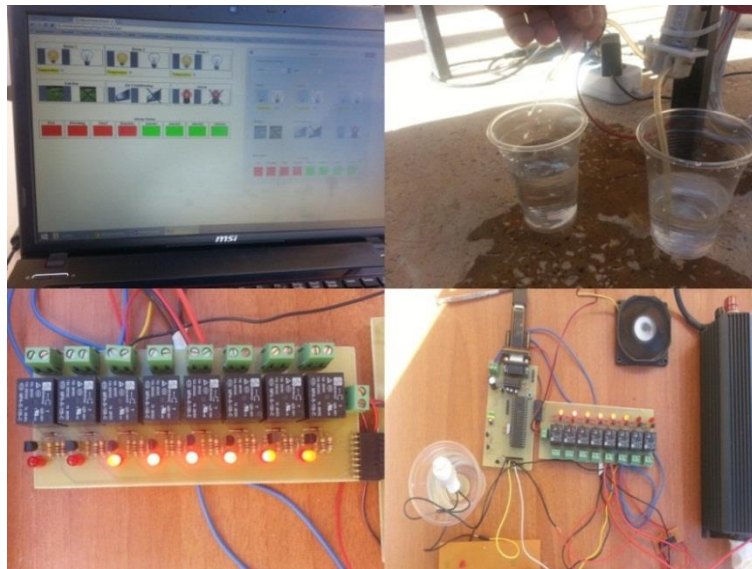


Fig.10. Observation of led and loads with all active output

When all outputs are active, the 6 led lights on the driver card give off light. The small computer fan representing the air-conditioning system keeps working, and the water pump representing the irrigation system moves the water in the glass (Fig.10).

When a load at an output is active, the led connected to that output is on (Fig.11). This shows whether an output is active or passive. When will outputs are active as above, all of the 6 different controls on the smart home automation system may

be made: illumination of 3 rooms, temperature (air-conditioning) control in one room, garden irrigation system control, and home security system control.

As input to the system, four active inputs were tried. The changes in the website and desktop application were observed online by boiling water in a kettle and applying vapor on the humidity sensor, by bringing a lighter close to the fire sensor, by moving a hand in front of the motion sensor, and by pouring water into a glass with the flood sensor in it (Fig.11).

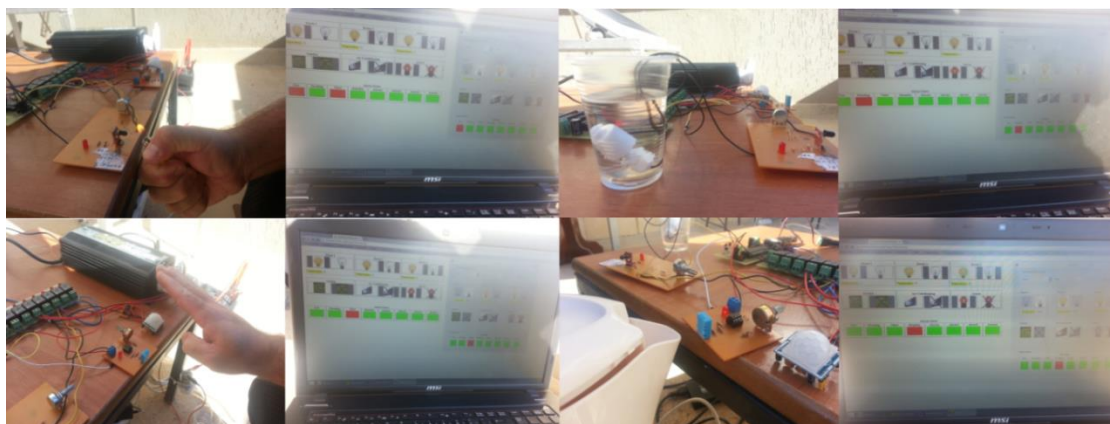


Fig.11. Observation of input units



Fig.12. Observation of temperature changing

In addition, the temperature change that occurred when one of the room temperature sensors was heated with a lighter was observed instantly on the website and the desktop application (Fig.12).

The designed smart home automation system has been also supported by renewable energy sources, such as pv array. That is why the energy consumption needed for the control and driver cards in the system is approximately 5-10W. The energy consumption of a laptop computer controlling these is approximately between 60-70W. The modem for the internet connection also consumes an average of 5W, thus necessitating a total of approximately 80-100W energy consumption. As can be seen, the energy required for the system may be provided by a 100W solar panel. In this experiment, the pv array for 80 W was been used.

IV. CONCLUSION

The use of solar energy in building is one important contribution for the reduction of fossil fuel consumption and harmful emissions to the environment. Solar energy used for industrial processes is an inevitable trend in future. Solar energy is clean and safe in many industrial sectors. This study focused on using the internet to control the illumination system, temperature system, irrigation system, and security system for pv array based smart home. It is an advantage of the designed smart home automation system that it may be controlled both over a website and with a computer. The reasonable costs of the automation system and its ease of application are the other advantages. This system facilitates human life. The designed smart home automation system can be applied to a small model house in future works.

Future studies may regularly record home controls and temperature information in graphics. This would enable an observation of how long a device works daily and how much energy they consume on average. The system may also be made more useful by add on such as mobile device software and RF command.

REFERENCES

- [1] M.Yumurtacı ve A.Keçebaş, "Akıllı Ev Teknolojileri ve Otomasyonu Sistemleri", 5. (IATS'09), 13-15, Karabük, Türkiye, Mayıs 2009.
- [2] Işık, Hakan, ve A. Alpaslan Altun, "Mikrodenetleyici Kullanılarak Cep Telefonu Kontrollü Akıllı Ev Uygulaması."
- [3] U.Bekçibaşı ve M.Tenruh, "Telefon Şebekesi Üzerinden Şifre Güvenlikli Akıllı Ev Kontrol Sistemi", 13.(Akademik Bilişim'11), 2-4, Malatya, Şubat, 2011.
- [4] K.İnan ve M.Ali Akçayol, "GSM Tabanlı Akıllı Ev Uygulaması", Bilişim Teknolojileri Dergisi, Cilt: 2, Sayı: 2, Mayıs 2009.
- [5] B.Cincirop, "Gsm Kontrollü Akıllı Ev Otomasyonu", Sakarya Üniversitesi Elektronik ve Bilgisayar Eğitimi Yüksek Lisans Tezi, 2009.
- [6] T.Aydoğan, A.Çakır, M.A.Akça ve Y.E.Polat, "Telefonu İle Çağrı Otomasyonu".
- [7] C.Can, A.İpek, E.Azapoglu ve R.O.Turker, "Lazer Güvenlik Sistemi ve Gsm Haberleşme", MYO-OS 2010- Ulusal Meslek Yüksekokulları Öğrenci Sempozyumu.
- [8] İ.Çayıroğlu ve S.Görgünoğlu, "Mobil Telefon ve Pic Mikrodenetleyici Kullanarak Uzaktan Esnek Kontrol Sağlanması", Int.J.Eng.Research&Development, Vol.2, No.1, January 2010.
- [9] O.Tosunoğlu ve M.Göktürk, "Akıllı Ev Sistemlerinde Ethernet Üzerinden Cihaz Kontrolü Ve İzlenmesi", ELECO'2008, Elektrik-Elektronik-Bilgisayar Mühendisliği Sempozyumu ve Fuarı.
- [10] F.Kahraman ve A.F.Boz, "Web Tabanlı Otomasyon Sistemi Tasarımı ve Yapımı", 5. (IATS'09), 13-15, Karabük, Türkiye, Mayıs 2009.
- [11] S.T.Bushby, BACnet: a standard communication infrastructure for intelligent buildings, Automation in Construction 6 (1997) 529–540.
- [12] A.Kaklauskas, E.K. Zavadskas, Internetinė sprendimų parama (Web-based decision support), monograph, Technika, Vilnius, 2002, 216 pp. [in Lithuanian].
- [13] İ.Yabanova, S.Taşkın, H.Ekiz ve H.Çimen, "Denetleyici Alan Ağı Üzerinden Mekatronik Bir Sistemin Kontrolü", Makine Teknolojileri Elektronik Dergisi, Cilt: 7, No: 2, 2010.
- [14] L.Birgül ve G.Cansever, "Mikrokontrollör ile Akıllı Ev Otomasyonu ve Bilgisayar Arayüzü", ELECO'2008, Elektrik-Elektronik-Bilgisayar Mühendisliği Sempozyumu ve Fuarı.
- [15] U.Bayram, "Akıllı Ev Otomasyonu", Çanakkale Onsekiz Mart Üniversitesi Bilgisayar Bölümü Yüksek Lisans Tezi, 2006.
- [16] G.Arslanoğlu, "Rf Ev Otomasyonu", Gazi Üniversitesi Elektrik-Elektronik Mühendisliği Yüksek Lisans Tezi, 2009.
- [17] H.Korkmaz, "Akıllı Ev Otomasyonunun Mikrodenetleyici ile Gerçekleştirilmesi", Yıldız Teknik Üniversitesi Elektrik Mühendisliği Yüksek Lisans Tezi, 2007.
- [18] F.Cem Uzun, "Akıllı Binalarda Otomasyon", Makine Mühendisliği Yüksek Lisans Tezi, 2009.
- [19] M.T.Gençoğlu, "Akıllı evler", I.Mühendislik ve Teknoloji Sempozyumu (2008), pp.221-234.
- [20] A.Kaklauskas, E. Zavadskas, R. Ditkevičius, An intelligent tutoring system for construction and real estate, Lecture Notes in Computer Science, 4101, (2006), pp.174–181.
- [21] J.-H. Park, H.-S. Park, S.-J. Lee, J. Choi, D.-G. Lee, Intelligent multimedia service system based on context awareness in smart home, Lecture Notes in Computer Science, 3681, (2005), pp.1146–1152.
- [22] K.Schacht, New developments: smart materials (cutting edge, shape-memory properties, column), Appliance Manufacturer, 52, (1), (2004), pp. 14–16.
- [23] T.Staedter, The smart antenna (Visualize, brief article), Technology Review Cambridge, 106, (1), (2003), pp. 81–82.
- [24] J.Wong, H. Li, J. Lai, Evaluating the system intelligence of the intelligent building systems: Part 1: development of key intelligent indicators and conceptual analytical framework, Automation in Construction, 17, (3), (2008), pp. 284–302.
- [25] H.W. Kua, S.E. Lee, Demonstration intelligent building—a methodology for the promotion of total sustainability in the built environment, Building and Environment, 37, (3), (2002), pp.231–240.
- [26] J.K.W. Wong, H. Li, S.W. Wang, Intelligent building research: a review, Automation in Construction, 14, (1), (2005), pp.143–159.
- [27] J.Neelamkavil, Automation in the prefab and modular construction industry, 2009— 26th International Symposium on Automation and Robotics in Construction (ISARC 2009) Austin, Texas, USA, June 24–27, 2009, pp. 299–306.
- [28] Z.Chen, D. Clements-Croome, J. Hong, H. Li, Q. Xu, A multicriteria lifespan energy efficiency approach to intelligent building assessment, Energy and Buildings, 38, (5), (2006), pp.393–409.
- [29] H.Arkin, M. Paciuk, Evaluating intelligent building according to level of service system integration, Automation in Construction, 6, (1997), pp.471–479.
- [30] J.Naimavičienė, Intelligent knowledge and device based assisted residential environment: doctoral dissertation: technological sciences, civil engineering (02T), Vilnius Gediminas Technical University, Technika, Vilnius, (2008), pp.134
- [31] H.Şahin ve O.Hazer, "Akıllı Konut Teknolojileri", Gazi Üniversitesi Endüstriyel Sanatlar Eğitim Fakültesi Dergisi, Sayı:269, Mayıs 2010.
- [32] G.Wood, M. Newborough, Energy-use information transfer for intelligent homes: enabling energy conservation with central and local displays, Energy and Buildings, 39, (2007), pp.495–503.
- [33] A.M.Omer, Renewable building energy systems and passive human comfort solutions. Renewable and sustainable, Energy Reviews, 12, (6), (2008), pp.1562–1587.
- [34] D.W.Seward, S.D. Quayle, System architectures and safety for mobile construction robots, 13th Int. Symp. on Robotics in Construction, Tokyo, Japan, June 1996, pp. 727–732.
- [35] C.Soungho, K. Naruo, Application of location information by stereo camera images to project progress monitoring, ISARC 2007, September 2007, 24th International Symposium on Automation and Robotics in Construction, Indian Institute of Technology Madras, Kochi, India, September 2007, pp. 89–92.
- [36] G.J.Rios-Moreno, M. Trejo-Perea, R. Castañeda-Miranda, V.M. Hernández-Guzmán, G. Herrera-Ruiz, Modelling temperature in intelligent buildings by means of autoregressive models, Automation in Construction, 16, (5), (2007), pp.713–722.

- [37] C.E. Ochoa, I.G. Capeluto, Strategic decision-making for intelligent buildings: comparative impact of passive design strategies and active features in a hot climate, *Building and Environment*, 43, (11), (2008), pp.1829–1839.
- [38] O.Woodman, R. Harle, RF-based initialisation for inertial pedestrian tracking, in: H. Tokuda, et al., (Eds.), *Pervasive Computing*, 7th International Conference, Pervasive 2009, Nara, Japan, May 11–14, 2009, Proceedings. Lecture Notes in Computer Science, 5538, Springer, 2009, pp.238–255.
- [39] NanoLOC TRX - High Performance RF Transceiver with Location Awareness and Robust Wireless Communication, Fact Sheet. In http://www.nanotron.com/EN/pdf/Factsheet_nanoLOC-NA5TR1.pdf Nanotron Technologies, 2009.
- [40] A.Guillemain, N. Morel, An innovative lighting controller integrated in a selfadaptive building control system, *Energy and Buildings*, 33, (5), (2001),pp. 477–487.

BIOGRAPHY



Ahmet ŞENPINAR was born in 1973 in Elazığ, Turkey. Author received his MS (Electrical Systems) and PhD in Solar Energy Systems in 1997 and 2005 respectively from Firat University, Turkey. Currently, he is an assistant professor at College of Technical Sciences, Department of Electronics Technology, Firat University. His research interests are in pv systems and tracking systems.

Identification of abnormal DNS traffic via Hurst Parameter


A. Gezer

Abstract— It is a necessity for effective network management to be aware of the activities taking place on computer networks. Network managers should always be alarmed about what is happening now, what might be, or what will be in the future for the sake of network. To gather information about a computer system or a network, attackers mostly exploit networking tools to gain some privileges and login systems. Penetration testers also use these tools to gather information about systems, but their main concern is to discover the vulnerabilities of the system, and to find out what kind of measures could be applied to make the system more resistant to these vulnerabilities. In this study, we propose an abnormal DNS traffic identification method via utilizing Hurst parameter estimation. To do so, we employ DNS information gathering tools in Kali Linux to generate abnormal DNS flows. Then, we estimate its self-similarity degree to compare the differences between normal DNS traffic flows and abnormal ones. Obtained results show that abnormal DNS traffic show higher self-similarity degrees. Another interesting finding is that abnormal DNS traffic shows different distribution characteristic.

Index Terms— Traffic analysis, DNS protocol, distribution fitting, abnormal traffic detection

I. INTRODUCTION

NOWADAYS, we need computer network systems more than ever to fulfill our daily routines. The Internet is a global network which we couldn't endure its absence even for a few minutes. The usage of Internet is so widespread that we could perform most of our daily works such as banking, health care, navigation, food order, travel reservations, payment, mailing, telephone calling, and even education; almost all the things which used to need physical presence and effort in the past. Security is a significant issue for every type of computer system and network. We share our most secret credentials to the world through the Internet.

A. GEZER is with Department of Electrical and Computer Engineering, University of Alabama at Birmingham, Birmingham, Alabama USA (e-mail: aligezerr@hotmail.com) 

Manuscript received June 21, 2018; accepted July 25, 2018.

DOI: [10.17694/bajece.435230](https://doi.org/10.17694/bajece.435230)

Although the networking systems and technologies are getting safer, there are always malicious people whose aim are to cause harm to the computer systems, steal significant information, or use our network resources without permission. Attackers always stay vigilant for discovering system vulnerabilities and whenever, wherever possible they will carry out their attacks. For the sake of not only systems but also users, network administrators should also stay vigilant to verify that the network resources and policy are not being violated.

To ensure security and get rid of violations that put the systems in danger, firewalls are mostly used [1]. Although firewalls perform packet inspection, filtering, and prevent any login to systems through the Internet without permission, they don't ensure network system safety for all possible violations and intrusions [2]. In order to further strengthen the network from intruders, intrusion detection and intrusion prevention system usage are on the rise. Intrusion detection systems require monitoring the events occurring in a computer system or network and analyzes them for signs of possible violations, security threats and intrusions [3].

In this study, we focus on the identification of abnormal DNS traffic flows as an intrusion detection system which might be an indicator of an upcoming cyber-attack in advance. DNS packets could be exploited for malicious purposes in many ways. For example, some trojans benefit from a domain name generation algorithm (DGA) to conceal their command and control (C&C) servers [4]. Group activities in DNS traffic might be a signature of a botnet presence. A botnet detection method is proposed by monitoring group activities in DNS traffic [5, 6]. In [7], a DNS protection method is proposed against DNS Spoofing and Poisoning attacks. Attackers could also utilize DNS protocol to obtain information about a local area network before carrying out their attacks vector [8]. They might exploit some DNS tools for gathering information about a targeted domain. In this study, we will simulate this behavior to generate abnormal DNS traffic through exploiting some penetration testing tools. Penetration testing is a simulation of an attack on computer systems to find out the vulnerabilities on the systems and evaluate the security of the system being tested [9]. The basic concept behind this is to find out the vulnerabilities and the weaknesses of systems. Generally, penetration tests include three main steps for pen testing [10]. Sequentially, information gathering, attacking, and reporting. The information gathering phase might consist of

DNS gathering tools, web crawlers, sniffing technologies, spoofing and so on. The idea behind the information gathering phase is to scan and identify system specifications and vulnerabilities and exploit them in attacking. The obtained information about the system is utilized to drive the attack generation phase. Software developers could use this information to eliminate the vulnerabilities and improve the security of their software [9].

We propose an abnormal DNS traffic identification method through the Hurst parameter estimation procedure. The Hurst parameter, which is between 0 and 1, is a numerical measure of self-similarity. It gives information about long-range dependency and probability density characteristic of statistical times series. We generate abnormal DNS flows via exploiting some DNS information gathering tools to discover IP address of domains, domain names, subdomain names, name servers, and mail servers in a targeted domain. To do so, we employed some DNS information gathering tools in Kali Linux. These tools generally use the methods like DNS inquiries to DNS server, zone transfer, brute force, and google searches about a targeted domain. We analyze how these tools work to obtain DNS information on a domain. This process would give us detailed information about particular behaviors of some DNS information gathering tools. We also propose a method to identify abnormal DNS flows via the estimation of self-similarity parameter, namely the Hurst parameter. To compare the differences between normal DNS traffic and abnormal ones, we employ wavelet-based Hurst parameter estimation method. Normal DNS traffic flows are generated via interacting with popular internet domain names for the aim of comparing the self-similarity level of abnormal and normal DNS traffic.

II. BACKGROUND

A. KALILINUX

Developing tools for hacking and pen-testing purposes consumes a lot of times and is very demanding. Some software like Kali Linux makes it easy to carry out penetration tests. Kali Linux is a Debian based Linux distribution which is popular for penetration testing purposes. It was developed and maintained by Offensive Security [11]. It includes more than 600 tools for penetration testing such as information gathering, vulnerability identification, sniffing and spoofing, attacking, exploitation, forensic investigation tools, etc. It is an open source distribution, which means anyone can modify and enhance it via accessing its source code. Kali Linux can run on many different platforms; even on resource constrained devices such as a raspberry pi. It adheres to the Filesystem Hierarchy Standard. This allows users to easily locate supported files, libraries, and binaries [9].

B. SELF-SIMILARITY

A great variety of physical phenomena could be well represented via self-similar processes [12]. It has found a strong base in many disciplines such as biology, econometrics, natural images, fluctuations of the stock market and turbulence

[13, 14]. Self-similar processes have also been considered for modeling network traffic. Previously, network traffic was characterized with Poisson distribution [15]. However, Poisson distribution could not reflect the self-similar nature of network traffic. After modeling Ethernet traffic via self-similar processes, performance-related computations for network traffic such as resource sharing, queue and routing management have been revised [16]. Nowadays, self-similarity artifacts have been considered for the modelling of many broadband network traffic types [16–19].

As self-similarity is so significant in many disciplines, correct estimation of it is a necessity. Powerful properties of wavelet analysis have been an inspiration source for Hurst parameter estimation. Time-scale dependent working nature of wavelet analysis makes it a valuable candidate [20, 21]. An efficient wavelet-based Hurst parameter estimator called Abry-Veitch DWB was proposed in 1998 [22]. Abry-Veitch DWB used Daubechies wavelets as kernel function due to their limited time support which makes it more efficient for handling of border effects. Daubechies wavelets lead more accurate results by better matching self-similar structure of long range dependent processes [23].

The Hurst parameter indicates whether a stochastic process is long range dependent or not. It is a numerical measure of self-similarity. A continuous time stochastic process $\{X(t), t \in \mathbb{R}\}$ is strictly self-similar with the Hurst parameter $\{H, 0 < H < 1\}$ if

$$X(at) \stackrel{d}{=} a^H X(t). \quad (1)$$

$X(at)$ is a new process scaled by factor a and $\stackrel{d}{=}$ means equal in finite dimensional distributions. When the Hurst value is 0.5, the process is randomly scattered. Let X_k is a discrete time stochastic process, which is defined at discrete time points $k=1, 2, \dots, n$ and $X_k^{(m)}$ is m aggregated time series which is calculated as

$$\{X_k^{(m)} = (X_{km-m+1} + \dots + X_{km})/m, k \geq 1, m = 1, \dots\} \quad (2)$$

$$\text{Var}[X_k^{(m)}] = m^{2H-2} \text{Var}[X_k] \quad (3)$$

$$\rho_z^{(m)} = \rho_z, z \geq 0. \quad (4)$$

If variance and correlation of the time series follows (3) and (4), then the process is called wide sense self-similar or second order self-similar. $\rho_z^{(m)}$ shows autocorrelation coefficient of m aggregated series with respect to lag z .

III. METHODOLOGY

A. BEHAVIORAL ANALYSIS OF DNS TOOLS IN KALI LINUX

Basically, a domain name system (DNS) resolves host names into IP addresses. It is among the core parts of TCP/IP protocol suite. Before downloading packets from a web site, it is

required to resolve the IP address of that web site. There is an ID part in every DNS query. A DNS server replies to a DNS query with the IP address of the URL by putting the same ID which was used in the query [24]. This process between the host and DNS server is open to many attacks because the packet exchange between the two ends occur in plain text. So, any packet sniffer which is located in a strategic position could capture packets and reveal the content easily. DNS information might be used for some malicious purposes such as gathering information about a domain before attacking.

In this section, we test some of DNS information gathering tools in Kali Linux. While carrying out this operation, we also capture the exchanged packets with a protocol analyzer. A protocol analyzer could capture all the packets that pass through the network and monitor the bottlenecks in the network, alert the user to irregular behavior in the network, provide useful information to the network administrator, and reveal packet content which also contains passwords [25].

Generally, packet sniffers are utilized by network managers to troubleshoot the network problems via analyzing passing traffic to find out any problematic traffic such as intrusions, malicious packets, or if there is any user who violates network policy. We utilize a protocol analyzer to capture the traffic and reveal the packet exchange process while executing DNS information gathering commands in Kali Linux. The behavior of the traffic can be compared to an established policy for deviations to further investigate the differences between normal DNS traffic and the traffic from an information gathering tool.

i. Dnsenum

Dnsenum is a tool used for information gathering about name servers, mail servers, and subdomains. The packet traffic is captured via a packet sniffer when we execute the Dnsenum command in Kali Linux and identify what are the exchanged packet contents during this operation. The packet exchange pattern is summarized in Table 1.

Table 1 The packet exchange pattern for Dnsenum

Requests and Replies
IP address of the desired domain
Name server name from the DNS server
IP address of name server
Mail exchange server of that particular domain
IP addresses of the mail servers
Again, IP address of the name server
IPv6 address of name server
Zone transfer is tried between the particular name server and resolver host
Scraping of given domain name through Google Search

ii. Dnsmap

Dnsmap tool is used generally for subdomain scans. A built-in word list is used for scanning subdomain names and IP addresses. According to the built-in word list, IP addresses of domain names are requested from the DNS server. Overall, more than 3000 DNS queries are raised to the DNS server for

subdomain IP addresses. At the end of scanning, the number of subdomain names and IP addresses are given as a report on the Kali Linux screen. Most of the DNS queries take DNS error messages.

iii. Dnswalk

Dnswalk is used for zone transfer. According to the captured packets after execution of the Dnswalk command, the packet exchange process could be summarized as in Table 2.

Table 2 The packet exchange process for Dnswalk

Requests and Replies
Request to mark the start of zone transfer
Name server name from the DNS server
IP address of name server from DNS server
IPv6 address of name server from DNS server
Zone transfer is tried for a particular name server
Scraping of given domain name by Google search

iv. Dnsrecon

With using Dnsrecon in Kali Linux, one can reach a lot of information about subdomain names and IP addresses. The usage of the command is also customizable by changing parameters in the command line. With the goo parameter, it gets subdomain names using a Google search. Once the command is executed, it sets up a TCP connection between the host computer and Google servers. After getting subdomain names, DNS queries are raised to ask their IPv4 and IPv6 addresses to the DNS server and finally give them as a report on the Kali Linux terminal screen.

With the -tld parameter, it performs DNS queries according to the typed domain name in command line. Built-in word list is used for second order domain names. All generated DNS queries are requested from the DNS server. Mostly, the returned answers aren't associated with the desired domain name.

v. Fierce

Subdomain names and IP addresses of subdomains could be fetched with the execution of the Fierce command. Fierce usage could be customized with some extra parameters. With the usage of the DNS parameter, at first the name of name server query is raised to the DNS server. Then, IP address of the name server is requested from DNS server. Another query is raised for the IPv6 address of the name server. After obtaining the IP information of the name server of the interested domain, a TCP connection is established between the name server and the host for zone transfer. Mostly, the name server rejects zone transfer. A Brute Force method is attempted to obtain subdomain names and their IP addresses from the name server of the desired domain.

vi. Dmitry

Lots of information could be gathered such as subdomains, e-mail addresses, and port scan with this tool. After executing Dmitry in Kali Linux, we capture the packet traffic with a packet sniffer application. First, the IP address of the desired domain is requested from the DNS server. After getting the IP address, the Ripe.net IP address is requested from the DNS

server. Then, a TCP connection is established between Ripe.net and the host computer to investigate the IP address of the typed domain name. Ripe.net gives IP address ranges for that domain and the information about the organization who owned that IP address. Next, the Whois-servers.net IP address is raised to the DNS server. A TCP connection has been established with the Whois server. Mail addresses, phone numbers, and organization names are obtained from the Whois server. Then the uptime.netcraft.com IP address is requested from the DNS server and a TCP connection is established for searching particular domain addresses. Then a Google-based search is performed after obtaining the IP address from DNS server. Google returns a lot of subdomain names. After getting subdomain names from servers, DNS queries are raised to the DNS server to learn their IP addresses. At the end, a port scan is performed.

B. ABNORMAL DNS TRAFFIC IDENTIFICATION VIA HURST PARAMETER

We employ the aforementioned DNS tools in Kali Linux to gather information about sub-domains, name servers, and mail servers on two domains: www.erciyes.edu.tr and www.mit.edu.tr. Abnormal DNS flow traffics are generated via exploiting DNS information gathering tools while benign traffic captures are generated through network interaction with some popular web sites.

Table 3 Captured DNS Traffic

Datasets	DNS packet counts
Dataset 1 (Normal)	7268
Dataset 2 (Normal)	33522
Dataset 3 (Abnormal)	30344
Dataset 4 (Abnormal)	77519

The content of captured DNS traffic is given in Table 3. Dataset 1 is obtained during the interaction with some well-known web sites in Turkey such as university domains, online newspaper, and some public enterprise websites. Dataset 2 is generated via visiting the Top 215 global URLs in the Alexa top 500 global web sites list. Captured DNS packets during these interactions are counted as normal DNS datasets. Dataset 3 and Dataset 4 are obtained via exploiting mentioned DNS information gathering tools on www.erciyes.edu.tr and www.mit.edu.tr domains, respectively.

In the Hurst estimation procedure, Wavelet-based Hurst estimation method is employed to get the self-similarity degree of packet length and inter-arrival time of DNS traffic. Hurst parameters of the given flows are easily calculated through the relationship between variance of wavelet coefficients and corresponding scale [24] as given in the equation (5)

$$\log_2(\text{var}(d_j[n])) = (2H - 1)j + \text{const.} \tag{5}$$

where $d_j[n]$ represents the wavelet coefficients at j scale, and H represents Hurst parameter. The slope between $\log_2(\text{var}(d_j[n]))$ and j are in relation with $2H-1$. Therefore, Hurst

parameter could be calculated utilizing this regression line. Each point in Figure 1 and Figure 2 is computed through the variances of wavelet coefficients at the corresponding scale for DNS packet interarrival times and packet length obtained when DNS information gathering tools are employed for www.mit.edu.tr domain.

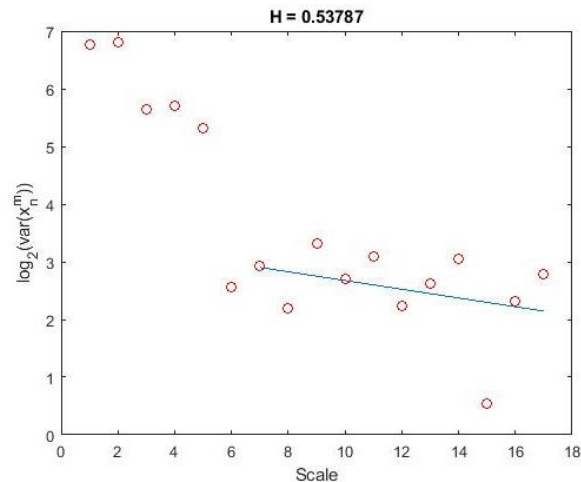


Fig. 1 Wavelet-based self-similarity estimation of inter-arrival times of DNS packets (Utilization of DNS information gathering tools for www.mit.edu.tr domain)

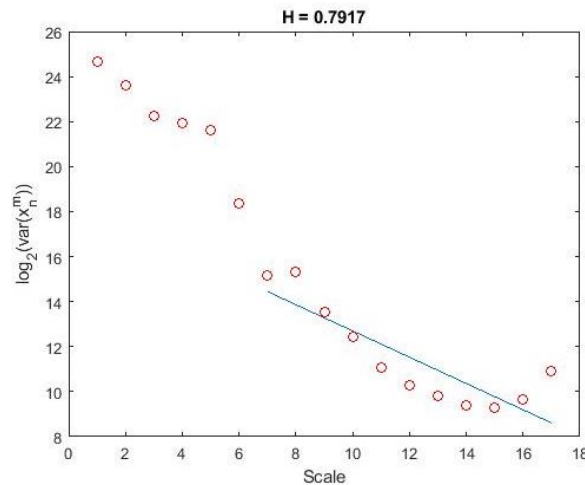


Fig. 2 Wavelet-based self-similarity estimation of DNS packet length (Utilization of DNS information gathering tools for www.mit.edu.tr domain)

Similar figures are obtained during the variance computations of wavelet coefficients at each scale for all Datasets in Table 3. Due to the resemblances in figures, only the associated figures with Dataset 2 and Dataset 4 are shared in the manuscript. Figure 3 and Figure 4 illustrate the variance of wavelet coefficients at corresponding scale for DNS packet interarrival time and packet length computed during the visit of Top the 215 URLs in the Alexa top 500 global web site list.

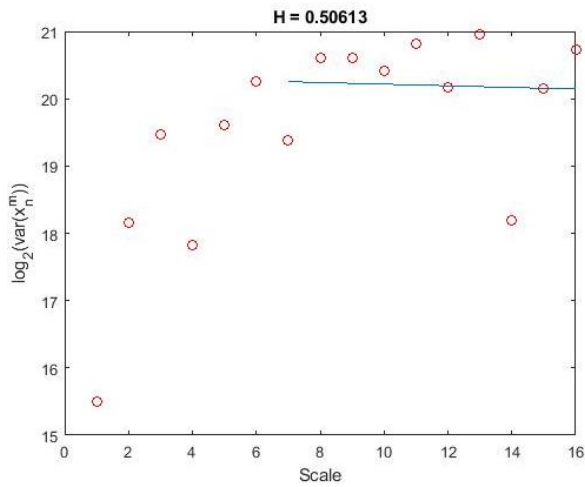


Fig. 3 Wavelet-based self-similarity estimation of inter-arrival times of DNS packets (Top 215 URLs in Alexa top 500 global web sites)

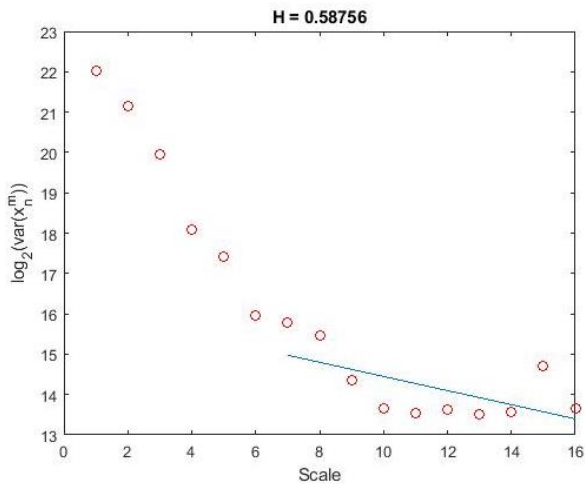


Fig. 4 Wavelet-based self-similarity estimation of DNS packet length (Top 215 URLs in Alexa top 500 global web sites)

The Estimated Hurst values for each data set are given in Table 4 for DNS packet inter-arrival times and DNS packet lengths.

Table 4 Hurst estimation values of each dataset via Wavelet-Based methods

Datasets	DNS packet inter-arrival time	DNS Packet Size
Dataset 1 (Normal)	0.4828	0.4906
Dataset 2 (Normal)	0.5061	0.5876
Dataset 3 (Abnormal)	0.5515	0.8334
Dataset 4 (Abnormal)	0.5379	0.7917

It is observed that abnormal DNS datasets give greater Hurst values for both DNS packet interarrival times and packet lengths. Obtained results demonstrate that Hurst parameters could be an indicator of abnormal DNS traffic, and it might presage an upcoming cyber-attack in advance.

C. DISTRIBUTION ANALYSIS

In this section, our aim is to obtain a fitted distribution function for the modeling of packet sizes of normal and abnormal DNS packet traffic. Distribution functions could be an efficient way of characterizing network traffic due to their non-deterministic behavior. If abnormalities in DNS traffic could be represented with distribution functions, this characteristic could be an indicator of possible cyber-attacks. In the distribution fitting procedure, we test 73 different distribution functions. As selection criteria for goodness of fitting, we employ Kolmogorov Smirnow results and determine the fitted distribution types for packet sizes of normal and abnormal DNS traffic.

Pareto Distribution gives the best result for Dataset 2 which is obtained through the visiting of 215 URLs in the Alexa Top 500 Global web sites. The probability density function of Pareto Distributions is as follows,

$$F_x(x) = \begin{cases} 1 - (\frac{x_m}{x})^\alpha & x \geq x_m, \\ 0 & x \leq x_m. \end{cases} \quad (6)$$

Figure 5 shows the cumulative distribution and fitted distribution for Dataset 2. According to the test result, the Pareto distribution parameters α and β are 1.2048 and 61 respectively.

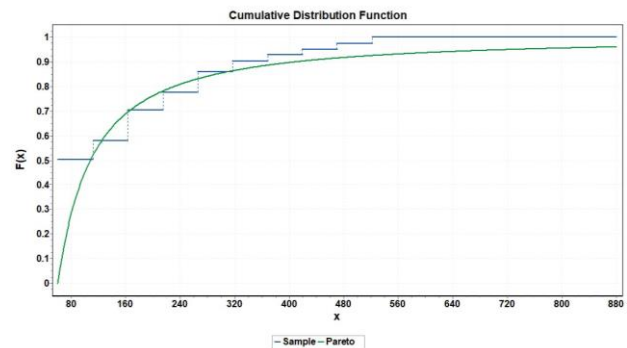


Fig. 5 Packet size distribution of normal DNS traffic (Top 215 URLs in Alexa top 500 global web sites)

Phased Bi-Exponential gives the best result for Dataset 4 which is obtained utilizing DNS information gathering tools for the targeted domain. The probability density function of Phased Bi-Exponential is as follows,

$$F_x(x) = \begin{cases} \lambda_1 e^{-\lambda_1(x-\gamma_1)} & \gamma_1 \leq x \leq \gamma_1, \\ \lambda_2 e^{-\lambda_2(x-\gamma_2)-\lambda_1(\gamma_2-\gamma_1)} & \gamma_2 \leq x \leq +\infty. \end{cases} \quad (7)$$

Figure 6 shows the cumulative distribution and fitted distribution for Dataset 4. According to the test results, the Phased Bi-Exponential distribution parameters λ_1 , γ_1 , λ_2 , and γ_2 are 0.02468, 66, 4.9635E-5, and 476 respectively.

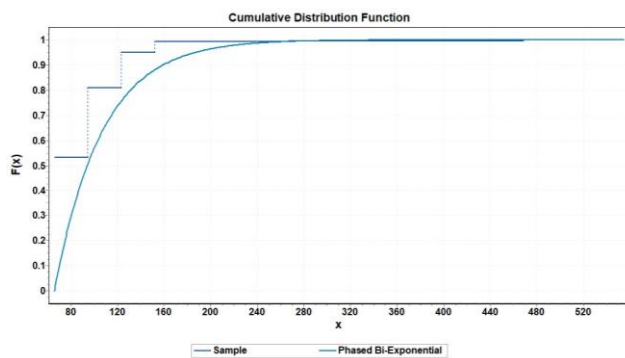


Fig. 6 Packet size distribution of abnormal DNS traffic (Utilization of DNS information gathering tools for www.mit.edu.tr domain)

Obtained results demonstrate that distribution characteristic is a significant feature to identify abnormal DNS traffic.

IV. CONCLUSIONS

Identification of abnormal DNS traffic might presage some cyber-attacks that could take place in the future. We demonstrate that Hurst-parameter estimation might be an indicator of abnormal DNS traffic identification method. To do so, we generate abnormal DNS traffic via utilizing pen testing tools in Kali Linux. We also generate normal DNS packets via interacting with some popular domains in the Alexa top 500 global web sites. Obtained results show that abnormal DNS traffic gives greater Hurst values compared to normal DNS traffic. Therefore, it is understood that Hurst parameter could be an indicator of abnormal DNS traffic. According to Kolmogorov Smirnov test statistics, Pareto distribution could be used to model normal DNS traffic which is obtained during the interaction of the first 215 URLs in the Alexa top 500 global web sites. However, Phased Bi-Exponential gives the best fitting results for abnormal DNS traffic, which is obtained by utilizing some DNS information gathering tools on targeted domains.

ACKNOWLEDGMENT

The authors would like to thank the editors and anonymous reviewers for their valuable suggestions and comments. I would like to thank Dr. Murat M. Tanik for his support, encouragement and guidance.

I also would like to thank Michael Mistretta for helping in the review of the study.

I would like to thank, TUBITAK-Directorate of Science Fellowships and Grant Programmes (BIDEB) to support my postdoctoral research project coded with 1059B191600549 application number.

REFERENCES

- [1] H. Chen, J.H. Cho, and S. Hu, "Quantifying the Security Effectiveness of Firewalls and DMZs", In Proceedings of the 5th Annual Symposium and Bootcamp on Hot Topics in the Science of Security, ACM, 2018.
- [2] A. Patel, M. Taghavi, K. Bakhtiyari, and J. Celestino Júnior. "An intrusion detection and prevention system in cloud computing: A systematic review", Journal of network and computer applications, vol. 36, no. 1, 2013, pp- 25-41.
- [3] U.A. Sandhu, S. Haider, S. Naseer, and O. U. Ateeb, "A survey of intrusion detection & Prevention Techniques", 2011 International Conference on Information Communication and Management IPCSIT, vol. 16, Singapore, 2011, pp. 66-67.
- [4] M. Wielogorshka, and D. O'Brien, DNS Traffic Analysis for Botnet Detection.
- [5] C. Hyunsang, H. Lee, H. Lee, and H. Kim. "Botnet detection by monitoring group activities in DNS traffic", In Computer and Information Technology, 2007. CIT 2007. 7th IEEE International Conference on, 2007, pp. 715-720.
- [6] C. Hyunsang, and H. Lee. "Identifying botnets by capturing group activities in DNS traffic", Computer Networks, vol. 56, no. 1, 2012, pp. 20-33.
- [7] M.A. Hussain, H. Jin, Z.A. Hussien, Z.A. Abduljabbar, S.H. Abbdal, A. Ibrahim, "DNS Protection Against Spoofing and Poisoning Attacks", 3rd International Conference on Information Science and Control Engineering (ICISCE), Beijing China, 2016, pp. 1308-1312.
- [8] M. Anagnostopoulos, G. Kambourakis, P. Kopanos, G. Louloudakis, and S. Gritzalis. "DNS amplification attack revisited." Computers & Security 39, 2013, pp. 475-485.
- [9] D. Matthew, Z. Carlos, and H. Thaier, "Penetration Testing: Concepts, Attack Methods and Defense Strategies, Systems", Applications and Technology Conference (LISAT), 2016 IEEE Long Island, NY USA, 2016.
- [10] W.G.J. Halfound, S.R. Choudhary, and A. Orson, "Penetration Testing with Improved Input Vector Identification", Software Testing Verification and Validation, 2ICST'09, Denver Co, USA, 2009, pp. 346-355.
- [11] Kali Linux by Offensive Security, <https://www.kali.org/>, accessed September 2017.
- [12] S. Giardano, S. Miduri, M. Pagano, F. Russo, S. Tartarelli, "A wavelet-based approach to the estimation of Hurst parameter for self-similar data", International Conference on Digital Signal Processing, DSP 97 2, 1997, pp. 479-482.
- [13] M. Barnsley, "Fractals Everywhere", Academic Press, San Dieog, 1998.
- [14] J. Beran, "Statistics for Long Memory Processes", Chapman & Hall, New York, 1994.
- [15] V. Paxson, S. Floyd, "Wide area traffic: the failure of Poisson modeling", IEEE/ACM Transactions on Networking, vol. 3, no. 3, 1995, pp. 226-244.
- [16] W.E. Leland, M.S. Taqqu, W. Willinger, D.V. Wilson, "On the self similar nature of Ethernet traffic (extended version)", IEEE/ACM Transactions on Networking, vol. 2, no. 1, 1994, pp. 1-15.
- [17] J. Beran, R. Sherman, M.S. Taqqu, W. Willinger, "Long-range dependence in variable-bit-rate video traffic", IEEE Transactions Communications, vol. 43, no. 234, 1995, pp. 1566-1579.
- [18] M.E. Crovella, A. Bestavros, "Self similarity in world wide web traffic: evidence and possible causes", IEEE/ACM Transactions on Networking, vol. 5, no. 6, 1997, pp. 835-846.
- [19] D.P. Heyman, T.V. Lakshman, "What are the implications of long-range dependence for VBR-video traffic engineering?", IEEE/ACM Transactions on Networking, vol. 4, no. 3, 1996, pp. 301-317.
- [20] E. Masry, "The wavelet transform of stochastic processes with stationary increments and its application to fractional Brownian motion", IEEE Trans. Inform. Theory, Vol. 39, no. 1, 1993, pp. 260-264.
- [21] G. Womell, "A Karhunen Loe've like expansion for 1/f processes via wavelets", IEEE Trans. Inform. Theory, Vol. 36, No. 4, pp. 859-861, 1990.
- [22] P. Abry, D. Veitch, "Wavelet Analysis of Long-Range-Dependent Traffic", IEEE Transactions on Information Theory, Vol. 44, No.1, pp. 2-15, 1998.
- [23] H. J. Jeongy, D. McNicklez, K. Pawlikowski, "Fast Self-Similar Teletraffic Generation Based on FGN and Wavelets", IEEE International Conference on Networks, Brisbane, Australia, 1999, pp. 75-82.
- [24] R. Bassil, R. Hobeica, W. Itani, C. Ghali, A. Kayssi, and A. Chehab, "Security Analysis and Solution for Thwarting Cache Poisoning Attacks in the Domain Name System", Proceedings of the 19th IEEE International Conference on Telecommunications (ICT'12), Lebanon, 2012, pp. 1-6.
- [25] A. Pallavi, P. Hemlata, Network Traffic Analysis Using Packet Sniffer, International Journal of Engineering Research and Applications, Vol. 2, No. 3, 2012, pp. 854-85

BIOGRAPHIES



Ali GEZER was born in Kayseri City, Turkey, in 1976. He received the B.S. degree in Electronic and Computer Education from Marmara University in 1999 and M.S. degree in computer engineering from Erciyes University in 2004, and the Ph.D. degree in electronic engineering from Erciyes University, Kayseri, TURKEY, in 2011.

He is an Assistant Professor with the Electronic and Communication Technology in Erciyes University. Nowadays, He is doing post-doctoral research study at University of Alabama at Birmingham. His research interests include internet traffic, self-similarity, traffic modeling, signal processing techniques, communication technologies, IoT botnet.

Analysis of the Effect of Uncertain Renewable Sources on Static Voltage Stability by Using NR-Based DSOPF Model with Adapted IEEE-30 Bus Test System

B. Baydar, H. Gozde, and M.C. Taplamacioglu

Abstract—This study examines the uncertainty effect of renewable energy resources on the static voltage stability thanks to modeling a specific area of Turkish electricity network by using classic IEEE 30-bus test system. For this purpose, the classic IEEE 30-bus test system is adapted to the Turkish electricity network by using new approach proposed in the study, which is based on the 2015 Turkey real and reactive load curves. In this way, the classic IEEE 30-bus test system is considered a part of Turkish electricity network. The analyses are performed on this model using Newton-Raphson (NR) solution by established three Optimal Power Flow (OPF) studies: dynamic-OPF study without renewable sources, dynamic-OPF study with renewable energy sources having constant power output, Dynamic-Stochastic Optimal Power Flow (DSOPF) study with uncertain renewable energy sources. To take into account the uncertainty effects, Weibull Probability Distribution Function (PDF) using Turkey wind and solar data are used for each month. At the end of the study, it is observed that the integration of uncertain renewable energy sources into the Turkey electricity power system largely decreases both the yearly total generation cost and the reactive power generation.

Index Terms—Optimal power flow, Renewable energy sources, Static voltage stability, Uncertainty effect, Weibull probability distribution function.

I. INTRODUCTION

RENEWABLE ENERGY SOURCES are increasing day by day the share of world electricity energy production in total installed capacity. The remaining 100-150 years of life of fossil-based energy reserves and the serious and now irreversible damages of climate change and global warming impacts that our world faces due to their use are compelling reasons for this increase.

B. BAYDAR, is with Baskent Electricity Distribution Company, EnerjiSA, Ankara, Turkey, (e-mail: basar.baydar@baskentedas.com.tr).

H. GOZDE, is with Department of Electronics and Communication Engineering, National Defence University, Military Academy, Ankara, Turkey, (e-mail: hgozde@kho.edu.tr).

M. C. TAPLAMACIOGLU, is with Department of Electrical and Electronics Engineering University of Gazi, Ankara, Turkey, (e-mail: taplam@gazi.edu.tr).

Manuscript received May 14, 2018; accepted June 21, 2018.

DOI: [10.17694/bajece.423459](https://doi.org/10.17694/bajece.423459)

Additionally, the use of renewable energy sources as much as possible in electricity generation is also a necessity in terms of reducing the cost of electricity energy consumption which is rapidly increasing in parallel with developing technology. In theory; it is clear that the use of renewable energy sources with a source nature of almost zero cost instead of relatively costly power plants such as fossil-fueled natural gas plants that are commissioned to meet additional demand at peak times in a continuously changing supply-demand balance will greatly reduce electricity energy consumption prices. Practically, this is proved by the countries that increase the use of renewable energy. For example; It was reported that the price of electricity in Germany has been about 80 €/MWh in peak hours in 2008 and it has been decreased to 38 €/MWh in 2013 with the increase in renewable energy plants [1]. In parallel with these factors, the share of renewable energy sources in the world electricity energy production was determined as 21% in 2015. It has been estimated to be around 30% in 2035. In 2016, the world's net capacity additions obtained from renewable energy sources was around 66%, while the installed capacities of the coal and gas power plants declined in the same year [2]. In terms of net capacity increase, solar energy power plants rose for the first time in the world with an increase of 75 GW for the first time [3]. Similarly, the proportion of renewable energy sources in the net additional capacity in Turkey was 55% in 2016. By the end of 2017, the total installed capacity of renewable energy plants in Turkey has reached approximately 39 GW [4]. It is planned to increase this power to 60 GW by 2023. In this regard, it is planned that worldwide until 2030, CO₂ emission from fossil-based electricity generation plants will be reduced by 40% [3].

Whereas; the increase in the proportion of renewable power plants in total installed capacity brings some problems affecting the power quality of the countries in the electricity grid and the interconnected system. It is possible to divide these problems in general into the problems related to integration and stability. It can be said that the integration problems are mostly related to the infrastructure competencies of the distribution and transmission networks of the countries. For example, the active and reactive power capacity competencies of the transformer substations in the distribution network include the basic factors such as the availability of transformer substations with sufficient short circuit power capacity in the region according

to the capacity of the renewable plant to be connected and the active and reactive power carrying capacities of the respective transmission lines. The solutions of these problems depend on the countries' midterm and long-term electricity infrastructure improvement, renewal and expansion plans. On the other hand, the stability problems can be caused from both the power network and the renewable power plant itself. It is clear that the uncertain nature of the renewable resources is the most effective reason of these problems. In literature, the uncertainty effect of the renewable resources to the power network has been examined so far by using different OPF models. It is known that the classic OPF analysis provides only instant information about the power system. To reach the more realistic long-term results, the analyses are spread periodically throughout months, years etc. by using dynamic-OPF analysis. In addition, these long-term dynamic-OPF analyses are improved to the stochastic-dynamic OPF by taking into account uncertainties of the process. At the recent ones, Liang et al. presented a wide-area measurement based DSOPF algorithm using the adaptive critic design (ACD) technique in 2012 [5]. In 2014, Gill et al. proposed the dynamic-OPF analysis for active distribution power system [6]. Two years after, Wei et al. proposed an integration technique of DG based on stochastic OPF model [7]. At the same year, Sun et al. proposed a DSOPF for wind farms and EVs integrated power system based on the chance-constrained programming model [8], then Bai et al. were aimed to reduce the expected operational cost by using 94 wind power plants in Texas developed with raw data and using the model to estimate hourly wind energy outputs for 24 hours [9]. In 2017, in his doctoral dissertation, Bai utilized a probabilistic forecast model, dynamic factor model (DFM), to predict wind power. This work also focuses on the optimization of the system integrated with wind power and storage devices over 24 hours. In this doctoral dissertation, has been tested on small, medium and large power system for OPF (IEEE-30, IEEE-57 and IEEE-118 buses) and then it was modified and extended to solve a dynamic optimization problem recursively [10].

This study examines the uncertainty effect of renewable energy resources on the static voltage stability is examined thanks to modeling a specific area of Turkish electricity network by using IEEE 30-bus test system. For this purpose, IEEE 30-bus test system is adapted to the Turkish electricity network by using new approach proposed in the study, which is based on the 2015 Turkey real and reactive load curves obtained from TEİAS for the year of 2015 for Turkey. In this way, IEEE 30-bus test system is considered a part of Turkish electricity network. The analyses are performed on this model by established three OPF studies: dynamic-OPF study without renewable sources, dynamic-OPF study with renewable energy sources having constant power output, DSOPF study with uncertain renewable energy sources. All models have contained IEEE 30-bus test system arranged monthly in accordance with these load curves. The behavior of modified IEEE 30-bus system has been examined only at the first model for being reference. The renewable power plants have been integrated to this model in the second one. Finally, the third model has been composed to include the uncertainty of the renewable resources. To take into account the uncertainty effects, Weibull probability distribution function using Turkey wind and solar data are used for each month.

This article is organized as follows; the OPF problem and the new OPF models are summarized in Section II. Proposed OPF models are explained in Section III. The case studies for examinations are presented and discussed in Section IV and they are concluded in the Conclusion section.

II. OPTIMAL POWER FLOW PROBLEM

The Optimal Power Flow (OPF) was first introduced by Carpentier in 1962 [11]. It is defined as the production sharing of optimal power exchange between generators and barriers in production, without exceeding the physical limits of the equipment used in the power systems. Actually, OPF is a nonlinear optimization problem including a flow which must be optimized, a desired equality, inequality constraint, and a problem solving method [12, 13]. In other words, the OPF optimizes a certain the power flow within an electrical power system without violating power flow restrictions and operational limits [14, 15]. Conclusively, it maximizes the energy quality and determines the optimal working condition for the power system.

The general OPF problem is formulated in Equation 1 [16]:

$$\begin{aligned} f(x, u) &= 0 - \text{is objective function} \\ g(x, u) &= 0 - \text{is equality constraints} \\ h(x, u) &\leq 0 - \text{is inequality constraints} \end{aligned} \quad (1)$$

Where:

$f(x, u)$ - is the minimization function to optimize the solution,
 $g(x, u)$ - represents the power flow equations,
 $h(x, u)$ - represents the power system safety limits,
 x, u - are the status and control variables, respectively.

The state variables of the power system are the real output power of the slack bus, the voltage amplitudes of the load buses and the reactive output powers of the generator buses as depicted in Equation (2):

$$x = [P_{slack}, V_L, Q_g] \quad (2)$$

The control variables include the real output powers of the generator buses except slack bus, voltage magnitudes of the generator buses, transformer tap-changes and shunt capacities as represented in Equation (3):

$$u = [P_g, V_g, T, Q_c] \quad (3)$$

The general cost function F_{cost} in order to minimize the entire production cost of the power system can be determined as Equation (4):

$$F_{yakta} = \sum_{i=1}^{N_g} (\alpha_i + \beta_i \cdot P_{gi} + \gamma_i \cdot P_{gi}^2) \quad (4)$$

Where:

N_g - is the number of generators in the power system,
 P_{gi} - is the real powers of the generators,
 α_i, β_i and γ_i - are the generator fuel cost coefficients.

Finally, the real and reactive power at bus k from the system can be given as Equation (5) and Equation (6):

$$P_k = 0 = V_k \sum_{m=1}^N [V_m [g_{km} \cdot \cos(\delta_k - \delta_m) + b_{km} \cdot \sin(\delta_k - \delta_m)]] - P_{GK} + P_{LK} \quad (5)$$

$$Q_k = 0 = V_k \sum_{m=1}^N [V_m [g_{km} \cdot \sin(\delta_k - \delta_m) - b_{km} \cdot \cos(\delta_k - \delta_m)]] - Q_{GK} + Q_{LK} \quad (6)$$

The required limits generator real power, generator reactive power, bus voltage magnitude, transformer tap-changing value and shunt capacity can be arranged according to the nature of the application.

On the other hand the OPF problem has been extended to the different OPF models according to solution requirements, especially for renewable energy sources with uncertainty. Some of them are summarized as follows:

Static OPF: Static OPF model defines the classic OPF problem. It can only manage a single load level at a certain time [17].

Dynamic OPF: This OPF model is similar to the static one. The difference is that the dynamic OPF model covers multiple time periods [18, 19].

Transient stability-constrained OPF: This problem handles static and dynamic constraints of the power network simultaneously during the optimization process [19]. In this case, the system can withstand serious hazards [20].

Security-constrained OPF: This is another extended version of the OPF which involves constraints arising from the operation of the system under a set of postulated contingencies. SCOPF studies help to overcome when any real contingency happens by rescheduling / controlling to make sure that system is within the allowed limits of operation and termed as steady state security [21].

Deterministic OPF: This derivatization based OPF model does not take into account the stochastic factors. The deterministic OPF is a typical short-term decision-making tool used by a number of utilities and its implementation in this work aims to give a reasonable benchmark for comparison. Traditional deterministic OPF models dispatch controllable generation using the central (most likely) wind forecast, i.e., they do not endogenously account for the variability and uncertainty of wind generation [22].

Stochastic OPF: This type of OPF model takes into account the uncertainties in the power system parameters [23, 24]. Indeed, uncertainty sees it as part of constraints and objective models. For this reason, optimization process and final OPF results may be affected by uncertain factors [25]. These uncertainties can be changes of the wind for a wind turbine.

Probabilistic OPF: Estimates the probability distribution functions of dependent variables based on probability distributions of loads and other indeterminate factors using Monte Carlo Simulation [26], Cumulant method [27], Point Estimation Method (PEM) [28], and adapted Gaussian mixture model [29] uncertain factors do not affect the final results.

AC OPF: The AC OPF model is associated with the AC power network and is based on the natural power flow characteristics of the system [30]. As a result, the results obtained with this type of OPF are more accurate [31].

DC OPF: This type of OPF does not consider reactive power and transmission losses [30].

Mixed AC/DC OPF: Both AC and DC parameters in the power system are associated with OPF [32].

In this study, the dynamic OPF model and the stochastic OPF model are combined with each other in order to examine the effect of uncertain variations at the renewable energy resources to the static stability of the power system as explained below. For this purpose, while the dynamic OPF is modeled in a year period for monthly, the stochastic OPF is modeled with Weibull PDF of sun radiation and wind variation for each the month.

III. PREPARATION OF DSOPF MODEL

The IEEE 30-bus test system is used as an example power system in this study [33]. To preparation of the combined DSOPF model, the three regulations explained below have been performed on the IEEE 30-bus test system. In this way, the three OPF model are obtained as;

Model-1: Monthly dynamic OPF model for a year on the IEEE 30-bus test system,

Model-2: Monthly dynamic OPF model for a year on the IEEE 30-bus test system with static renewable sources,

Model-3: Monthly combined DSOPF model for a year on the IEEE-30 bus test system with uncertain renewable sources modeled with Weibull PDF.

After that, the three case studies have been realized using these three models in order to examine the effect of uncertain variations at the renewable energy resources to the static voltage stability of the power system.

3.1 Regulation-I

In this regulation, the standard IEEE 30-bus test system is re-organized monthly as a dynamic OPF model according to the real and reactive power load curves of 2015 obtained from the TEIAS annual sector reports [34]. This load curves are represented in Fig. 1.

Turkey's monthly real and reactive power consumption peak values of 2015 obtained from these curves are used to calculate the monthly values of constant total real and total reactive powers for the IEEE 30-bus test system as explained below. For this purpose, the total real and reactive powers of the IEEE 30-bus test system replaced with the peak values of the curves for each month.

$$Real\ Power'(Month) = \frac{Real\ Power\ (Month)}{Peak} \times Peak_{IEEE30} \quad (8)$$

$$Reactive\ Power'(Month) = \frac{Reactive\ Power\ (Month)}{Peak} \times Peak_{IEEE30} \quad (9)$$

Sampling for real and reactive power for January, it will be as follows;

$$256,7\ MW = \frac{6328,2\ MW}{6984,2\ MW} \times 283,4\ MW$$

$$256,7\ MVar = \frac{1248,9\ MVar}{1400,9\ MVar} \times 126,2\ MVar$$

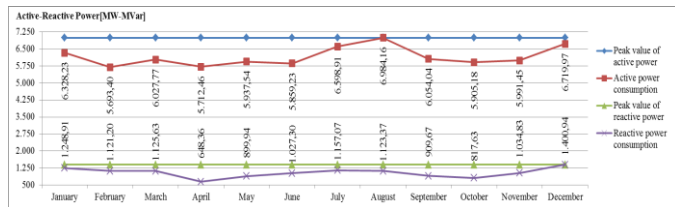


Fig.1. Turkey real and reactive power load curves for the year of 2015 [34]

After that, the load sharing for each bus in the IEEE 30-bus system represented as *A* can be computed with the equations below;

$$A = \frac{\text{Demand in bus-}n \text{ (Real or Reactive)}}{\text{Peak (Real or Reactive)}} \tag{10}$$

$$\text{Real power (each month and bus)} = \text{Monthly Real Power} \times A \tag{11}$$

Sampling for the 2nd bus for January;

$$0,07657 = \frac{21,7 \text{ MW}}{283,4 \text{ MW}}$$

$$19,66 \text{ MW} = 256,7 \text{ MW} \times 0,07657$$

The load curves of the monthly total real and reactive powers for the Model-1 is represented in Fig. 2 and Fig. 3;

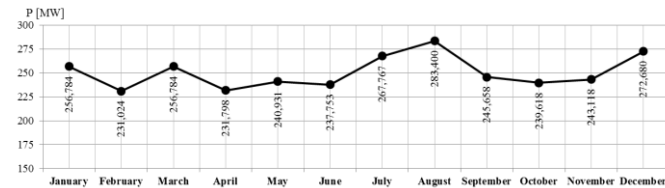


Fig.2. Monthly total real power load curve for Model-1

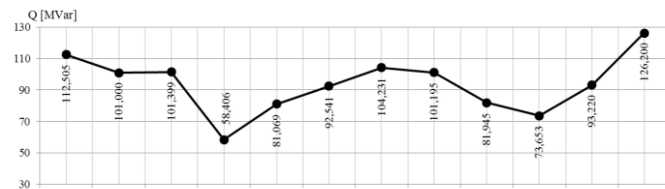


Fig.3. Monthly total reactive power load curve for Model-1.

3.2 Regulation-II

The renewable energy sources are integrated into Model-1 in the rate of 48% of total capacity by modifying the bus-5 and bus-11 as the wind power plants and bus-13 as the solar power plants in IEEE 30-bus standard test system. The single-line diagram of the modified IEEE 30-bus system for Model-2 (also for Model-3) and new generation capacities of the power plants are represented in Fig. 4 and Table 1.

TABLE I
GENERATION CAPACITIES OF THE MODEL-2 [35]

Bus No	Plant Type	Generation Capacity, [MW]
1	Thermal	99.248
2	Thermal	80.000
5	Wind	75.000
8	Thermal	20.000
11	Wind	60.000
13	Solar	50.000

After this modification, the new load curves as a dynamic OPF model are computed as similar to the Regulation-1.

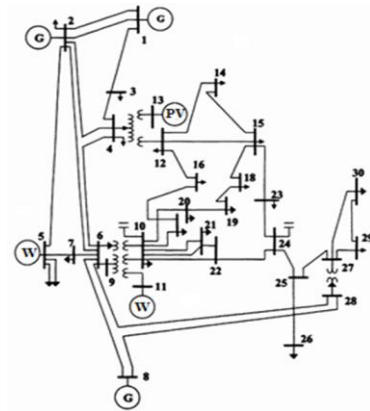


Fig.4. Modified IEEE 30-bus system for Model-2 and Model-3

3.3 Regulation-III

This regulation is realized to compose Model-3. In this regulation, dynamic and stochastic OPF models are combined with each other as DSOPF in order to examine the uncertainty of the renewable energy resources integrated to the Model-2. The stochastic OPF model is achieved by using Weibull PDF to model the monthly variations of the wind speed and the sun radiation as explained below.

3.3.1 Modelling wind speed uncertainty

To modeling wind speed uncertainty, it is assumed in accordance with the IEEE 30-bus standard test system layout that the two wind power plants at the bus-5 and bus-11 powered 75 MW and 50 MW, respectively has been installed in Amasra county of Bartın in Turkey. The chosen values of air density ($\rho = 1,211 \text{ kg/m}^3$), scale factor *k* and shape factor *c* for Amasra region and the computed values below are represented in Table 2 [36]. The gamma function is used to find the average wind speeds (V_m) for each month. Gamma function is represented in Equation (12).

$$V_m = c \cdot \Gamma\left(\frac{1}{k}\right) \tag{12}$$

TABLE II
k AND *c* COEFFICIENTS AND COMPUTED RESULTS OF WEIBULL PDF FOR EACH MONTH

Amasra Region ($\rho=1,211 \text{ kg/m}^3$)						
Months	k	c	V_m , [m/s]	f_w	F_w	Power density, [W/m ²]
January	1,48	8,63	7,8037	0,0690	0,5775	287,7522
February	1,50	8,22	7,4206	0,0735	0,5759	247,4146
March	1,54	9,81	8,8292	0,0634	0,5727	416,7502
April	1,39	7,79	7,1081	0,0714	0,5854	217,4564
May	1,40	5,56	5,0675	0,1008	0,5845	78,7951
June	1,40	6,10	5,5597	0,0919	0,5845	104,0553
July	1,30	7,41	6,8437	0,0695	0,5942	194,0831
August	1,49	6,53	5,8998	0,0919	0,5767	124,3425
September	1,82	7,11	6,3196	0,1037	0,5538	152,8187
October	1,59	8,97	8,0470	0,0717	0,5689	315,5100
November	1,63	7,16	6,4090	0,0921	0,5660	159,3960
December	1,94	9,57	8,4869	0,0820	0,5471	370,1391

The monthly Weibull PDFs of the wind speed for 0-40 m/s range can be computed by using equation (13). The monthly Weibull PDFs are depicted in Fig. 5.

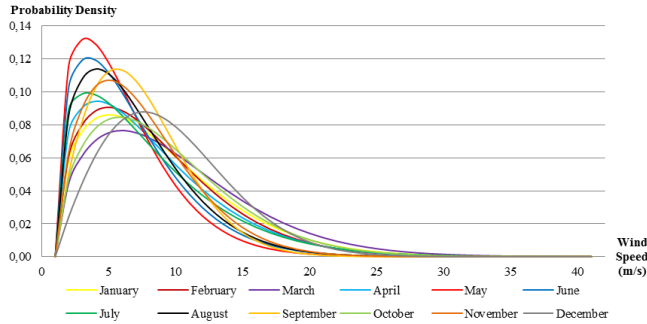


Fig.5. The monthly Weibull PDFs for Model-3

$$f_w(v) = \left(\frac{k}{c}\right) \cdot \left(\frac{v}{c}\right)^{k-1} \cdot e^{-\left(\frac{v}{c}\right)^k} \quad (13)$$

Then, the cumulative Weibull PDFs for each month which give the probability of being less than or equal to the average speed of that month is computed as below;

$$F_w(v) = 1 - e^{-\left(\frac{v}{c}\right)^k} \quad (14)$$

ENERCON E-115 E-2 model 3,200 kW wind turbine is selected for this study. The cut-in speed v_i , rated speed v_r and cut-out speed v_o for the turbine are given in Table 3. The turbine output power according to the speeds are calculated and presented at the same table.

$$p = \begin{cases} 0, & v \leq v_i, v > v_o \\ p_r \left(\frac{v-v_i}{v_r-v_i}\right), & v_i \leq v \leq v_r \\ p_r, & v_r \leq v \leq v_o \end{cases} \quad (15)$$

TABLE III
THE CUT-IN SPEED V_i , RATED SPEED V_r , AND CUT-OUT SPEED V_o FOR THE TURBINE

Months	v_r [m/s]	v_i [m/s]	v_r [m/s]	v_o [m/s]	P_{75MW} [MW]	P_{60MW} [MW]
January	7,8037	2,0000	11,0000	25,0000	48,3643	38,6914
February	7,4206	2,0000	11,0000	25,0000	45,1714	36,1371
March	8,8292	2,0000	11,0000	25,0000	56,9099	45,5279
April	7,1081	2,0000	11,0000	25,0000	42,5674	34,0539
May	5,0675	2,0000	11,0000	25,0000	25,5626	20,4501
June	5,5597	2,0000	11,0000	25,0000	29,6640	23,7312
July	6,8437	2,0000	11,0000	25,0000	40,3642	32,2914
August	5,8998	2,0000	11,0000	25,0000	32,4981	25,9985
September	6,3196	2,0000	11,0000	25,0000	35,9964	28,7971
October	8,0470	2,0000	11,0000	25,0000	50,3915	40,3132
November	6,4090	2,0000	11,0000	25,0000	36,7414	29,3931
December	8,4869	2,0000	11,0000	25,0000	54,0577	43,2462

3.3.2 Modelling solar radiation uncertainty

To modeling solar radiation uncertainty, it is assumed in accordance with the IEEE 30-bus standard test system layout that the solar power plants at the bus-13 powered 50 MW has

been installed in Ankara region in Turkey. The model of the solar power plant can be obtained with the direct normal radiation values calculated for this region. For this region, DNI (Direct Normal Irradiation) values depicted in Fig. 6 which are directly calculated instead of the k and c parameters are used [36].

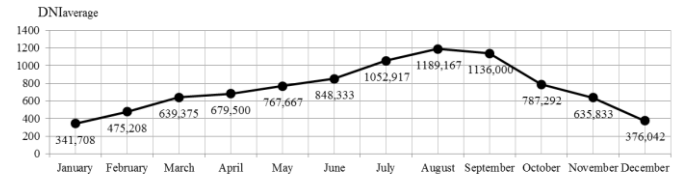


Fig.6. Average monthly DNI values for Ankara region [34]

The AXITECAC 320P/156-72S model solar panels are selected for this study. The PV panel output power according to the amount of solar radiation is calculated as below [34]. These values are shown in Table 4 for each month.

$$P_{PV}(G) = \begin{cases} P_{sr} \left(\frac{G^2}{G_{std} \cdot R_c}\right) & 0 < G < R_c \\ P_{sr} \left(\frac{G}{G_{std}}\right) & G > R_c \end{cases} \quad (16)$$

Where:

G - is solar irradiance forecast

G_{std} - is standard irradiation [1000 W/m²]

R_c - is a certain irradiation point set to 150 W/m²

P_{sr} - is rated equivalent power output of the PV system

TABLE IV
MONTHLY FRACTION OF DNI VALUES FOR ANKARA REGION

Ankara	G_r [W/m ²]	G_{std} [W/m ²]	R_c [W/m ²]	P_{50MW} [MW]
January	341,7083	1000	150	17,0854
February	475,2083	1000	150	23,7604
March	639,3750	1000	150	31,9688
April	679,5000	1000	150	33,9750
May	767,6667	1000	150	38,3833
June	848,3333	1000	150	42,4167
July	1052,9167	1000	150	52,6458
August	1189,1667	1000	150	59,4583
September	1136,0000	1000	150	56,8000
October	787,2917	1000	150	39,3646
November	635,8333	1000	150	31,7917
December	376,0417	1000	150	18,8021

IV. PROPOSED OPF STUDIES

To examine the uncertainty effect of the renewable energy sources added to the IEEE 30-bus system in according to regulations considered before, three cases are performed by using model-1, model-2 and model-3. All OPF problems have been solved by Newton-Raphson solution method on *MATLAB* environment.

4.1 Case-I:

In this case, the dynamic OPF model is applied to the IEEE 30-bus test system and only the monthly real and reactive powers

are changed in each bus. All of the plants are considered thermal power plants.

TABLE V
THE RESULTS OF CASE-I

	Total Active Power, [MW]	Total Reactive Power, [MVAR]	Cost, [\$/h]	Standard Deviations of the Voltage Magnitudes	Standard Deviations of the Phase Angles
January	264,705	74,061	707,06	0,0165	2,8423
February	237,329	55,944	618,91	0,0157	2,5157
March	264,655	62,518	706,86	0,0157	2,8459
April	238,057	14,541	620,90	0,0150	2,5546
May	247,794	37,770	651,80	0,0144	2,6623
June	244,489	49,137	641,32	0,0157	2,6120
July	276,258	68,104	745,72	0,0165	2,9705
August	292,744	68,673	802,05	0,0166	3,1368
September	252,797	39,803	667,93	0,0145	2,7230
October	246,397	29,969	647,30	0,0146	2,6509
November	250,189	51,146	659,56	0,0158	3,0806
December	281,535	91,767	763,63	0,0176	3,0154
	3096,95 (total)	643,43 (total)	8233,04 (total)	0,0157 (average)	2,8000 (average)

The results obtained by using model-1 are represented in Table 5. The fuel costs, the voltage magnitudes and the phase angles of the voltages are computed monthly for each bus with dynamic OPF model. However, the voltage magnitudes and their phase angles for each month are represented by computing their standard deviations. At the end of the table, the average values are presented. On the other hand, these values are represented graphically in Fig. 7, 8 and 9.

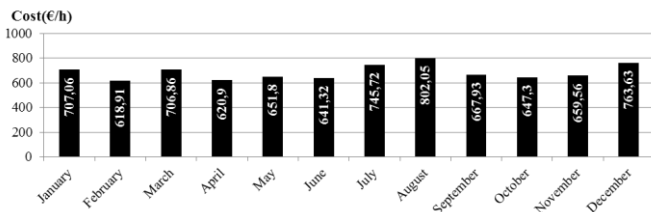


Fig.7. Monthly cost values for case-I

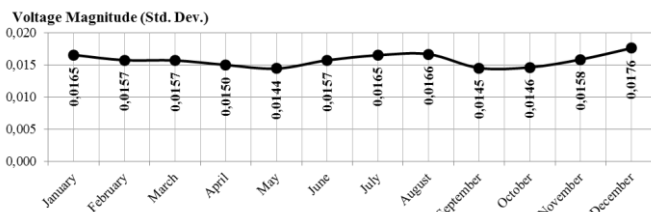


Fig.8. Monthly standard derivations of the voltage magnitudes for case-I

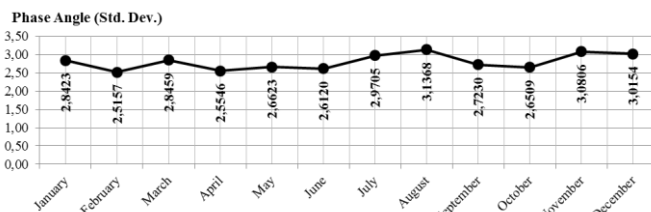


Fig.9. Monthly standard derivations of the voltage angles for case-I

4.2 Case-II:

In this case, the dynamic OPF model is applied to the IEEE 30-bus test system with the renewable energy sources which have the constant outputs. In this model, bus-5 and bus-1 considered wind power plants whose capacities are 75 MW and 60 MW, respectively. Also, bus-13 is considered 50 MW solar power plant. The other generation buses are considered same as the standard IEEE 30-bus test system. The results obtained by using model-2 are represented in Table 6.

The results are computed monthly for each bus with dynamic OPF model which have renewable power plants having constant power outputs. The coefficients of the quadratic cost function presented in equation (4) are taken zero for the renewable energy sources at this case study since there are no or close to zero fuel costs for renewable power plants in actual in steady-state. For this reason, the costs are computed quite small than the standard ones. The voltage magnitudes and their phase angles for each month are also represented with standard deviations. At the end of the table, the average values are presented. The graphics of these values are depicted in Fig. 10, 11 and 12.

TABLE VI
THE RESULTS OF CASE-II

Months	Total Active Power, [MW]	Total Reactive Power, [MVAR]	Cost, [\$/h]	Standard Deviations of The Voltage Magnitudes	Standard Deviations of The Phase Angles
January	258,900	43,282	170,45	0,0169	2,3862
February	232,687	38,735	111,97	0,0160	2,2954
March	258,846	36,515	170,33	0,0164	2,3861
April	233,233	34,088	113,14	0,0127	2,3365
May	242,556	35,622	133,39	0,0134	2,3535
June	239,352	38,179	126,35	0,0146	2,3099
July	270,123	37,734	197,07	0,0168	2,4440
August	286,258	35,373	236,98	0,0170	2,5409
September	247,350	31,234	144,05	0,0146	2,3371
October	241,213	31,387	130,43	0,0135	2,3497
November	244,801	38,089	138,36	0,0147	2,3276
December	275,275	50,534	209,60	0,0180	2,4719
	3030,59 (total)	450,77 (total)	1882,12 (total)	0,0153 (average)	2,3782 (average)

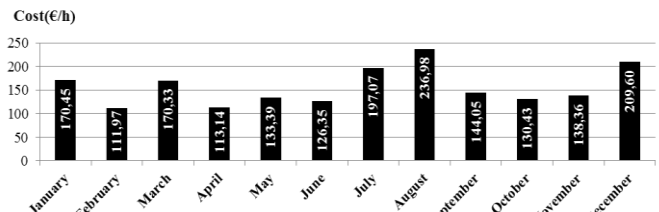


Fig.10. Monthly cost values for case-II

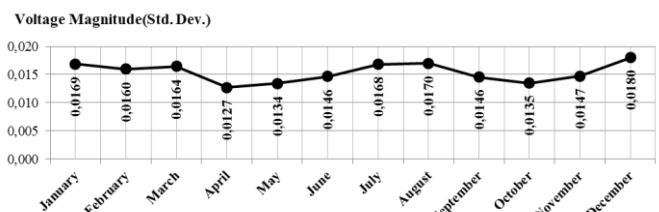


Fig.11. Monthly standard derivations of the voltage magnitudes for case-II

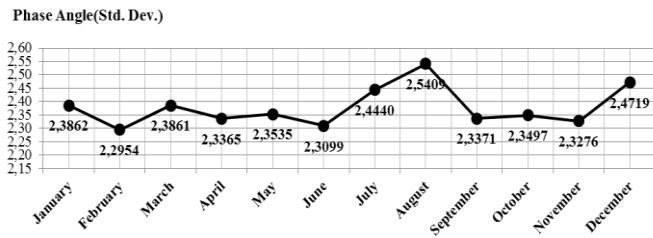


Fig.12. Monthly standard derivations of the voltage angles for case-II

4.3 Case-III:

In this case, the dynamic-stochastic OPF model is applied. In this model, all renewable energy sources have uncertainties modeled with Weibull PDFs for each month. The other generation buses are considered same as the standard IEEE 30-bus test system. The results obtained from model-3 are represented in Table 7.

The results are computed monthly for each bus with dynamic-stochastic OPF model which have renewable power plants having uncertainties. The coefficients of the quadratic cost function are also taken zero for the renewable energy sources at this case study since there are no or close to zero fuel costs for renewable power plants in actual in steady-state. But, the costs computed are closer to the real values. The graphic results are also depicted in Fig. 13, 14 and 15.

TABLE VII
THE RESULTS OF CASE-III

Months	Total Active Power, [MW]	Total Reactive Power, [MVAR]	Cost, [\$/h]	Standard Deviations of The Voltage Magnitudes	Standard Deviations of The Phase Angles
January	261,531	30,324	391,00	0,0166	2,2085
February	234,334	30,590	310,88	0,0158	2,0345
March	260,239	32,257	309,64	0,0162	2,2221
April	234,870	10,040	297,27	0,0148	1,9913
May	246,309	17,278	404,46	0,0158	2,1926
June	242,333	23,650	359,31	0,0158	2,0884
July	272,714	31,995	361,85	0,0168	2,3395
August	290,196	30,820	435,72	0,0171	2,3453
September	249,556	23,018	307,25	0,0145	2,1770
October	242,360	20,041	265,36	0,0146	2,0449
November	247,604	25,265	368,38	0,0159	2,1500
December	277,794	48,549	403,73	0,0176	2,2719
	3059,84 (total)	323,83 (total)	4214,85 (total)	0,0159 (average)	2,1721 (average)

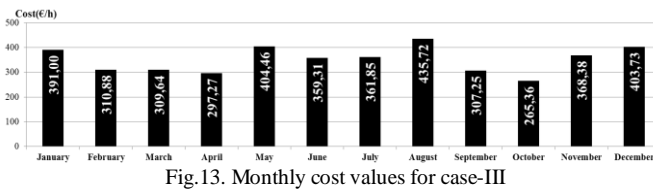


Fig.13. Monthly cost values for case-III

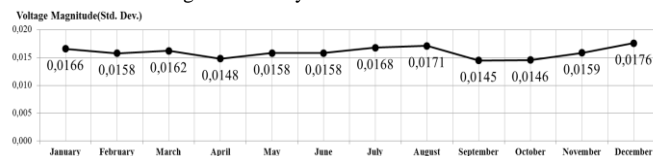


Fig.14. Monthly standard derivations of the voltage magnitudes for case-III

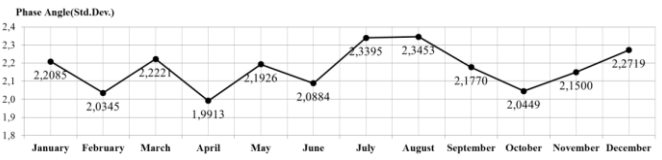


Fig.15. Monthly standard derivations of the voltage angles for case-III

V. RESULTS AND DISCUSSION

At the end of the studies, the monthly standard deviations of the voltage magnitudes are specified in Fig. 16. It is observed from the figure that while the voltage magnitudes relatively decrease for some months of Model-2, the values computed at Model-3 is almost the same as the Model-1 which is assumed as a reference. It can be seen that these decreases in Model-2 are caused from inadequacy of the reactive powers supplied to the network by the entire power plants at April and October as observed from Table 6, since the renewable power plants have been taken constant capacities in this model.

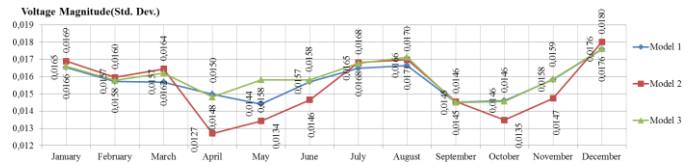


Fig.16. Monthly standard derivations of the voltage magnitudes case-I-II-III

On the other hand, the results are obtained relatively better in Model-3 according to the Model-1 for some months such as March, May and August, since the reactive power support of the power plants to the consumers increase in these months as seen from the tables as well.

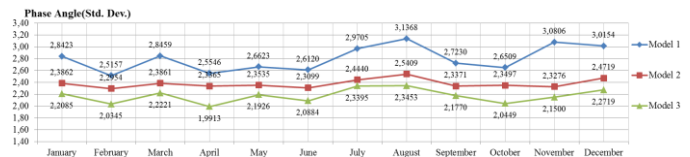


Fig.17. Monthly standard derivations of the voltage angles for case-I-II-III

Also, it is seen from the Fig. 17 that the phase angles of the bus voltages decrease in general and they have been more stable when the renewable power plants are integrated to the power system. When the monthly costs are examined, it is normally seen that the costs obtained from Model-1 which involved only IEEE 30-bus system are bigger than the other models which include renewable energy sources. Its maximum and minimum values are computed as 802.05 \$/h and 618.91 \$/h, respectively. At Model-2, the maximum and minimum values are computed as 236.98 \$/h and 111.97 \$/h, respectively. They are relatively very small compared to the values obtained from Model-1, since the α, β, γ coefficients of the cost function are assumed zero for renewable energy sources. These results are not realistic, but they are computed in order to be able to notice the change in Model-3 in this study. They directly follow the load curve, as similar to the Model-1. On the other hand, when the uncertainties are added to the renewable energy sources by using Weibull PDFs in Model-3, the generation costs are obtained more realistic. At this study, their maximum and minimum values are computed as 435.72 \$/h and 264.36 \$/h,

respectively. From these results summarized in Table 8, it can be clearly seen that the electric energy generation costs are decreased almost in a half, although both the total active power generation is nearly the same and the voltage and the phase angles are keep their stabilities. In addition, it is provided that the reactive power generation also decreases almost in a half as well in this circumstance.

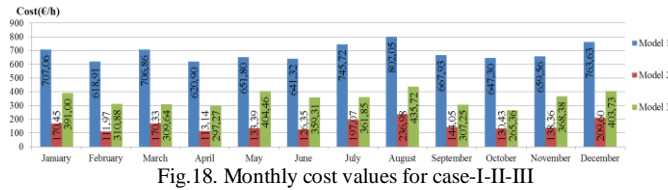


Fig.18. Monthly cost values for case-I-II-III

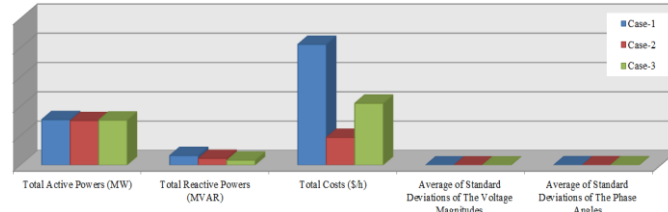


Fig.19. Graphical comparison of the entire results

As a result, the proposed DSOPF analysis which takes into account the uncertainty effects of renewable energy resources as well, clearly shows with the example study that the contribution of integrating the renewable power plants into the power system which includes classic thermal power plants are in important level.

TABLE VIII
COMPARISON OF THE RESULTS OF CASE-I-II-III

	Total Active Powers, [MW]	Total Reactive Powers, [MVAR]	Total Costs, [\$ /h]	Average of Standard Deviations of the Voltage Magnitudes	Average of Standard Deviations of the Phase Angles
Case-1	3096,95	643,43	8233,04	0,0157	2,8000
Case-2	3030,59	450,77	1882,12	0,0153	2,3782
Case-3	3059,84	323,83	4214,85	0,0159	2,1721

VI. CONCLUSION

The effect of uncertain renewable energy sources integrated into a specific area of Turkey electricity power system on the static voltage stability is simulated by using DSOPF analysis in this study. DSOPF analyses combined Weibull PDF throughout a year is chosen in order to taking into account uncertainty effect of the renewable energy resources. Also, the IEEE 30-bus system is adapted with the method proposed in the study to the Turkish electricity system by using 2015 Turkey real and reactive load curves, as different from the literature. The analyses are performed on three models for comparison with each other. At the end of the proposed study, it is observed that the integration of realistic renewable energy sources with uncertainty into the Turkey electricity power system decreases approximately 50% both the yearly total generation cost and the reactive power generation, without changing the current active power generation. In this condition, it can be said that the static voltage stability of the power system is became more stable due to increase the reactive power margin.

REFERENCES

- [1] The Economist, “European Utilities, How to Lose Half A Trillion Euros”, October 15th 2013, <https://www.economist.com/news/briefing/21587782-europes-electricity-providers-face-existential-threat-how-lose-half-trillion-euros>
- [2] IEA Renewables 2017, London, October 4th 2017, <https://www.iea.org/media/publications/mtrmr/Renewables2017LaunchPresentation.pdf>
- [3] REN21 Renewable 2017 Global Status Report, http://www.ren21.net/wp-content/uploads/2017/06/17-8399_GSR_2017_Full_Report_0621_Opt.pdfology, January 2013, pp.1-11.
- [4] Electromagnetic Yenilenebilir Enerji Genel Müdürlüğü (General Directorate Of Renewable Energy), <http://www.eie.gov.tr/anasyafa2.aspx>.
- [5] J. Liang, G.K. Venayagamoorthy, R.G. Harley, “Wide-area measurement based dynamic stochastic optimal power flow control for smart grids with high variability and uncertainty,” IEEE Transactions on Smart Grid, vol.3, no.1, pp.59–69, 2012.
- [6] S. Gill, I. Kockar, G.W. Ault, “Dynamic Optimal Power Flow For Active Distribution Networks”, IEEE Transactions On Power Apparatus And Systems, vol.29P, issue.1, pp.121-131, 2014.
- [7] C. Wei, Y. Fu, Z. Li, Y. Jiang, “Optimal DG Penetration Rate Planning Based On S-OPF In Active Distribution Network,” *Neurocomputing*, vol.174, pp.514–521, 2016.
- [8] G. Sun, Y. Li, S. Chen, Z. Wei, S. Chen, H. Zang, “Dynamic Stochastic Optimal Power Flow Of Wind Power And The Electric Vehicle Integrated Power System Considering Temporal Spatial Characteristics”, *Journal of Renewable and Sustainable Energy*, vol.8, issue.5, 2016.
- [9] W. Bai, D. Lee, K. Lee, “Stochastic Dynamic Optimal Power Flow Integrated with Wind Energy Using Generalized Dynamic Factor Model”, *IFAC-Papers On-Line*, vol.49, issue.27, pp.129-134, 2016.
- [10] W. Bai, “Stochastic Dynamic Optimal Power Flow Under The Variability Of Renewable Energy With Modern Heuristic Optimization Techniques”, PhD. Thesis, Baylor University, Waco, Texas, 2017.
- [11] J. Carpentier, “Contribution a l’etude du dispatching economique”, *Bulletin de la Societe Francaise des Electriciens*, vol.3, iss.1, pp.431-447, 1962.
- [12] B. Ghaddar, J. Marecek, M. Mevissen, “Optimal Power Flow As A Polynomial Optimization Problem”, *IEEE Transactions on Power Systems*, vol.31, issue.1, pp.539-546, 2016.
- [13] J. Lin, V.O. Li, K.C. Leung, A.Y. Lam, “Optimal Power Flow With Power Flow Routers”, *IEEE Transactions on Power Systems*, vol.32, issue.1, pp.531-543, 2017.
- [14] S. Frank, I. Stepanavice, S. Rebennack, “Optimal Power Flow: A Bibliographic Survey I”, *Energy Systems*, vol.3, issue.3, pp.221-258, 2012.
- [15] K.C. Almeida, A. Kocholik, “Solving Ill-Posed Optimal Power Flow Problems Via Fritz-John Optimality Conditions”, *IEEE Transactions on Power Systems*, vol.31, issue.6, pp.4913-4922, 2016.
- [16] A.D. Chandekar, D. Subroto, “A Review on Optimal Power Flow Solutions under Variable Load”, *International Journal of Advanced Research in Electrical, Electronics and Instrumentation Engineering*, vol.4, issue.1, 2015.
- [17] A.M. Shaheen, R.A. El-Sehiemy, S.M. Farrag, “Solving Multi Objective Optimal Power Flow Problem Via Forced Initialised Differential Evolution Algorithm”, *IET Generation, Transmission & Distribution*, vol.10, issue.7, pp.1634-1647, 2016.
- [18] T. Niknam, M.R. Narimani, M. Jabbari, “Dynamic Optimal Power Flow Using Hybrid Particle Swarm Optimization And Simulated Annealing”, *International Transactions on Electrical Energy Systems*, vol.23, issue.7, pp.975-1001, 2013.
- [19] Y. Xu, J. Ma, Z.Y. Dong, D.J. Hill, “Robust Transient Stability-Constrained Optimal Power Flow With Uncertain Dynamic Loads”, *IEEE Transactions on Smart Grid*, vol.8, issue.4, pp.1911-1921, 2017.
- [20] Y. Xu, Z.Y. Dong, Z. Xu, R. Zhang, K.P. Wong, “Power System Transient Stability-Constrained Optimal Power Flow: A Comprehensive Review”, In *IEEE Power and Energy Society General Meeting*, pp.1-7, 2012.
- [21] M.M. Bhaskar, M. Srinivas, M. Sydulu, “Security Constraint Optimal Power Flow (SCOPF)-A Comprehensive Survey”, *International Journal of Computer Applications*, vol.11, issue.6, pp.42-52, 2010.

- [22] M. Lubin, Y. Dvorkin, "A Robust Approach to Chance Constrained Optimal Power Flow with Renewable Generation", IEEE Transactions on Power Systems, vol.31, issue.5, pp.3840-3849, 2016.
- [23] A. Vaccaro, C.A. Cañizares, "An Affine Arithmetic-Based Framework For Uncertain Power Flow And Optimal Power Flow Studies", IEEE Transactions on Power Systems, vol.32, issue.1, pp.274-288, 2017.
- [24] M. Bazrafshan, N. Gatsis, "Decentralized Stochastic Optimal Power Flow In Radial Networks With Distributed Generation", IEEE Transactions on Smart Grid, vol.8, issue.2, pp.787-801, 2017.
- [25] J. Gong, D. Xie, C. Jiang, Y. Zhang, "A New Solution For Stochastic Optimal Power Flow: Combining Limit Relaxation With Iterative Learning Control", Journal of Electrical Engineering and Technology, vol.9, issue.1, pp.80-89, 2014.
- [26] H. Zhang, P. Li, "Probabilistic Analysis For Optimal Power Flow Under Uncertainty", IET Generation, Transmission & Distribution, vol.4, issue.5, pp.553-561, 2010.
- [27] A. Schellenberg, W. Rosehart, J. Aguado, "Cumulant-Based Probabilistic Optimal Power Flow (P-OPF) With Gaussian And Gamma Distributions", IEEE Transactions on Power Systems, vol.20, issue.2, pp.773-781, 2005.
- [28] G. Verbic, C.A. Canizares, "Probabilistic Optimal Power Flow In Electricity Markets Based On A Two-Point Estimate Method", IEEE transactions on Power Systems, vol.21, issue.4, pp.1883-1893, 2006.
- [29] D. Ke, C.Y. Chung, Y. Sun, "A Novel Probabilistic Optimal Power Flow Model With Uncertain Wind Power Generation Described By Customized Gaussian Mixture Model", IEEE Transactions on Sustainable Energy, vol.7, issue.1, pp.200-212, 2016.
- [30] M. Ou, Y. Xue, X.P. Zhang, "Iterative DC Optimal Power Flow Considering Transmission Network Loss", Electric Power Components and Systems, vol.44, issue.9, pp.955-965, 2016.
- [31] T. Akbari, M.T. Bina, "Linear Approximated Formulation Of AC Optimal Power Flow Using Binary Discretisation", IET Generation, Transmission & Distribution, vol.10, issue.5, pp.1117-1123, 2016.
- [32] W. Feng, A. Le Tuan, L.B. Tjemberg, A. Mannikoff, A. Bergman, "A New Approach For Benefit Evaluation Of Multiterminal VSC-HVDC Using A Proposed Mixed AC/DC Optimal Power Flow", IEEE Transactions on Power Delivery, vol.29, issue.1, pp.432-443, 2014.
- [33] www.washington.edu, https://www2.ee.washington.edu/research/pstca/pf30/pg_tca30bus.htm.
- [34] <https://www.teias.gov.tr/yayinlar-raporlar/sector-raporlari/isletme-faaliyetleri-raporlari/2015-yili-isletme-faaliyetleri-raporu>.
- [35] P.P. Biswas, P.N. Suganthan, G.A.J. Amaratunga, "Optimal power flow solutions incorporating stochastic wind and solar Power", Energy Conversion and Management, vol.148, pp.1994-1207, 2017.
- [36] F. Szek, "Trkiye Rzgr Enerji Potansiyelinin Belirlenmesi," İstanbul, 2007.

BIOGRAPHIES



BASAR BAYDAR graduated from Department of Electrical and Electronics Engineering, Osmangazi University, Eskisehir, Turkey in 2014 and working as an Electrical Engineer at Baskent Electrical Distribution Company, EnerjiSA, Ankara, Turkey. He is currently a student of M.Sc. degree in Electrical and Electronics Engineering Department, Gazi

University, Ankara, Turkey. His main research interests and subjects are high voltage engineering, power systems, smart grids and renewable energy sources.



HALUK GOZDE received the B.Sc. degree in Electrical and Electronics Engineering from Karadeniz Technical University, Trabzon, Turkey, in 1997, and the M.Sc. and the Ph.D. degrees in Electrical and Electronics Engineering from Gazi University, Ankara, Turkey, in 2004 and 2010, respectively. Then, he is an Assoc.Prof. of the electrical and

electronics engineering in National Defense University since 2016. His main research area consists of power system dynamics and control, artificial intelligence-based control methods, and swarm intelligence-based optimization algorithms.



M. CENGİZ TAPLAMACIOĞLU graduated from Department of Electrical and Electronics Engineering, Gazi University, Ankara, Turkey. He received the degrees of M.S. degree in Industrial Engineering from Gazi University in 1985 and in Electrical and Electronics Engineering from Middle East Technical University

and received the Ph.D. degree in Electrical, Electronics and System Engineering from University of Wales (Cardiff, UK). He is a Professor of the Electrical and Electronics Engineering since 2000 and the Chairman of the Department of Electrical and Electronics Engineering in Gazi University between 2001-2012. His research interests and subjects are high voltage engineering, corona discharge and modeling, electrical field computation, measurement and modeling techniques, optical HV measurement techniques, power systems control and protection, and lighting techniques.

A Convolutional Neural Network Application for Predicting the Locating of Squamous Cell Carcinoma in the Lung

H.S. Nogay, and T.C. Akinci

Abstract—Squamous cell carcinoma, one of the most common types of lung cancer types, usually occurs in the middle, right or left bronchi. Squamous cell carcinoma can be easily detected by imaging methods to determine the location within the lung. However, rarely the location of some tumor types cannot be determined. In this case, it may be delayed to obtain the results of the assay such as biopsy. This possible delay also means delayed diagnosis and delayed start of treatment. In order to solve this problem, it is possible to perform applications with machine learning methods. In this study, convolutional neural networks method was used to determine the location of cancerous tumor in squamous cell carcinoma of lung. With the designed convolutional neural network model, squamous cell carcinoma tumor location in lung cancer was estimated with an accuracy rate close to 100%.


Index Terms—Convolutional neural networks, squamous cell carcinoma, classification, estimation, accuracy rate.


I. INTRODUCTION

WHILE lung cancer is a rare disease at the beginning of the 20th century, the frequency has increased steadily in parallel with the increase in smoking habits and has become the most common type of cancer in the world [1]. According to the World Health Organization (WHO) report, lung cancer is the leading cause of death among males and the second type of cancer among females all over the world [2]. Squamous cell lung cancer, also called lung squamous cell carcinoma, accounts for about 30% of all lung cancers [3]. There are many treatment options for people diagnosed with squamous cell lung cancer, and doctors are constantly working to increase and improve these types of treatments. Squamous cell lung cancer is a type of non-small cell lung cancer. Squamous cell carcinoma starts as squamous cells that look like fish scales when viewed under a microscope. This cancer, which runs along the inside of the airways in the lungs, uses the most air channels to progress. Squamous cells in the tissue that make up the skin surface are also found on the surface of the body's organs and inside the digestive tract. Squamous cell carcinoma originating in the lungs is thought to be lung cancer.

Squamous cell lung tumors usually begin in the middle of the lung or in one of the main airways (left or right bronchus) [3, 4]. The location of the tumor may affect the appearance of symptoms such as coughing, shortness of breath, chest pain and blood in the sputum. If the tumor is enlarged, a chest radiograph or computerized tomography scan may detect a space in the lung. This space is a gas or fluid-filled cavity in the tumor mass or nodule and is a classic sign of squamous cell lung cancer. Squamous cell lung cancer can spread to multiple sites such as the brain, spine, other bones, the adrenal glands, and the liver. Smoking affects this type of cancer more strongly than any other large-cell lung cancer. Other risk factors for squamous cell lung cancer include age, hereditary diseases, environmental pollution, mineral and metal dust, exposure to asbestos or radon. Positive results may be observed with appropriate treatment methods, although this type of cancer is sometimes hardly noticed by occult development [5-7]. Pathologically, lung cancer can be divided into 4 main groups; a) squamous cell carcinoma, b) large cell carcinoma, c) adenocarcinoma, d) small adenocarcinoma. Squamous cell carcinoma in 40% - 60% of males is more common in the middle and advanced age group. The main diagnostic methods of lung cancer are; a) CT (Computerized Tomography), b) Endoscopic Ultrasonography, c) Bronchoscopy, Thoracoscopy, Dermoscopy. d) Pulmonary Radiography e) Positron Emission Tomography (PET) f) Magnetic Resonance Imaging. The main treatment modalities are surgical treatment, radiotherapy, chemotherapy and cryotherapy. Squamous cell carcinoma shows different symptoms according to its tumor location. Identification of tumor location is of great importance in early diagnosis of the disease. The region of the lung where the tumor is located is an important piece of information to be used for the treatment process. The location of the tumor is immediately revealed by imaging techniques. In some cases, however, the tumor location may not be detected by imaging techniques. This leads to delays for biopsy and the later start of treatment [7-13].

Machine learning-based prediction methods have been used effectively in recent years for different purposes in cancer types [14-17]. In this study, convolutional neural network (CNN) model, which is the most popular method of machine learning approaches in recent years, is designed. Detection of tumor location in squamous cell carcinoma lung cancer is the main goal of the study. In the first section of the study, basic information on entry and lung cancer was included. In the second section, data set and materials used in the study were mentioned. In the third chapter, the design of the convolutional neural networks used in the study is briefly explained. In the fourth section, the estimation results obtained from the CNN

H.S. NOGAY, works in University of Kayseri, Kayseri, Turkey, (e-mail: nogay@erciyes.edu.tr). 

T.C. AKINCI, is with Department of Electrical Engineering, Istanbul Technical University, Istanbul, Turkey, (e-mail: akincitc@itu.edu.tr). 

Manuscript received July 9, 2018; accepted June 28, 2018.
DOI: 10.17694/bajece.455132

model are presented. In the fifth chapter, which is the last chapter, the results are evaluated.

II. MATERIALS

The data set used in the study was obtained from the website of The Cancer Imaging Archive (TCIA) [18,19]. The actual size of the image data in the data set is 512 x 512. All image data used in this study actually consist of 3-channel data. In order to train the CNN model in shorter time, all image data in the data set is reduced to 84x84 and single channel gray scale. According to the regions of the squamous cell carcinoma tumor dataset, a data set consisting of a total of 300 image data, 60 data for five regions, was used. Figure 1 shows a sample image at the actual size in the dataset.

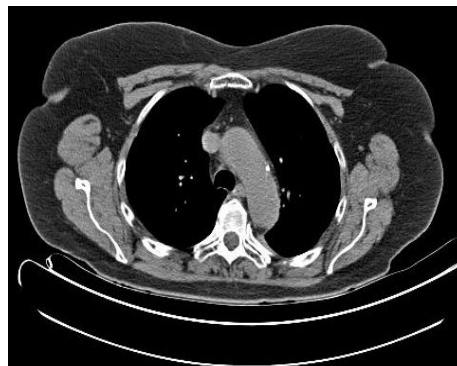


Fig. 1. Lung squamous cell carcinoma sample image

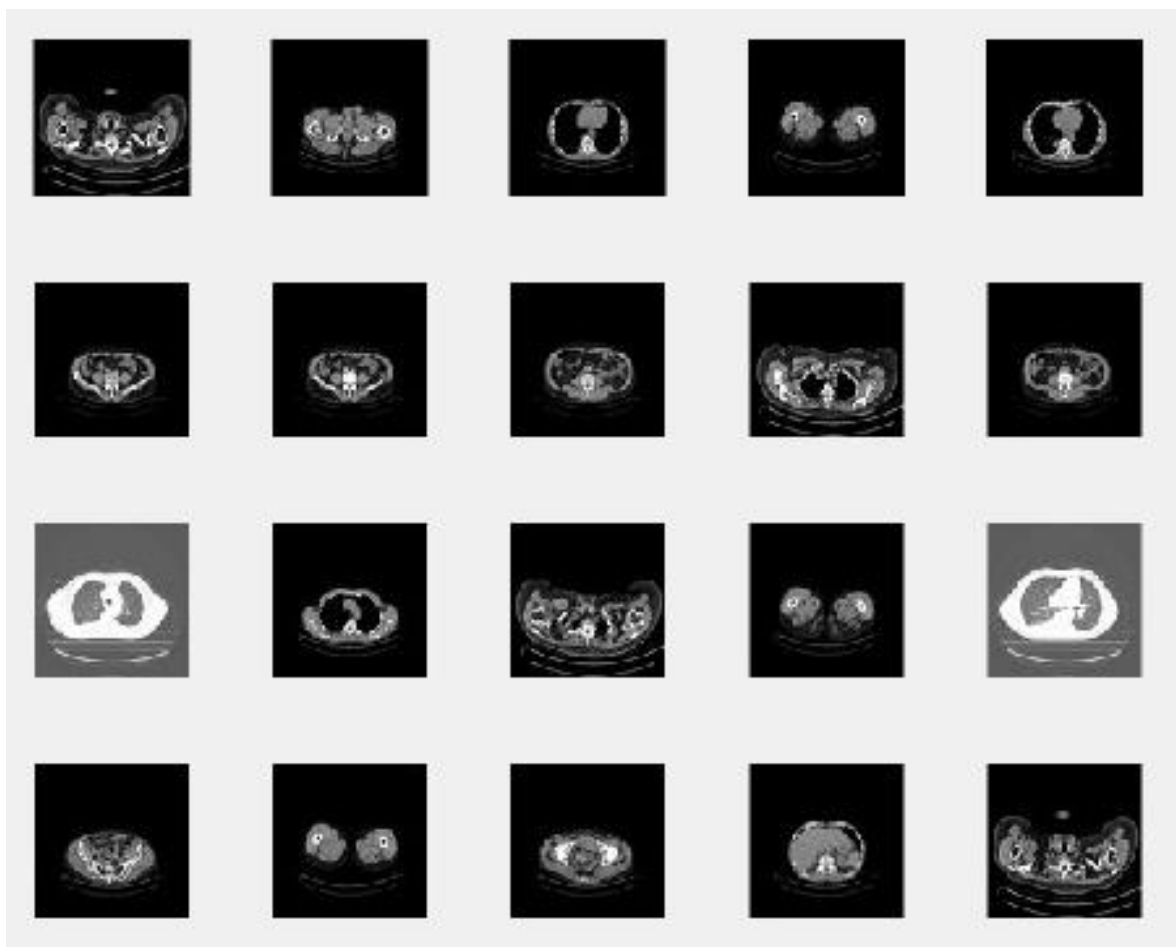


Fig. 2. Example of data set available for CNN

Figure 2 shows a sample data set consisting of 20 randomly selected images after reducing the image data to a usable size. The abbreviations and numbering used for the 5 regions of the lung where squamous cell carcinoma is present in the data set used in the study are shown in Table 1.

TABLE.1 SQUAMOUS CELL CARCINOMA LUNG LOCATION AND NUMBERING

Location	Abbreviation	Numbering
Left Lower Lobe	LLL	1
Left Upper Lobe	LUL	2
Right Upper Lobe	RUL	3
Right Lower Lobe	RLL	4
Right Middle Lobe	RML	5

III. METHODOLOGY

For the input layer of the CNN model, each image data is used in the form of a matrix form. If a randomly selected image data from the data set is redrawn by contouring the digitized matrix form, Figure 3 is obtained. In Figure 3, the data set for the input layer shows a contour of a randomly selected image data in the matrix form. The convolutional neural network designed and applied in the study is shown in figure 4. The CNN model shown in Figure 4 includes the process after the actual image data is reduced to 84x84 pixels and is mono-channelized.

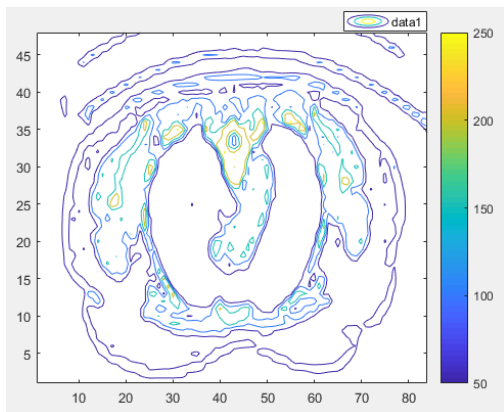


Fig. 3. Contour plot of a randomly selected sample image

The designed CNN model consists of the input layer, the convolution layer, the relu, the maxpooling layer, the fully connected layer and the softmax, respectively. As mentioned earlier, image data is used at the input layer. For the next layer, convoluted layer, 20 filters of 5x5 are used. After this filtration process, normalization with Relu transfer function is performed. In the Maxpooling layer, a 2x2 filter was used, shifted by 2 frames. The next processing layer is the ‘fully connected layer’ to which all neurons are connected. Classification is also performed with the last layer, the softmax layer.

In the study, 15 of 60 data used for each region were tested and the rest was used for training purposes. In this case a total of 75 data were used for the test and the remaining 225 data were used for the training of the model. The initial learning rate for the designed CNN model was accepted as 0.00001. 1000 is selected as the maximum epoch for training and testing in the study. The reason for choosing a very high Epoch number is to be able to achieve high accuracy.

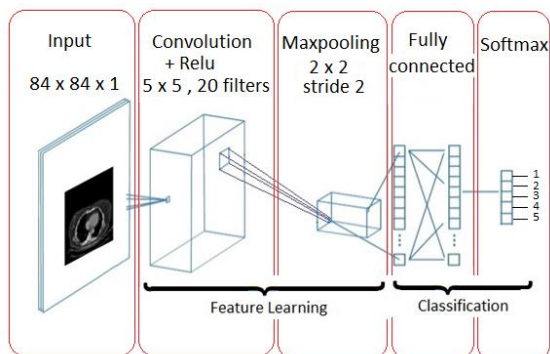


Fig. 4. Architecture of the designed CNN model

IV. RESULTS

With the training of the designed CNN model, it is estimated which region of the lung of the squamous cell carcinoma tumor is located. The accuracy of the model training and the results obtained for each 50 iterations are given in Table 2.

TABLE 2. THE EXTRACTED FEATURES

Iteration	Epoch	Time elapsed (Second)	Mini-Batch Loss	Mini - Batch Accuracy (%)	Base Learning Rate
1	1	0.16	5.7198	18.67	1.00e-05
50	50	6.22	0.0501	99.9499	1.00e-05
100	100	12.15	0.0179	99.9821	1.00e-05
150	150	18.07	0.012	99.988	1.00e-05
200	200	23.63	0.0091	99.9909	1.00e-05
250	250	29.18	0.0073	99.9927	1.00e-05
300	300	34.72	0.0061	99.9939	1.00e-05
350	350	40.3	0.0052	99.9948	1.00e-05
400	400	45.93	0.0045	99.9955	1.00e-05
450	450	51.63	0.004	99.996	1.00e-05
500	500	57.26	0.0036	99.9964	1.00e-05
550	550	62.92	0.0033	99.9967	1.00e-05
600	600	68.63	0.003	99.997	1.00e-05
650	650	74.34	0.0027	99.9973	1.00e-05
700	700	79.97	0.0025	99.9975	1.00e-05
750	750	85.7	0.0024	99.9976	1.00e-05
800	800	91.42	0.0022	99.9978	1.00e-05
850	850	97.13	0.0021	99.9979	1.00e-05
900	900	102.87	0.0019	99.9981	1.00e-05
950	950	108.6	0.0018	99.9982	1.00e-05
1000	1000	114.45	0.0017	99.9983	1.00e-05

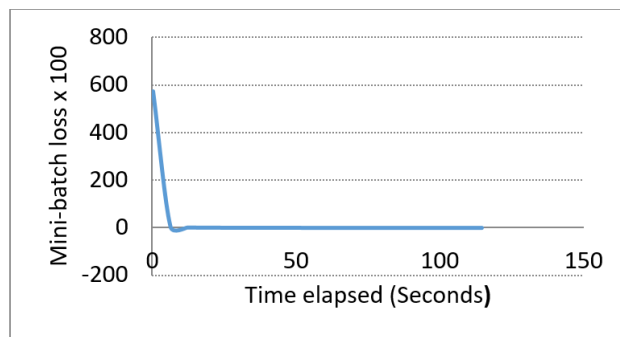


Fig. 5. The loss curve for the CNN model in the training process

At the end of each 50 epochs in the CNN model, the smallest loss ratio obtained can be viewed from the graph covering all epochs in figure 5, which are obtained according to the values given in table 2. If this graph is to be examined more clearly, the graph of Figure 6 is obtained by reducing the maximum value of the loss axis to 3. The change in losses is shown more clearly in this graph.

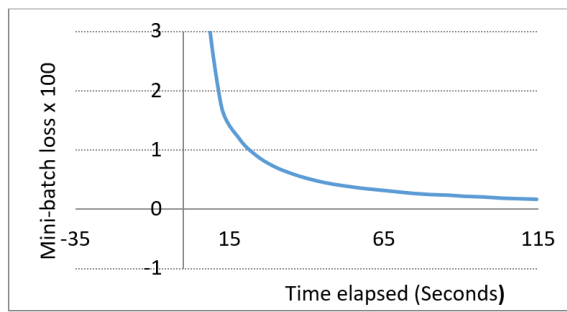


Fig. 6. Detailed loss curve

It is also possible to obtain an accuracy curve from the values in Table 2. Figure 7 shows the obtained accuracy curve. This accuracy curve is obtained by taking minimum values for every 50 epochs, as in the mini-batch loss curve. However, the total accuracy rate obtained is 99.11%.

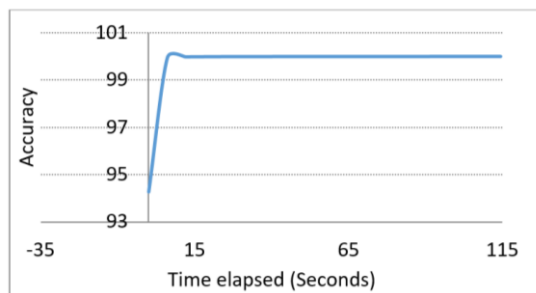


Fig. 7. Accuracy curve obtained from CNN model

V. CONCLUSION

In order to evaluate the results obtained from the CNN model designed in the study, it is seen that 1000 iterations in total are used in Table 2 when the training process is examined first. At the end of each 50 epoch, the error rate obtained by writing the lowest error rate shows an accuracy rate of 99.9983% after the last epoch. However, this accuracy is the lowest rate of the last 50 epochs. When all epochs are considered in this case, it is seen that the average accuracy rate is 99.11% of the true accuracy rate. This accuracy is an indication that the model is extremely successful. In the obtained error value, it is possible to say that the first epoch is a very high error of 5.71, but it is approaching zero by decreasing to the next epoch. Another important factor is the length of the education process. The training ended after 114.45 seconds at the end of a thousand epoch. This value may vary depending on the power of the processor, the size of the image, the number of images in the data set, and the number of convolutional and maxpooling layers used in the designed model. In fact, the number of filters used in the convolutional layer and the filter size affect both accuracy and training duration. As a result, with the designed CNN model, the estimation of which region of the lung of the squamous cell carcinoma tumor was performed in approximately 2 minutes, with an accuracy rate close to 100%.

REFERENCES

- [1] Spiro S.G, Porter J.C. Lung cancer-Where are we today? Current advances in staging and nonsurgical treatment. *American Journal of Respiratory and Critical Care Medicine*, vol.166, no.9, pp.1166-1196, 2002.
- [2] World Health Organisation, *The World Health Report*, 2004.
- [3] Derman B.A., Mileham K.F., Bonomi P.D., Batus M., Fidler M.J. Treatment of advanced squamous cell carcinoma of the lung: A review, *Transl Lung Cancer Res*, vol.4, no.5, pp. 524-532, 2015.

- [4] Wusheng Y., Ignacio I. Wistuba, Michael R. Emmert-Buck, Heidi S. Erickson, Squamous cell carcinoma – similarities and differences among anatomical sites, *Am J Cancer Res*, vol.1, no.3, pp.275-300, 2011.
- [5] Wilkerson M.D., et al., Lung Squamous Cell Carcinoma mRNA Expression Subtypes Are Reproducible, Clinically Important, and Correspond to Normal Cell Types, *Clinical Cancer Research*. vol.16, no.19, 2010.
- [6] Ateş İ., et al., Squamous Cell Cancer of The Lung with Synchronous Renal Cell Carcinoma, *Turkish Thoracic Journal*, vol.17, no.3, pp.125-127, 2016.
- [7] Reck M. and Rabe K.F. Precision Diagnosis and Treatment for Advanced Non–Small-Cell Lung Cancer, *The New England Journal of Medicine*, vol.377, pp.849-861, 2017.
- [8] Schild S.E., et al. Long-term results of a phase III trial comparing once-daily radiotherapy with twice-daily radiotherapy in limited-stage small-cell lung cancer, *International Journal of Radiation Oncology Biology-Physics*, vol.59, no.4, pp.943-951, 2004.
- [9] Kulkarni A., Panditrao A. Classification of Lung Cancer Stages on CT Scan Images Using Image Processing, 2014 IEEE International Conference on Advanced Communication Control and Computing Technologies (ICACCCT).
- [10] Sarker P., et al. Segmentation and Classification of Lung Tumor from 3D CT Image using K-means Clustering Algorithm, *Proceedings of the 4th International Conference on Advances in Electrical Engineering (ICAEE)* 8-30 September, Dhaka, Bangladesh, 2017.
- [11] Usui S., et al., Differences in the prognostic implications of vascular invasion between lung adenocarcinoma and squamous cell carcinoma, *An International Journal of Lung Cancer and Other Thoracic Malignancies*, vol.82, no.3, pp.407-412, 2013.
- [12] Vakili M., Yousefghahari B., Sharbatdaran M. Squamous cell carcinoma of lung with unusual site of metastasis, *Caspian Journal of Internal Medicine*, vol.3, no.2, pp.440-442, 2012.
- [13] Huang Z., Chen L., Wang C. Classifying Lung Adenocarcinoma and Squamous Cell Carcinoma using RNA-Seq Data, *Cancer Stud Mol Med Open Journal*, vol.3, no.2, pp.27-31, 2017.
- [14] Pearce C. *Convolutional Neural Networks and the Analysis of Cancer Imagery*, Stanford University, 2017.
- [15] Fabio A. et al., *Breast Cancer Histopathological Image Classification using Convolutional Neural Networks*, Saint Etienne du Rouvray, France, 2017.
- [16] Pratt H., Coenen F., Broadbent D.M., Harding S.P., Zheng Y. Convolutional Neural Networks for Diabetic Retinopathy, *International Conference On Medical Imaging Understanding and Analysis, MIUA 2016*, 6-8 July 2016, Loughborough, UK.
- [17] Vallières, M. et al. Radiomics strategies for risk assessment of tumour failure in head-and-neck cancer, *Scientific Report*, vol.7, 2017.
- [18] <http://www.cancerimagingarchive.net/>, date of access: 10 Jan 2018.

BIOGRAPHY



H. Selçuk NOĞAY received B.S degrees in Electrical Education from Kocaeli University, and M.S and Ph.D degrees in Electrical Education from Marmara University respectively 2002, 2003 and 2008. His research interests include artificial neural networks, deep learning and biomedical engineering. He has been working as a Professor in Vocational School of Kayseri University in Kayseri, Turkey.



T. Cetin Akıncı received B.S degrees in Electrical Engineering. M.Sc. and Ph.D. degrees from Marmara University, Istanbul-Turkey. His research interests include artificial neural networks, deep learning, machine learning, image processing, signal processing and, biomedical engineering. He has been working as an Associate Professor in Electrical Engineering Department of Istanbul Technical University (ITU) in Istanbul, Turkey.

Publication Ethics

The journal publishes original papers in the extensive field of Electrical-electronics and Computer engineering. To that end, it is essential that all who participate in producing the journal conduct themselves as authors, reviewers, editors, and publishers in accord with the highest level of professional ethics and standards. Plagiarism or self-plagiarism constitutes unethical scientific behavior and is never acceptable.

By submitting a manuscript to this journal, each author explicitly confirms that the manuscript meets the highest ethical standards for authors and coauthors

The undersigned hereby assign(s) to *Balkan Journal of Electrical & Computer Engineering* (BAJECE) copyright ownership in the above Paper, effective if and when the Paper is accepted for publication by BAJECE and to the extent transferable under applicable national law. This assignment gives BAJECE the right to register copyright to the Paper in its name as claimant and to publish the Paper in any print or electronic medium.

Authors, or their employers in the case of works made for hire, retain the following rights:

1. All proprietary rights other than copyright, including patent rights.
2. The right to make and distribute copies of the Paper for internal purposes.
3. The right to use the material for lecture or classroom purposes.
4. The right to prepare derivative publications based on the Paper, including books or book chapters, journal papers, and magazine articles, provided that publication of a derivative work occurs subsequent to the official date of publication by BAJECE.
5. The right to post an author-prepared version or an official version (preferred version) of the published paper on an internal or external server controlled exclusively by the author/employer, provided that (a) such posting is noncommercial in nature and the paper is made available to users without charge; (b) a copyright notice and full citation appear with the paper, and (c) a link to BAJECE's official online version of the abstract is provided using the DOI (Document Object Identifier) link.



ISSN: 2147- 284X
Year: July 2018
Volume: 6
Issue: 3

CONTENTS

T.P. Fowdur, R. Abdool Khader; An Anti-Web Phishing Application for Analysing the Security of Websites.....	146-152
L. T. Ergene, M. Imeryuz, C. Ekin; Cross Saturation Inductance Analysis of a Permanent Magnet Synchronous Motor,	153-158
K. Y. Aldoğan, C. Ide; Experimental Investigation of Refractive Index Measurement of Common Solvents and Aqueous Solutions in the Infrared Wavelengths,	159-164
R. Kopru, FSRFT Based Broadband Double Matching via Passband Extremums Determination,	165-171
A. Gencer; Modelling and control of permanent magnet synchronous generator based on three level NPC using fuzzy PI,	172-177
T. Ercan, M. Asim; Energy Efficient Routing Protocol to Extend WSN Lifetime,	178-182
A. Şenpınar; PV Array Based Smart Home Automation System,	183-190
A. Gezer; Identification of abnormal DNS traffic with Hurst parameter,	191-197
H. Gözde, B. Baydar, M.C. Taplamacioglu; Analysis of the Effect of Uncertain Renewable Sources on Static Voltage Stability by Using NR-Based DSOPF Model with Adapted IEEE-30 Bus Test System,	198-206
H. S. Noğay, T. C. Akinci; A Convolutional Neural Network Application for Predicting the Locating of Squamous Cell Carcinoma in the Lung,	207-210

BALKAN JOURNAL OF ELECTRICAL & COMPUTER ENGINEERING

(An International Peer Reviewed, Indexed and Open Access Journal)

Contact

Batman University
Department of Electrical-Electronics Engineering
Bati Raman Campus Batman-Turkey

Web: <https://www.bajece.com>
<http://dergipark.gov.tr/bajece>
e-mail: bajece@hotmail.com

